2006

Design and fabrication of micro transducers using cured SU-8 polymer as main structural material

Wen Dai
Louisiana State University and Agricultural and Mechanical College

DESIGN AND FABRICATION OF MICRO TRANSDUCERS USING CURED SU-8 POLYMER AS MAIN STRUCTURAL MATERIAL

A Dissertation

Submitted to the Graduate Faculty of the
Louisiana State University and
Agricultural and Mechanical College
in partial fulfillment of the
requirements for the degree of
Doctor of Philosophy

in

The Interdepartmental Program in Engineering Science

by
Wen Dai
B.S., Southeast University, 1998
M.S., Southeast University, 2002
December 2006

ACKNOWLEGEMENTS

In the course of the past four years, this research project has allowed me to cross paths with many remarkable people. I am obliged to express my appreciation for their encouragement, contributions, and guidance as their support and knowledge were indispensable for the completion of this dissertation.

First, I would like to thank Professor Wanjun Wang for his supervision and dedication. His invaluable insights and enthusiastic critique were instrumental throughout the duration of this project.

Second, I would also like to thank my committee members for their detailed review of this dissertation: Professor Wenjing Meng, Professor Ashok Srivastava, Professor Jin-Woo Choi, and the Dean's representative, Professor T. Gregory Guzik. Special thanks to Dr. Ren Yang and Mr. Dong Eun Lee for their friendship and encouragement in the past four years.

Third, this project could not exist without the generous financial support from the State of Louisiana Board of Regents and the Mechanical Department of Louisiana State University.

Finally, I would like to thank my parents, whose love and support are unparalleled.

TABLE OF CONTENTS

LIST OF TABLES

LIST OF FIGURES

ABSTRACT

Polymer based micro-transducers have many advantages over the traditional silicon based micro-transducers, such as easy integration with metal structures, design flexibility, and low fabrication costs. The characteristics of micro-transducers include converting electrical signals to/from mechanical response, the ability to sustain loading, sensitivity to external excitation, and etc. Some of the difficulties in realizing these characteristics include: characterizing material mechanical properties, techniques for producing electrically conductive polymer structures, and reliable fabrication procedures.

In this dissertation, research addressing these difficulties is presented. The developed techniques are demonstrated in the design and fabrication of a SU-8 polymer based comb-drive micro-actuator. The micro-actuator used SU-8 polymer as the main structural material and gold coating film for realizing electrical conduction. It was fabricated with multi-layer, multi-step UV-lithography technology and metallized with titled E-beam deposition and selectively electroless plating techniques.

The adhesion properties between metallic surface and SU-8 polymer were measured firstly. After comparing different metals, Au was chosen as the base material for electroplating for its good adhesion to SU-8. Customized micro-fracture toughness measurement procedure was then designed based on ASTM standards to measure the fracture toughness of Ni micro-structures.

The difficulties in micro-fabrication were then addressed. Two different approaches were evaluated for fabricating the SU-8 micro-structure: (1) multilayer processing using modified

SU-8 with reduced PAG; (2) multilayer processing using normal SU-8 with copper as sacrificial layer. The second method was shown more reliable. The polymer structures were surface metallized using two methods: (1) titled E-beam deposition; (2) selectively electroless plating. The latter was proven to be more suitable for high aspect ratio sidewalls. The proper UV exposure dosage, duration, and other parameters were also established.

A novel structural design of comb drive micro-actuator was studied using analytical and finite element analysis. The design was realized with the developed fabrication technologies. Finally, the resulted micro-actuators were tested to prove the feasibility of the design and fabrication.

CHAPTER 1. INTRODUCTION

1.1 MEMS Devices and Microfabrication Technologies

The application of integrated circuit fabrication technology to fabricating micro-scale mechanical, chemical, optical, and biological devices on primarily silicon wafers has introduced numerous innovative designs and unique opportunities in achieving difficult or infeasible functionalities for conventional devices, as well as reducing the cost in manufacturing them. Interest in MEMS has grown dramatically in the last decade because of the maturing of the fabrication technology and the gradually recognized wide range of industrial applications. Commercial MEMS products such as pressure sensors, acceleration sensors, gyros, ink-jet nozzles, read-write head positioners in hard drives, and digital light processors (DLPs) in projectors and television sets are just a few of numerous examples. Among the current commercial MEMS products on the market, about 40% is composed of sensors [1]. Their wide adaptation can be seen in the automotive industry, process control and automation, scientific and medical instrumentation, telecommunication, commodity products, environmental monitoring, and etc. Because of the fast pace in the maturity of the enabling technologies, and the ever increasing industrial needs, especially when the potentials of the MEMS devices start to gain wide acknowledgement, the MEMS technology has become one of the fastest evolving and growing fields both in academia and industry.

MEMSs are often labeled as “micro systems” in Europe and “micro machines” in Japan. From a practical point of view, MEMS devices are manufactured using similar

microfabrication techniques as those used to create integrated circuits. They often have moving components that allow a physical or analytical function to be performed by the device in addition to their electrical functions [2]. MEMS processing creates structures on wafers with depths one or two orders of magnitude larger than transistors.

The origin of MEMS technology dates back to semiconductor discoveries at Bell Laboratories in the early 1950s, and many consider the 1954 paper announcing the discovery of the piezoresistive effect in silicon and germanium as the birth of MEMS [1].

The MEMS fabrication technologies can be divided into several categories: surface micromachining, bulk micromachining, and LIGA (German acronym for X-ray lithography, electrodeposition, and molding.). Surface micromachining is a technology for fabricating three-dimensional micromechanical structures from multilayer stacked and patterned thin films. The process is additive in nature: various films are first deposited on top of the substrate, and then parts of deposited films are selectively removed to create MEMS devices, closely following the fabrication process of multi-layer integrated circuits. Although the surface micromachining is generally considered mature, its application is limited to certain thin film microstructures. Particularly, it is incapable of fabricating high aspect ratio microstructures. Bulk micromachining technology is based on single crystal silicon etching. The micro-structures are fabricated from silicon crystal or deposited/grown layers on silicon. High aspect ratio micro-structure can be realized with the bulk micromachining. It uses silicon wet etching, silicon dry etching, or LIGA processing to produce the bulk microstructures. The bulk

micromachined devices often have the combined mechanical and electrical merits of traditional devices [3].

One of the unique advantages of the LIGA micro-fabrication technology is its ability to fabricate high aspect-ratio microstructures from polymer, metals, and alloys. The possibility of utilizing other materials other than silicon opens up a new dimension in term of possible functionalities of the MEMS devices and reducing the manufacturing cost. With LIGA, any metals or alloys that can be electroplated can be used as potential materials for three-dimensional MEMS structural components. The combination of the broad material selection and the capability of fabricating high aspect ratio microstructures lend this technology numerous potentials [4].

LIGA technologies are mostly based on X-ray and UV-lithography. The advantages of the X-ray lithography based LIGA technology include high aspect ratios, excellent sidewall quality, and flexibility in selection of structural materials. The major disadvantage, on the other hand, is the requirement for synchrotron source, resulting in expensive fabrication investment. The UV-LIGA technology has been developed as a cheaper alternative, which is also capable of making metal and alloy microstructures with high aspect ratio as the x-ray based counterpart, although at the cost of slightly lower sidewall quality. In exchange, it eliminates the requirement for the expensive and complicated synchrotron source [3].

With the recent progress in UV lithography, the quality of the microstructures fabricated has also been improved dramatically. Various types of microdevices have been successfully

fabricated with metals, metal alloys, plastic alloys, or metal/polymer composites as structural materials [5-11].

1.2 Micro-transducer

Benefiting from the advances in general UV-LIGA fabrication technologies and new materials, the design and fabrication of the micro-transducers have attracted attentions, recognizing its potential industrial applications. The performance and manufacturing cost, as usual, are the two key components in determining how the new technology will be adapted in wide industrial applications, especially considering the typical industrial application scenarios of such devices. For instance, micro-transducers are often introduced as a cheap alternative to more expensive conventional transducers because they can be manufactured in large quantities. Therefore, the establishment of manufacturing processes that can result in both high-performance and low manufacturing cost is critical in realizing the great potential of MEMS micro-transducer.

Transducers operate by the simple principle of converting energy from one form to another, and/or from one system to another. Typical energy forms are mechanical, electrical, chemical, fluid, thermal, and etc. A transducer typically measures the physical quantity of interest indirectly through its effect on one of the transducer's parameters or vice versa.

In general, transducers can be divided into sensors and actuators. Sensors are devices that detect a change in an external physical stimulus such as acoustic, optical, and magnetic field, and convert it into a signal (usually electrical signal) that can be measured or recorded. Recent

micro-sensors are being used in many applications such as sophisticated guidance systems, antilock-braking systems, and micro-medical instruments. Reversely, actuators are devices that receive and respond to external signal, and transform the signal to physical change. Examples of actuators are relays, motors, pumps, tweezers, and force heads.

Although the transducers are commodities in modern industrial society, the emergence of micro-transducers is only since recent years. In spite of the short history, the unique advantages of micro-transducers have enabled them capture significant share of the market by replacing traditional transducers in many industries. Some of the advantages include smaller size, higher reliability, easier integration with other electrical components, lower noise, longer lifetime, faster response, low-cost batch manufacturing, less drive power, and easier integration of multiple relays on the same substrate or inside the same package. In this research work, we will be focusing on one of the categories of the micro-transducers, the micro-actuator only.

Successful micro-actuators must meet the following requirements: (a) capable of producing large angular or linear displacements; (b) utilizing effectively three-dimensional geometries to increase the power capability; (c) effectively interfacing with and transferring power to the external environment [12].

Different micro-actuators are based on different actuation principles allowing the realization of different behaviors. Based on their physical mechanisms, the micro-actuators can be divided into four categories: piezoactuators, thermal actuators, electromagnetic actuators, and electrostatic actuators. Compared with other options, electrostatic excitation combined with

capacitive detection is an attractive approach due to the simplicity and compatibility with microstructures based on silicon or other new materials [13].

Electrostatic actuators consisting of moving conductors and dielectrics have long been used in macroscopic systems such as electrostatic voltage meters. The corresponding micro-scale counterparts are also emerging with the MEMS technology, which essentially allow the movement of micro-scale structures. One typical example of micro-actuator structure is the comb-drive actuator [14]. Typical comb-drive actuators consist of two sets of interdigitated finger structures with one fixed and the other connected to a compliant suspension. Each pair of the fingers forms a parallel capacitor. In comb-drive actuators, the application of a driving voltage between the comb structures results in a displacement of the movable fingers towards the fixed fingers driven by the attractive electrostatic force. The kinetics of the movable finger structure is determined by the balance between the electrostatic force and the mechanical reaction force of the compliant suspension. The comb-drive actuators can be found in resonators, microgrippers, optical shutters, electromechanical filters, force-balanced accelerometers, *x*–*y* microstages, and driving elements for micromechanical gears [15].

Many research efforts on comb drive have been reported since first reported by Tang et al. [16]. Johnson and Warn reported a physical analysis [17]. Ye and Jensen proposed optimal shaped comb designs such as quadratic or cubic force profiles under constant bias voltage to produce highly linear force-displacement behavior [18]. Zhou et al. [15] presented tilted folded-beam suspension to extend the stable travel range of comb drive micro-actuators using

low voltages. Other investigations on the comb drive have also been published, including a triangular comb drive array to realize micromechanical resonant frequency tuning, an asymmetric comb drive in out-of-plane and torsional motion, a new comb drive actuator realizing three dimensional continuous motion, and angular vertical comb drive structures with high tuning capabilities [19-25].

The previously reported comb-drive actuators are mostly made from crystalline silicon and polycrystalline silicon. But the cost fabrication based on silicon chips remains high due to the complex fabrication processes in the clean room. Recently, new materials, especially polymer materials have been of great interest in the research and development of integrated circuits (IC) and MEMS due to their relatively low cost and easiness in processing. W. Eberhardt [26] proposed to fabricate polymer micromechanical devices coated with metal layers such as copper and gold using electroless plating technology. Zhao and Cui [25] also reported effort to use hot embossing technique in the fabrication of polymer-based electrostatic comb drives using PMMA as the structural material.

In recent years, a relatively new type of resist, SU-8, received wide attention in the microfabrication community. SU-8 is a negative, epoxy-type, near-UV photoresist based on EPON SU-8 epoxy resin originally developed and patented by IBM [27-30]. Significant research efforts have been made worldwide on the UV lithography of SU-8 and on the microfabrication technology based on it. The resist can be spin-coated as thick as 2 mm and offer aspect ratio as high as 40 [31]. Up to now, SU-8 has been mostly used in two ways. On

one hand, it is used as a thick resist material for UV lithography to fabricate plating moulds for UV-LIGA microfabrication. On the other hand, cured SU-8 polymer has also been used as structural materials for microsystems, especially in microfluidic systems [5,7,10,32,33,34] due to its excellent chemical and thermal stability. UV-LIGA technology based on cured SU-8 has some unique advantages: (1) it allows the fabrication of microstructures of any lateral shape with structural heights up to several hundreds of micrometers in any cross-sectional shape; (2) a wide variety of materials such as plastics, metals, alloys, and ceramics, or combinations of these materials can be used as the structural materials. These advantages make it very suitable for fabricating micro-actuators.

To the author's best knowledge, SU-8 based micro-transducers have not been reported in the open literature up to the now. The design and fabrication techniques for the SU-8 based micro-transducers, therefore, present a particularly important and challenging research topic that could lead to the adaptation of a new category of materials in manufacturing the micro-transducers. In particular, because the SU-8 is not electrically conductive, the metallic coating on US-8 polymer becomes one of the greatest difficulties and at the same time, the key enabling technology, which are addressed and successfully achieved in this research work.

1.3 Scope of the Research

In this dissertation, an innovative low cost concept for the design and fabrication of comb drive micro-actuators is presented. The fabrication techniques were based on high aspect ratio SU-8 polymer micro-structures fabricated with multi-layer, multi-step UV-lithography

technology, and metallization of the micro-structure with tilted E-beam evaporation or electroless plating method.

The first effort was spent on the investigation of adhesion property of cured SU-8 and metallic surfaces because a good adhesion between cured SU-8 and various substrate materials is essential to both the fabrication process and to the functionality of any final products that have cured SU-8 as part of the structural material. For the commonly used silicon wafer, adhesion is reasonably good. However, debonding on many metallic surfaces was often observed and caused failure of final devices. Chapter 2 will present a theoretical and experimental work to quantitatively study the adhesion properties of cured SU-8 on some of the most commonly used metallic material surfaces.

To achieve broad applications of UV-LIGA technology, numerous difficulties in fabrication process need to be resolved. One of the difficulties is the lack of micro-scale property characterization for the electroplated metals or alloys from which microstructures and microdevices are fabricated. The property database is particularly important for LIGA technology because these mechanical properties cannot be extrapolated from macro-scale data without experimental verification. In this work, we investigate the polymer and metal mixed micro-transducer, hence, the knowledge of such material properties is of vital importance. Chapter 3 will report an experiment scheme and UV-LIGA microfabrication procedure for specimen fabrication to study the fracture toughness of nickel. The resulted methodology lays groundwork for the fracture toughness measurement of other materials.

Chapter 4, Chapter 5, Chapter 6, and Chapter 7 will focus on the design of comb-drive micro-actuator, fabrication techniques, possible problems and their resolving approaches, testing methods, and testing results. In Chapter 4, the kinetic mechanisms of comb-drive micro-actuators based on the electrostatic force are first explained. Several common spring structure design methods are then discussed. Quantitative analytical and numerical analysis results for predicting comb-drive performance are provided. Chapter 5 describes two types of related multi-layer and multi-step UV-LIGA fabrication processes for fabricating the micro-actuators. Chapter 6 details two techniques for metallizing SU-8 polymer. In the first technique, selective e-beam evaporation with tilted angle is proposed to obtain electrically conductive side wall of comb drive fingers. The other technique of selectively electroless plating is then introduced and compared with the prior technique, and is demonstrated capable of overcoming the difficulties in handling entailed by the selective e-beam evaporation technique. More importantly, no special over-hang geometry for comb drive microstructure design is necessary for in this case, since the metal film can be coated on both the top and side wall surfaces of SU-8 microstructures while avoid coating the silicon wafer. The fabrication procedures are summarized in Chapter 7, followed by the unsuccessful experimental results, which reveals the necessary improvements. With the enhanced fabrication procedures and parameters, the successfully produced comb-drive micro-actuators are shown in microscopic and SEM pictures. The initial test results confirming the successful achievement of free-moving spring system and comb fingers, as well as the metallic coating of entire designed

surfaces including the deep side walls, are presented. Qualitative micro-actuator responses driven by external voltage are finally illustrated. The thesis concludes with related discussion and suggestions for future improvements.

CHAPTER 2. STUDY ON ADHESION PROPERTIES OF CURED SU-8 ON METALLIC SURFACES

2.1 Review for Adhesion Problem between SU-8 and Metallic Surfaces

One of the reasons that SU-8 has attracted attentions in recent years is its applications in the fabrication of high aspect ratio microstructures and microdevices. With the latest progress in UV-lithography of SU-8, the quality of the microstructures produced has also been improved dramatically. A variety of microdevices made of pure metal, alloys, or metal/polymer composites as structural materials have been reported using the SU-8 UV lithography technique [6-11] A good understanding and characterization of the behavior of cured SU-8 polymer on various substrate materials are hence important. For example, in situations where cured SU-8 polymer itself is used as structural material in microdevices, the adhesion strength between the cured SU-8 polymer and the substrates is of significant importance for the devices' quality and functionality. In this research, as will be illustrated in later chapters, the fabrication of micro-transducer utilized thin gold layer as the seed layer for electroplating, and the SU-8 polymer suspended microstructures were grown on copper layer which was used as the sacrificial layer. Cured SU-8 is well known for being extremely difficult to strip. A common problem in using SU-8 as resist for microfabrication is the residual SU-8 polymer in the narrow grooves and small features. On the other hand, poor adhesion of SU-8 on some of the commonly used substrate materials also often limits the choices of the microstructures desired for particular applications. For the commonly used silicon wafer, adhesion is reasonably good.

However, thin films of different metals often need to be evaporated or sputtered on the silicon or glass substrate as seed layers for electroplating metals and alloys, or as electrodes for power supplies. In such cases, debonding problems are frequent encountered, which eventually limits the application of SU-8 based UV-LIGA technique. For example, in UV-LIGA process, chromium is commonly used as adhesive layer for electroplating other metals on silicon substrate. However, many researchers have found poor adhesion between SU-8 and Cr coated surface [35,36]. In our case where cured SU-8 polymer is used as structural material in micro-transducer, the knowledgebase of the adhesion properties between SU-8 and different metallic film wafers is thus particularly essential in achieving the desired device performance, quality, and reliability.

Although it has been found that SU-8 has poor adhesion on most metal surfaces [35,37], few efforts have been made to quantitatively assess this issue. Jun et al. and Jingqun et al. reported some research work in this area [35,36]. They suggested from their experiment results that Ti film or Ti film with oxidation treatment has the strongest adhesion to cured SU-8 compared to other metals like Cu, Ni, Fe, Au, and Cr. However, no detailed information about the adhesion strength was provided in their paper. Another work on the adhesion strength of SU-8 was reported by Khoo et al. [38]. They studied the shear failure stress of SU-8 on silicon substrate by applying pulling load on circular and square samples fabricated on silicon substrate. To the best of our knowledge, there has been no study reported on the pulling adhesion strengths between SU-8 and commonly used metallic surfaces in open literature.

This chapter presents a theoretical and experimental work to quantitatively study the adhesion properties of cured SU-8 on some of the most commonly used metallic materials surfaces. The adhesion strengths of cured SU-8 samples on Au, Ti, Cu, Cr, and Ni coated glass substrates were measured following ASTM-C633 standard. A detailed analysis of the experimental results was also provided based on the atomic structures and electronic configurations of the respective metals.

In the following sections, the lithography conditions for substrates with different surface metals such as Cu, Ti, Au, Ni and Cr are presented in details. All the samples used in the experiments were designed to have the circular geometry. Efforts have been made to maintain the same processing conditions for all of the samples if possible for comparison purposes.

2.2 Sample Preparation

Careful and appropriate sample fabrication and preparation procedures are critical to the success of the experiments. To quantitatively characterize the adhesion strength of cured SU-8 polymer on various substrate materials, the 100 μm thick SU-8 circular patterns with 5, 10, and 25 mm diameters were designed and fabricated. Well documented processing parameters and procedures were used and followed consistently so that meaningful comparisons can be drawn from the experimental data.

2.2.1 Substrate Preparation

In the experiments, the Soda Lime glass plates (Capitol City Glass, Baton Rouge, LA) were chosen as the substrates, on which five different metallic films were deposited. A 2% microsoap

solution was applied to clean the glass substrate at 66 ^{0}C with ultrasonic agitation for 30 minutes. The glass plates were then rinsed using acetone, Isopropanol (IPA), and deionized (DI) water respectively. A pre-bake process was carried out on a hotplate for 30 minutes to dehydrate the substrates.

After dehydration, the glass wafers were put in the plasma asher machine for several minutes. A 10 nm Cr was then deposited on the glasses as the adhesive layer. This thin layer of the seed layer was necessary to boost the adhesion of the other metal films to be deposited on the substrates, which is a common practice in microfabrication. Finally, 50 nm Au, Cu, Ti, Ni, and Cr films were deposited on the Cr covered wafers, respectively.

2.2.2 Resist Coating

An SU-8 resist (SU-8 25 from MicroChem Corporation, MA) of 100 μm thickness was spun on the substrates coated with different metallic films. The freshly prepared substrates provided better adhesion compared with the adhesion on the prepared substrates that were shelved for a few days before spin-coating. Part of the reason for this phenomenon may be that oxidation of the metal films or moisture on the surfaces of these films might have negatively affected the adhesion property, which has been a common observation. To reduce the adverse effect of air oxidation and moisture, efforts were made to reduce exposure time of the fresh substrates to air by coating photoresist right after the metal films were deposited on the substrates. To obtain a 100 μm thick SU-8 film, about 3 ml SU-8 25 was dispensed on four inches diameter substrates and then spun at the speed of 700 rpm for 30 seconds. All specimens

in this chapter were made under this condition, so that meaningful comparison could be conducted later between materials.

2.2.3 Soft-bake

After the SU-8 was coated, the samples were placed on a level surface for overnight. This was proven a key factor in successful sample preparation. It improved the adhesion between SU-8 and metals, such as Au and Ti, as well as the resist layer uniformity, which was particularly important.

Insufficient soft-bake may cause SU-8 sticking to the mask, in addition to low quality patterned microstructures. On the other hand, over-bake reduces the adhesion strength between the resist and metals [36].

To soft-bake the 100 μm SU-8 on the hotplate, the temperature was ramped up to 65 ^{0}C in 15 minutes and stayed for 10 minutes at 65 ^{0}C. The temperature was further ramped to 100 ^{0}C in 15 minutes and stayed at that temperature for another 90 minutes. The samples were then cooled down to 55 ^{0}C in 1 hour and kept at 55 ^{0}C for 2 hours. For anneal purpose the temperature was ramped back to room temperature step by step to avoid the generation of internal stresses.

2.2.4 Exposure

Exposure dosage is critical to the quality of adhesion between SU-8 resist and substrates. When the same exposure dosage was tried on different substrates, adhesion problems surfaced between SU-8 and some of the tested metal films. Different metallic surfaces may have

different reflection coefficients that may cause significant changes in effective dosages at the top and the bottom of resist, which could lead to poor lithography quality [36]. To alleviate the adversary influence, the exposure dosage should be adjusted according to different substrates. Through experiments, optimal dosages for samples with a resist layer of 100 μm were recorded as listed in Table 2-1.

Table 2-1 Dosages for different metallic surfaces

Material	Ti	Au	Cu	Ni	Cr
Dosage (mJ/cm^2)	550	350	400	520	500

2.2.5 Post-bake

Post-bake process could severely affect residual stresses in the final microstructures of cured SU-8 polymer as suggested by Williams and Wang [39]. Careful control for the post-bake temperature should be exercised to decrease the internal stress, which is more serious for thick SU-8 layers. In the experiments with 100 μm SU-8, the samples were post-baked for 15 minutes at 96 ^{0}C, then cooled down to 55 ^{0}C for one hour. The samples were then kept at 55 ^{0}C for 2 hours, and finally ramped down to room temperature in 2 hours.

2.2.6 Development

SU-8 developer from MicroChem Corporation was used in this experiment. During the fabrication, it was often observed that over development erodes the bottom of the resist and damages the adhesion strength between the pattern and substrates. This is especially true at the edges of the samples where most debonding was observed. In our experiments, a development time of 20 minutes was adapted for 100 μm SU-8 resist. After patterns were developed, IPA

was used to rinse the structure to remove residual developer. The samples were finally blown dry before adhesion tests.

2.3 Experimental Principle and Adhesion Tests

2.3.1 Adhesion Test Principle and Measurement Standard

Materials with high Young's modulus, large hardness value, or less ductility exhibit low real area of contact, which leads to low adhesion [40]. The separation force (pulling force) between two solid surfaces is often referred to the adhesion force. Thus, the adhesion strength σ is defined as the separation force per unit area:

$$\sigma = \frac{F_{sep}}{A} \tag{2.1}$$

where F_{sep} is the separation load between two surfaces and A is the real area of contact. The separation load on the interface can be measured and then divided by the real contact area to compare adhesion strengths between the cured SU-8 and different metallic substrate surfaces.

Adhesion test of a coating layer is a destructive test, and sample cannot be reused. The experiment was designed to have multiple samples fabricated on a single wafer to avoid any inconsistence in sample preparation.

The adhesion test was designed for pulling off cured SU-8 structures in accordance with ASTM-C633 standard [41]. Pull-off adhesion testing is a measurement of the separation resistance of a coating from the substrate when a perpendicular tensile force is applied. The ASTM adhesion test standard requires the use of a stationary tensile testing disk. Two cylinders, one of which is coated with tested material, are glued together and then pulled apart. Load cell

is used to measure the force required to separate the coating from the substrate. The schematic diagram of the test set-up is shown in the Figure 2-1.

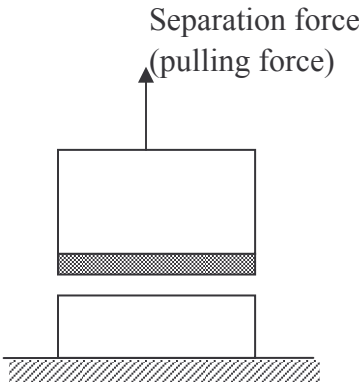

Figure 2-1 The ASTM-C633 adhesion test principle

The aluminum cylinder was glued to the cured SU-8 disk on the wafer before the pulling test. The glue must be able to provide an adhesion stronger than that between the SU-8 sample and the substrates to be tested. Several types of epoxy glues were tested. The best adhesion was found with No. 20-8130-128 Epoxide resin and No. 20-8132-032 Epoxide hardener supplied by Buehler Ltd, [Lake Bluff, IL]. Five parts by weight of No. 20-8130 Epoxide resin was mixed with one part by weight of No. 20-8132 Epoxide Hardener, which was then blended thoroughly to ensure no air bubble entrapment. To minimize shrinkage, the mixed resins were heated to 65 ^{0}C for 2 hours, followed by another 4 hours curing at room temperature. After that, the mixed glue was applied on the aluminum cylinder, which was then bonded with SU-8 film. After the aluminum cylinder was glued on the SU-8 sample, the entire wafer with multiple samples on it was held down using the vacuum chuck. A controlled load was applied to the aluminum alloy

cylinder, which delivered the force to the SU-8 disk. The pulling force applied was measured by the load cell and displayed by the palm load cell indicator.

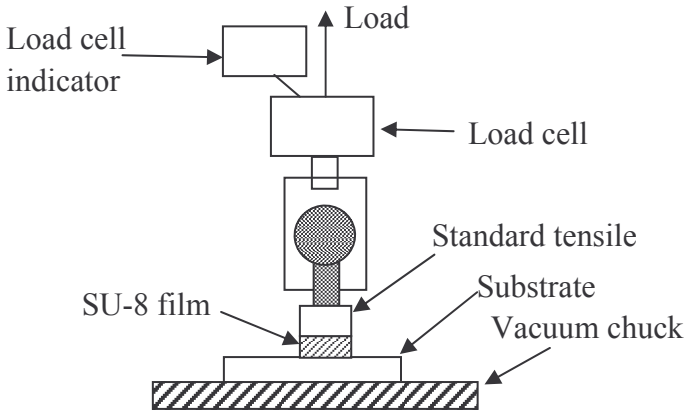

Figure 2-2 Schematic view of the measurement system

2.3.2 Adhesion Tests for Substrates Coated With Au and Ti Films

On Au and Ti coated substrates, SU-8 samples with diameters in the range from 5 to 25 mm were successfully fabricated. Samples on Ti surface with a thickness of 500 μm still showed excellent adhesion after the development. Figure 2-3(a) and (b) show the successful adhesive examples. Severe adhesion problems were encountered for other samples with most of SU-8 samples with diameters larger than 10 mm falling off the substrates after the development process.

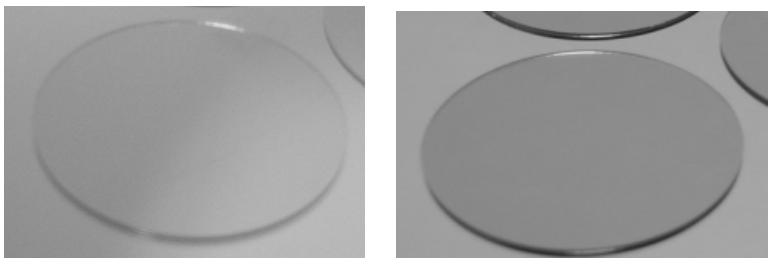

Figure 2-3 Adhesive test samples (a) The 100 μm thick SU-8 on Au film of 25 mm in diameter; (b) the 500 μm thick SU-8 on Ti film of 25 mm in diameter

Table 2-2 and table 2-3 show the adhesion strengths of SU-8 film on Au and Ti coated substrates. The test results showed certain scattering of the measured strength. ASTM-C633 requires a minimum of five specimens. It also does not require statistical analysis because the small number of specimens. The standard engineering practice in this kind of tests are to calculate the average adhesion strengths and provide the range of the experimental data as shown in ASTM-C633 [41]. However, to obtain a better quantitative understanding of the experimental data, a simple statistical analysis was conducted to obtain the uncertainty of the experimental data. It was found that the average adhesion strength for samples coated with Au is 7.099×10^4 Pa, with standard deviation of 0.354 $\times10^4$ Pa. The average adhesion strength for Ti coated samples is 7.783×10^4 Pa, with standard deviation of 1.169×10^4 Pa. It should be noticed that the standard deviation represents a significant part of the average strength values, particularly for Ti coated samples.

Table 2-2 Test results for Au film

Au film on SU-8 film	Test1	Test2	Test3	Test4	Test5
Interfacial separation force (N)	31.736	36.625	34.320	35.348	36.104
Portion of surface pulled off	97%	85%	90%	92%	95%
Diameter ($\times10^{-3}$m)	25	25	25	25	25
Adhesion strength ($\times10^4$Pa)	6.467	7.467	6.994	7.206	7.361

Table 2-3 Test results for Ti film

Ti film on SU-8 film	Test1	Test2	Test3	Test4	Test5
Interfacial separation force(N)	38.022	35.762	30.255	47.949	38.951
Diameter($\times10^{-3}$m)	25	25	25	25	25
adhesion strength ($\times10^4$Pa)	7.751	7.289	6.167	9.771	7.939

2.3.3 Adhesion Tests for Substrates Coated With Cu, Ni, and Cr Films

As mentioned previously, most of the samples with a diameter of 25 mm tended to fall off the substrates after development except for the substrates coated with films of Ti and Au. There may be two reasons behind this phenomenon. One is the inherently weak adhesion between SU-8 film and these metallic surfaces, and the other is the internal stress generated during the baking process.

When sample size was reduced to 10 mm, most of the samples on Cu, Ni, and Cr surfaces had no obvious debonding. When the sample size was further reduced to 5 mm, all of the samples were perfectly bonded to the substrates. Because the samples with 5 mm in diameter were extremely difficult to be handled by the standard test equipment, samples with diameter of 10 mm were used for testing the adhesion on the substrates coated with Ni, Cu, and Cr.

Figure 2-4 shows the photographs of a sample on Cu coated substrate. Significant debonding can be observed along the edge from Figure 2-4 (a). After the sample sizes were reduced to 5 mm in diameter, debonding could not be observed on the samples on Cu coated substrates, as shown in Figure 2-4 (b), and same for Cr and Ni coated substrates (not shown).

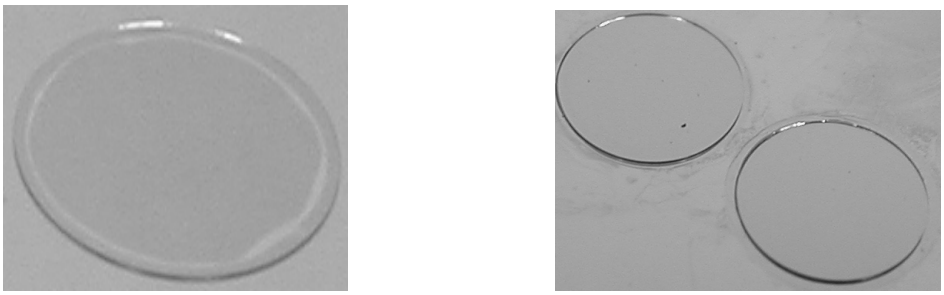

(a) (b)

Figure 2-4 Adhesion test samples made on Cu coated substrate (a) 13 mm (b) 5 mm in diameter

The experimental results for Cu, Ni, and Cr coated substrates are listed in Table 2-4, Table 2-5, and Table 2-6, respectively. All of these results were obtained using the samples with diameter of 10 mm and thickness of 100 μm.

Table 2-4 Test results for Cu coated substrates, average adhesion strength 4.697×10^4 Pa

Cu film on SU-8 film	Test1	Test2	Test3	Test4	Test5
Interfacial separation force (N)	3.874	3.879	3.612	5.942	5.943
Pattern Diameter ($\times10^{-3}$m)	10	10	10	10	10
Adhesion strength ($\times10^4$Pa)	4.936	4.941	4.601	4.438	4.568

Table 2-5 Test results for Ni coated substrates, average adhesion strength 4.486×10^4 Pa

Ni film on SU-8 film	Test1	Test2	Test3	Test4	Test5
Interfacial separation force (N)	3.848	3.403	3.474	4.159	2.722
Diameter ($\times10^{-3}$m)	10	10	10	10	10
Adhesion strength ($\times10^4$Pa)	4.902	4.337	4.426	5.298	3.469

Similar to previous cases, the measurement also showed significant scattering that prevented a precise and conclusive results of the adhesion strength. The average of adhesion strengths are: 4.697×10^4 Pa with standard deviation of 0.205×10^4 Pa, between Cu coated film and SU-8 film; 4.486×10^4 Pa with standard deviation of 0.615×10^4 Pa between Ni coated film and SU-8 film; and 7.681×10^4 Pa with standard deviation of 0.513×10^4 Pa between Cr coated film and SU-8 film.

Table 2-6 Test results for Cr coated substrates, average adhesion strength 7.681×10^4 Pa

Cr film on SU-8 film	Test1	Test2	Test3	Test4	Test5
Interfacial separation force (N)	6.579	5.422	6.886	6.067	5.462
Diameter ($\times10^{-3}$m)	10	10	10	10	10
Adhesion strength ($\times10^4$Pa)	8.038	6.903	8.772	7.726	6.967

2.4 Discussions of the Adhesion between SU-8 and Metallic Surfaces

The adhesion strength tests were first attempted with larger specimen size of 25 mm in diameter, according to the requirement of ASTM Standard C633. The purpose of the requirement is to reduce the operational influence from the specimen size variation, as it affects the accuracy in the measurement of the true contact area. During the tests, however, it was found that the large internal stress in the samples of Cu, Ni, and Cr coated samples made it very difficult to fabricate these samples successfully. Only these samples coated with Au and Ti films withstood the fabrication process and stayed on the substrate. Therefore, smaller specimen sizes had to be used for these three films, at the cost of increased inaccuracy. After testing different sizes, it was found that a diameter of 10 mm would allow reduced level of internal stress and reliable adhesion of the Cu, Ni, and Cr films on the substrate, and rendered the test meaningful. Five measurements were conducted for each type of metals as required by ASTM C633 [41]. The relatively large standard deviation show previously suggests that the measurements were affected significantly by the inaccuracy in the specimen sizes and fabrication (such as residual stress). Nevertheless, the results showed dramatic difference between two groups of metal surfaces with Au, Cr, and Ti as one, with Cu and Ni as another one. While within each group the difference is not as significant because of the large deviation of the experimental data.

As shown previously, and summarized in Table 2-7, two groups of adhesion strength clearly exist. The first group includes Cu and Ni with strength in the range of 4×10^4 Pa to 5 x

10^4 Pa. The second group includes Ti, Cr, and Au, and has strength value in the range of 7 x 10^4 Pa to 8 x 10^4 Pa. The second group of adhesion strength is much larger than the first group. Within each group though, however, the scattering of measurement data prevented conclusive ranking of the materials.

Many factors affect the adhesion strength between two materials, some of which counteract with each other or even can cancel each other, rendering the interpretation the data and explanation of the adhesion strength ranking from the underlying physical and chemical mechanisms difficult. Still, we attempt to provide some insights into the fundamental of material adhesion to explain the observed difference between the materials, with the hope of establishing a general guideline in evaluating materials that are not covered in this research, when coated with SU-8 polymer.

2.4.1 Ionic or Electrostatic Bonds of the Metallic Films and Free Surface Energy Effect

Adhesion is an interfacial phenomenon. The adhesion strength of an interface is a measurement of the attraction between the two surfaces. The physical principles for the surface attraction are discussed in this section.

Ionic bonds are formed when one or more electrons are transferred from one atom to another. Metals, which have relatively little attraction for their valence electrons, tend to form ionic bonds when combined with nonmetals. When a polymer and a metal are brought into contact, separation of charge at the interface is very large. An electrostatic attraction is generated in addition to the van der Waals interaction between the two bodies and it is

particularly the case when the entirety of the adhesion is electrostatic in origin [42]. The electrostatic interactions are dependent on the atomic structures of the particular metals as well as the polymers, in our case the atomic structures of Au, Cu, Cr, Ni, Ti, and cured SU-8. Table 2-7 lists the basic atomic structures, the surface energies, atomic volumes, and other related information for these five different metals according to their relative positions in the periodic table of the elements [43-45].

The adhesion between metals and cured SU-8 polymer is mainly affected by electrostatic interaction. The electrostatic interaction between a metallic surface and SU-8 varies from metal to metal. These differences in electrostatic interaction may explain why some metals have good adhesion with cured SU-8 while others do not. Careful investigation and comparison of the atomic structures of these metals and the respective surface energies could help to explain the results obtained in the experiments and provide some general guidelines for the expected adhesion strength between a particular metallic surface and cured SU-8.

As a polymer, cured SU-8 contains eight functional groups with rich oxygen that has larger electronegativity (3.44 pauling scale) than metals. Electronegativity is defined as the power of an atom in a molecule to attract electrons to it [44]. Atoms with high electronegativity tend to draw the electrons closer, and therefore have a more negative electrical charge [44]. On the other hand, atoms with less electronegativity are easy to lose electrons, and therefore appear partially positive. When two atoms with different electronegativities are in vicinity, it is relatively easier for the atom with lower electronegativity to lose its electrons and to be

partially positive. In general, the electronegativity depends on atomic structures such as the ground state electron configuration, atomic number, and atomic volume.

From Table 2-7, it can be seen that Ti has small electronegativity and few outer layer electrons, which means it may lose the electrons to oxygen in SU-8 easily. Based on this argument, the adhesion between Ti and SU-8 therefore can be expected to be the strong among these five metallic surfaces. Also, Cr should have better adhesion property than Ni and Cu.

For the exception to previous trend, the Au, we postulate that the abnormality was at least partially caused by the atomic volume. Though gold is a very stable metal, the large atomic volume may have rendered it more easily attracted by oxygen because atoms with large atomic volume tend to have less control over its electrons. This effect might have contributed to the enhanced adhesion between SU-8 and Au. The same argument may also be used to analyze other metallic surfaces. For example, Ni has the smallest atomic volume. Its electrons therefore surround the nucleus tightly, and have less chance to be attracted by oxygen, consequently adversely influencing the adhesion between Ni and SU-8.

Table 2-8 ranks the five types of metals according to their atomic volumes. From Table 2-8, it can be seen that as the atomic volumes become smaller, the adhesion in general becomes weaker, particularly when we compare the two groups of materials.

Besides the atomic volume, the surface energy is another factor that warrants the concern. The surface energy is defined as the excess energy associated with the presence of a surface [40], and is often considered fundamental to the understanding of adhesion. Surface energies

are associated with the formation or the failure of the adhesive bond. In general, the higher the surface energy of a solid surface is, the stronger are the bonds it will form with a mating material. The surface energies of metals are often much higher than that of polymers. According to Table 2-7, Ti has the high surface energy, and hence has strong adhesion to SU-8. Similarly, the higher adhesion strength between Cr and SU-8 than that between Cu and SU-8 can be explained.

Table 2-7 Rank of the metallic surfaces based on their relative positions in the periodic table of elements

Metals	Ti	Cr	Ni	Cu	Au
Atomic numbers	22	24	28	29	79
ground state electron configuration	$[Ar]3d^2 4s^2$	$[Ar]3d^5 4s^1$	$[Ar]3d^8 4s^2$	$[Ar]3d^{10} 4s^1$	$[Xe]4f^{14} 5d^{10} 6s^1$
Electronegativity (Pauling scale)	1.54	1.66	1.91	1.90	2.54
Atomic volume (cm^3/mol)	10.60	7.29	6.64	7.11	10.22
Surface energy (Jm^{-2})	2.6	2.1	2.5	1.9	1.6
Adhesion strength ($\times 10^4$ Pa)	7.783 ±1.169	7.681 ±0.513	4.486 ±0.615	4.697 ±0.205	7.099 ±0.354

Table 2-8 Rank of the metallic surfaces based on their atomic volumes

Metals	Ti	Au	Cr	Cu	Ni
Atomic volume (cm^3/mol)	10.60	10.22	7.29	7.11	6.64
Adhesion strength ($\times 10^4$Pa)	7.783 ±1.169	7.099 ±0.354	7.681 ±0.513	4.697 ±0.205	4.486 ±0.615

2.4.2 Other Factors That May Also Effect the Adhesion Strengths

Most of the SU8 patterns made on the Ni, Cu, and Cr coated substrates fell off after the development process for the pattern sizes larger than 25 mm in diameter. Only the samples fabricated on Ti and Au coated substrates showed no debonding at the sizes of 25 mm in diameter. As the sizes of the samples were reduced, the debonding problems become less serious. For the samples with diameter of 10 mm, samples on all of the five different types of metallic surfaces showed very little debonding. When the size was reduced to 5 mm in diameter, all of the samples showed no debonding problems.

This size dependence of the adhesion property may be explained by the thermal expansion coefficients of these metals tested. Table 2-9 lists the thermal expansion coefficients of the five different metals used in the experiments at temperature of 100 ^{0}C [43] and cured SU-8 polymer [37]. From the table, it can be seen that the mismatch of thermal expansion coefficients between Cr and SU-8 is the highest among the coefficients between metals and SU-8, which causes a larger residual stress at the interface between SU-8 film and Cr during the lithography process in comparison to stresses between SU-8 and other metals [37]. Cr is therefore most affected by the residual stress in large SU-8 structures. The experiments also demonstrated that the adhesion between Cr and SU-8 became much better when the size of SU-8 film was reduced.

Table 2-9 The thermal expansion coefficients of the metals tested

Metals/SU-8	Ti	Ni	Cr	Cu	Au	SU-8
Coefficient of thermal expansion (10^{-6} /K)	8.8	13.3	6.6	17.1	14.2	52+/-5.1

Another reason for the low adhesion strength of Ni coated surface may be that Ni may dissolve in weak acid and form “hydrated ions” [45]. The PH value of SU-8 developer is measured between 5 and 6, which indicates the SU-8 developer can ionize H^+ and is of weak acid properties. During the development, SU-8 developer solution may attack nickel surface around the edges of the SU-8 film. This may be part of the reason that debonding phenomena was observed, which reduced the adhesion strength greatly.

In general, surface humidity also affects the adhesion strength significantly. When exposed to the ambient air, even the noble metals absorb water vapor. A short period of exposure in air may lead to vapor on the surface and reduced adhesion.

Small amount of contaminants may significantly affect the adhesion of metals and SU-8 film. Especially, a very small amount of oxygen can produce a marked reduction in the adhesion strength [40]. Different metals are affected to different extent. For example, Cu is easily oxidized in the air, resulting in a loss of oxides on the surface, which might be the main reason why the adhesion between Cu and SU-8 tended to be lower.

In this section, we attempted to explain the material adhesion strength results from physical mechanisms. However, we also recognize that the data scattering was very large; therefore, the conclusion might not be conclusive by only analyzing the limited samples. For instance, the overlapping of the uncertainty range between Ti and Au was significant. This suggests that quantitative comparison and absolute ranking of material within each strength group are not very meaningful. Further investigation is necessary to produce statistically meaningful data set

to allow quantitative comparison within each strength group. Nevertheless, the difference between the two material groups has been clearly established and explained, consequently, the trend revealed suffices the purpose of this research by providing the guideline for selecting the candidate materials for the seed layer in later chapters.

The adhesion test data help to provide basic understanding to one of the fundamental issues in SU-8 based UV-LIGA -- the adhesion strengths of these commonly used metallic surfaces to SU-8. The analysis on the intrinsic physical/chemical mechanisms revealed a matrix of possible reasons for the discrepancies between the adhesion properties among these metallic materials, which provided a guideline for choosing and evaluating other metals when coating with SU-8 polymers. The knowledgebase established in this chapter serves as a preparation for future micro-transducer design and fabrication process [46].

CHAPTER 3. EXPERIMENT DESIGN AND UV-LIGA MICROFABRICATION FOR MEASURING FRACTURE TOUGHENSS OF NI MICROSTRUCTURES

3.1 Introduction

Knowledge of the mechanical properties of materials is indispensable in successful design, fabrication, as well as the reliability of MEMS components. Mechanical properties of bulk materials often can not be extrapolated to the scale of microsystems. The reason for the difference in properties is that the microstructures (grain structure, porosity, etc.) of these components fabricated with LIGA technique often vary significantly depending on the electroplating conditions, leading to different mechanical properties. In most cases, electroplating in micro-patterns, a key procedure in LIGA, is expected to produce nano-structured materials that may possess superior mechanical properties to these of their bulk counterparts. For example, due to small grain size, dislocation generation is less likely and yielding strengths may increase significantly. Thus, being able to first characterize the micro-structure materials, and then correlate processing parameters with the mechanical properties could help "tailoring" the materials to the specific requirements from the targeted applications.

So far, most of the previous and current efforts in the area of MEMS materials testing and characterization have concentrated on determining mechanical behavior of polysilicon [47-61]. In recent years, there have also been some reported efforts to study the material properties of LIGA produced micro-components. The reported measurements up to now have mainly

focused on electroplated nickel because it is the most commonly used metal in LIGA or UV-LIGA technologies. Nickel is known to have good mechanical properties and can be easily electroplated. Furthermore, these efforts on electroplated Ni have mostly been concerned with the tension and/or bending of beam specimens, and have resulted in values for the yield strength, ultimate tensile strength, and Young's modulus [62-71]. However, the fracture toughness of the microfabricated nickel structures has not been reported. For the microstructures involving mechanical movements, such as vibrations in a resonant devices, or micro-springs used for suspension and positioning purposes, micro-cracks at sharp corners may easily cause a mechanical failure with the structures undertaking stress. It is therefore very useful to know the fracture toughness of the microstructures made of electroplated nickel since the micro-actuator to be designed in this thesis might sustain large mechanical loading as well as contain structural defects.

The research work presented in this chapter focuses on development of an integrated experiment scheme and the micro-specimen fabrication procedure for the evaluation of fracture toughness of LIGA fabricated micro-specimens. The unique advantages of the presented specimen fabrication procedure and experiment scheme are: it does not need sample separation from the substrate and sample tests are in-situ, and the specimens have on-chip "guidance" to avoid sample wiggling and bending during the experiment. In particular, the research work includes: (a) the design and successful microfabrication of suitable free-standing, wafer-bound specimens; (b) a corroboration/validation of the compatibility of the samples and the design,

and set-up of suitable testing fixtures; (c) the testing of the UV-LIGA fabricated nickel micro-specimens and the associated fracture toughness calculation.

The devised testing mechanism demonstrated compatibility with the fabricated samples and capability of performing the desired experimentation by generating resistance-to-fracture values of the nickel specimens. The same experiment scheme and sample fabrication technology can be used in future work to study the fracture toughness value for LIGA fabricated samples of other metals and alloys.

3.2 Design and Microfabrication of Specimens

3.2.1 Design of the Specimens to Minimize Mechanical Handling

The basic criteria utilized to establish specimen size and specific geometry consisted of the following:

(a) Maximize the number of specimens per sample (substrate). Take advantage of the batch fabrication capability of UV-LIGA to produce arrays of equally dimensioned specimens fabricated simultaneously.

(b) Minimize or eliminate the need to handle the specimens after fabrication, thereby reducing the effect of associated disturbances and increasing the accuracy of results. The specimens were designed to measure fracture characteristics in pure tensile loading, which leads to opening or tensile failure mode, where the crack walls move directly apart from each other. Thus, the specimens should not be subject to any bending or torsion loads before or during testing. The simplest way to eliminate specimen handling is to keep them attached to the

substrate before and during testing. However, the specimens cannot remain completely attached to the substrate for the purpose of fracture testing. Therefore, the use of a sacrificial layer in the fabrication process became inevitable. The fact that the specimens must be partially attached to the wafer also determined the almost complementary relationship between the sample and the testing mechanism.

(c) Dimensionalize specimens based on "compact specimen" in ASTM standard E399 [72]. Due to the lack of standardization of mechanical property testing in microscale, the specimen design followed a proportional reduction of the ASTM fracture toughness standard specimen dimensions to insure adequate microsizes of specimen features (especially the notched area).

(d) Design specimens to accommodate the testing mechanism. The mechanism employs a loading pin to apply the necessary force; hence, the specimens were designed with a corresponding perforation for this purpose. The use of a tension testing clevis was considered, as indicated in ASTM standard E399 for the testing of compact specimens [72]. However, the reasonable thickness limitations of the electrodeposited sacrificial layer did not allow for a sufficient gap to properly insert a clevis.

All of the specimens had one end attached to a large block of electroplated Ni while the remaining part of the body was free to move above the wafer in a cantilever type of design. An opening at the unrestricted end was designed to permit insertion of a high stiffness needle for load application. The large block of electroplated Ni was intended to provide enough adhesion

force between the samples and the substrate, and to prevent them from detaching during testing. The required size of this adhesion block was estimated using a reasonable safety factor considering the total area of all specimens and the electroplating current limitations.

Figure 3-1 shows the configuration and dimensions of the fracture specimen. It includes a notched area (the fracture section), a pinning end where the sample could be hooked with the test system, and two guiding blocks to prevent in-plane bending during testing. The sample was designed to have a sharp notch to eliminate fatigue growth (Stage I – initiation). The length of the stem was designed to provide sufficient distance between the notched area and the pinning end for observation/recording purposes. The stem extends the point of force application a certain distance away from the notched area while maintaining the same line of force application as specified in the "compact specimen" design of ASTM E399 [72]. The length of the stem was determined by means of a simple beam deflection calculation, taking into account gravity and allowing for a deviation of up to 2 μm. A safety factor of 1.25 was included in the calculation. The width of this part is equivalent to the size of the opening in the pinning end.

3.2.2 Microfabrication of Specimens

Devising a suitable fabrication strategy involved experimenting with different techniques, and combinations thereof, to produce a final sequence deemed most appropriate for the research needs. This course of action was critical to establish the three major microfabrication steps involved (structural layer, sacrificial layer, and substrate), the details of which are described below.

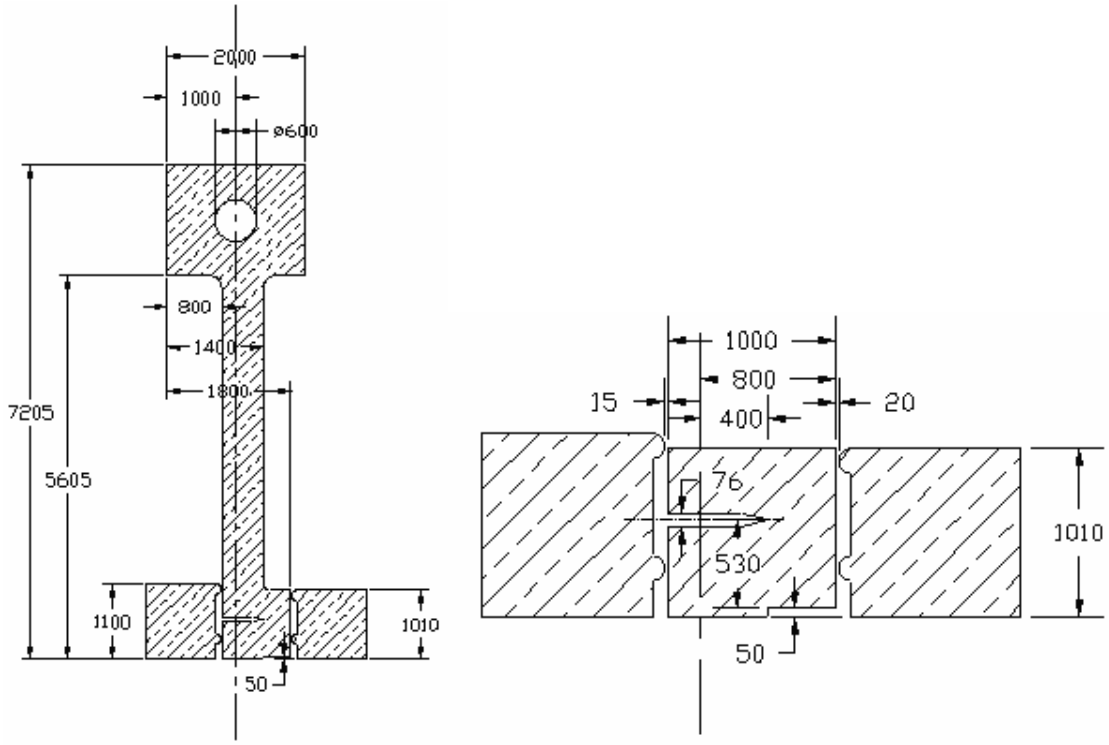

(A) (B)

Figure 3-1 The schematic design of the test sample (unit: μm) (A) Detailed design of the sample; (B) Zoom-in diagram of the notch design

The fabrication of the samples required three optical masks, two thick SU-8 layers, and two layers of electroplated metal. The fabrication flowchart as shown graphically in Figure 3-2 was followed. The fabrication sequence (starting after the completion of the substrate preparation) is outlined below:

(1) Thin layers of Cr and Au were coated on the surface of the substrate as the seed layer for electroplating and enhancing the adhesion.

(2) 90 μm thick film of SU-8 was spin-coated onto the wafer and pre-baked for 80 minutes at 96 ^{0}C.

(3) The SU-8 was exposed with a near-UV light source using the mask designed. Post-baking of the photoresist was done to induce cross-linking, followed by prudent relaxation time. The SU-8 film was then developed in Nano SU-8 Developer for 20 minutes, rinsed in IPA and DI water, and blown dry with nitrogen gas. Film residue removal from the substrate was performed using oxygen plasma asher.

(4) The copper sacrificial layer was electrodeposited. The sacrificial layer was then manually and mechanically leveled to the height of the photoresist, followed by a DI water rinse and N_2 blow-dry.

(5) The SU-8 plating pattern was removed by means of immersion in a heated (60 ^{0}C) bath of Dynalsove 185 (for 2-3 hours). Consecutive IPA rinsing and nitrogen gas blow-drying were performed. The substrate was placed in an oxygen plasma source to eliminate film residue and promote adhesion between the sacrificial layer and the subsequent SU-8 film.

(6) An about 400 μm thick structural layer of negative photoresist was spin-coated onto the sacrificial layer using SU-8 100 at the speed of 900 rpm and pre-baked for 6.5 hours.

(7) The SU-8 resist was lithographically patterned with a near-UV light source utilizing the negative UV-mask. After post-baking and developed in Nano SU-8 Developer, film residue removal from the substrate was again performed by oxygen plasma.

(8) The nickel structures were electrodeposited. Mechanical leveling and polishing of the metal structures were also carried out.

(9) The remaining SU-8 plating pattern was stripped in a heated bath of Dynalsove 185. The process was same as in step (5), but with much longer bathing time (4-5 hours).

(10) Specimen release was achieved by wet etching of the copper sacrificial layer. Removal of the remaining SU-8 structural layer was attempted again by means of immersion in a heated bath of Dynalsove 185.

The UV lithography of ultra thick SU-8 resist is a challenging issue. The processing parameters as provided by Williams and Wang [39] were used to obtain excellent sidewall quality. How to strip cured SU-8 polymer completely is another challenging task in SU-8 based UV-LIGA process. In the work presented here, plasma asher was used to clean out any residual polymer in these samples after stripping with Dynalsove 185.

The electroplating setup consisted of an electroplating tank (Nalgene, Rochester, NY), an electroplating tank cover and holder, an anode, a water bath (Lindberg/Blue, Asheville, NC) to maintain constant temperature, a Potentiostat/Galvanostat (EG&G, Gaithersburg, MD), a filtration device composed of a dispensing pump (Watson Marlow, Baton Rouge, LA) with the corresponding filtering hose and filter paper, a level controlling system consisting of a pinch valve (Cole Parmer, Vernon Hills, IL) with a level sensor (Cole Parmer, Vernon Hills, IL) and a dispensing reservoir, and a Lab Stirrer (Yamato, Japan). Mechanical agitation and filtration of the bath were performed continuously throughout the electrodeposition process. Agitation results in improved stability and controls of the thickness of the mass transport boundary layer. Filtration removes unwanted substances from the electrolyte.

Electrochemically deposited copper was employed as a sacrificial layer in the specimen fabrication process. Thus, the deposition technique was aimed to benefit the uniformity and adhesion of the coating to the substrate rather than focusing on the specific structure and properties of the copper deposit. Copper was electrodeposited at a current density of 15 mA/cm^2 for 9 hours at room temperature to obtain a sacrificial layer height of 90 μm.

The solution of choice for electroplating Ni is nickel sulfamate. This general purpose bath has a wide operating range, produces low stress deposits, and is easy to control. The bath was an aqueous nickel sulfamate solution prepared by mixing the appropriate components according to the proportions specified in Table 3-1, and adding DI water until the total volume was 6 liters. Lauryl sulfate was added as a wetting agent, to increase the throwing power of the solution. Boric acid is the most commonly used buffering agent for nickel plating baths. It is effective in stabilizing the pH in the cathode film within the ranges normally required for best plating performance. The nickel sulfamate anode utilized consisted of sulfur-activated electrolytic nickel rounds (Belmont Metals, Brooklyn, NY) inside a titanium basket encased in a cloth anode bag. The rounds had a unique shape ideal for plating with baskets.

The calculations required for the electrodeposition included the estimation of the total area to be plated and the amount of time necessary to achieve a certain film thickness. The addition of appropriate specimen dimensions yielded a total surface area of 2.11 cm^2. The total current applied was determined by multiplying the current density by the surface area. Subsequently, the time needed to produce the desired 400 μm thick nickel samples at a rate of 10 mA/cm^2,

including a factor of about 10% overplating necessary for uniform height of structures after lapping, was predicted to be approximately 36 hours. The plating conditions are provided in Table 3-2.

Figure 3-3 shows pictures of a test sample. The cantilever-type structure is released from the substrate for most part with end of notched section affixed to the substrate. Figure 3-3 (A) is the complete sample, and Figure 3-3(B) shows the notch and the guiding blocks of the sample.

The errors in lithography process may cause the final dimension of the samples to be different from what was designed. Table 3-3 shows the percentage deviation of measured values from the nominal design values for some dimensions. These dimensional changes can be attributed to the fact that the SU-8 photoresist undergoes significant chemical changes during UV exposure, where the photoinitiator generates an acid to facilitate the polymeric cross-linking, causing the photoresist to distend. The percentage deviations measured were consistent with the previously mentioned swelling effect and ranged from -4 to 4%.

Table 3-1 Nickel Sulfamate electroplating bath composition

Component	Chemical formula	Quantity in solution	Manufacturer
Nickel sulfamate	$Ni(SO_3NH_2)_2$	2700 mL	Alfa Aesar, Ward Hill, MA
Boric acid	H_3BO_3	225 g	Fisher Scientific, Fair Lawn, NJ
Lauryl Sulfate	$C_{12}H_{25}O_4SNa$	6 g	Sigma, St. Louis, MO

Table 3-2 Nickel electroplating parameters

Bath	Temperature	Operating mode	Time	Current density (mA/cm^2)	pH
Nickel Sulfamate	55 °C	Galvanostatic	36 hours	10	3.80-3.92

Table 3-3 Relative dimensional changes caused by the fabrication process

Dimension	Nominal (μm)	Average actual values (μm)	Percentage deviation (%)
Total notch length (*l*)	600	577.4	-4
Notch width	76	79	+4
Specimen dimension (*d*)	1000	986.4	-0.94

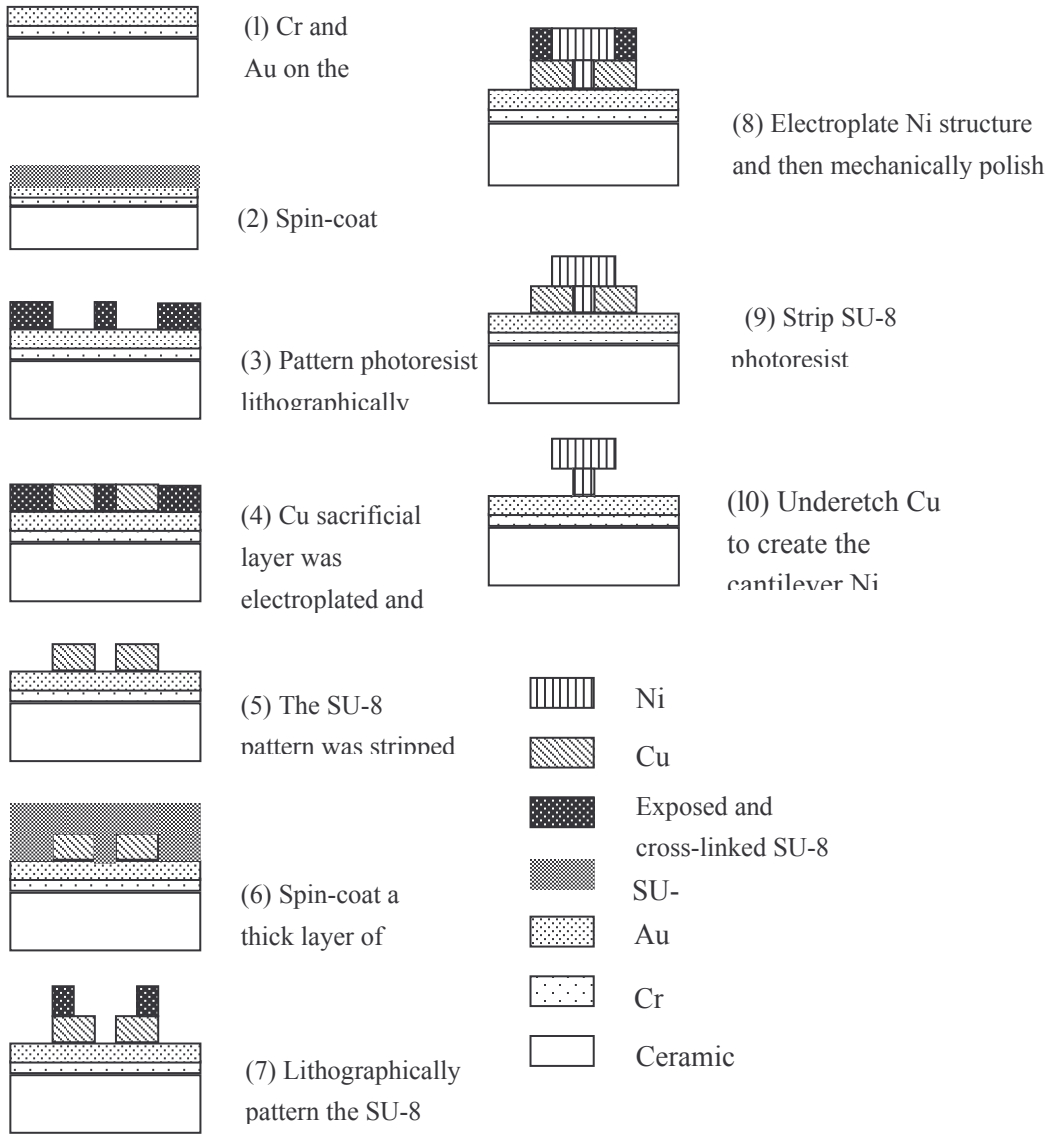

Figure 3-2 Fabrication sequence of the test sample

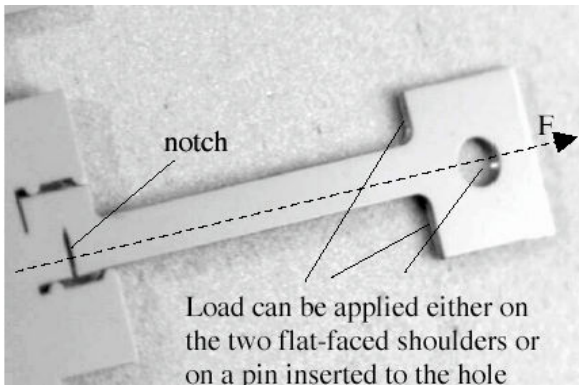

(A)

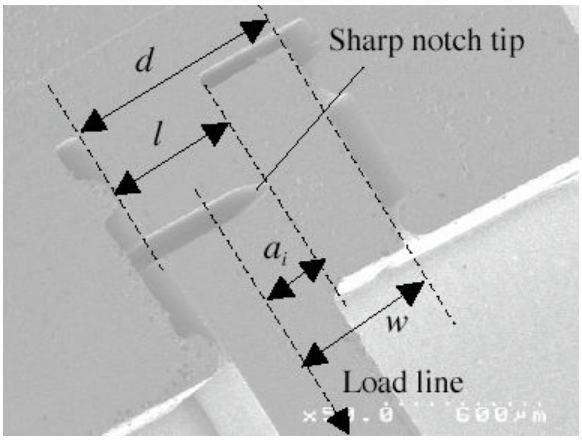

(B)

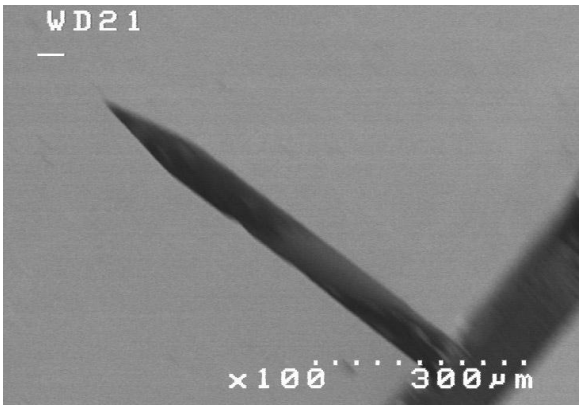

(C)

Figure 3-3 Pictures of a fracture toughness test sample (A) Top view; (B) SEM image of the notched and guidance section; (The load was applied along the direction of the arrowed line); (C) SEM image of the notch

3.3 Experiment Design and Results Analysis

3.3.1 Experimental Setup

Figure 3-4 shows the schematic diagram for the testing setup. The testing mechanism can be divided into two distinct assemblies according to the functions performed: (a) motion and loading, (b) measuring and recording.

The motion and loading assembly consisted of a model 200B air bearing with modified slider (Nelson Air Corp., Milford, NH), a PM500-C precision motion controller (Newport Corp. Irvine, CA), a loading pin arm (Mechanical Engineering Machine Shop, Baton Rouge, LA), a Prima 3-jaw drill chuck (Rohm Products of America, Lawrenceville, GA), and a pin gage (Vermont Gage, Swanton, VT). The measuring and recording assembly was comprised of an MDB-25 load cell (Transducer Techniques Inc., Temecula, CA), the Wafer Analysis System (WAS) software (CAMD, Baton Rouge, LA), a PCMCIA-232 data acquisition card (DAC) (National Instruments, Austin, TX), and Plug-n-Play General Purpose Interface Bus (GPIB) (National Instruments, Austin, TX).

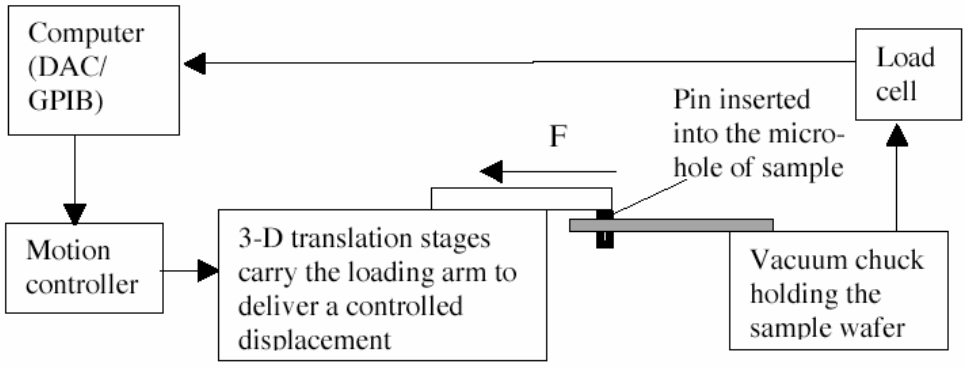

Figure 3-4 The set-up of the fracture toughness experimental system

With this mechanism, the wafer with arrays of samples was loaded on a vacuum chuck. A three-D translational system was used to carry the loading arm. A specially designed holder was designed and machined to hold and pull the sample on the left and right shoulders. A pulling force was applied to the sample by delivery of controlled displacement. The actual load delivered to the sample was monitored using the load cell. The output signal of load cell was fed to the data acquisition board of a computer.

3.3.2 Test results and Discussions

In the conventional fracture toughness tests, micro-cracks were created on the notches by fatiguing the samples before a tensile load is applied. For the micro-sized samples in this study, this approach is both impractical and not necessary. The sharp corner created at the end of the notch is already very sharp and it is not necessary to create additional cracks. The study reported by Lee et al. [60] proved that as the notch radius in a linear elastic body becomes small in comparison to the crack, it is possible to measure the fracture toughness by considering the notch effect without pre-crack formation. It was suggested that fracture toughness may be independent of the notch radius below a critical value, in their case, a notch tip radius of 2 μm [60]. From the SEM images shown in Figure 3-3(C), it can be seen that the notch in specimen is very sharp. The notch tip radius is essentially determined by the limit of the UV lithography process at about 2-5 μm. In our tests, the notch is therefore assumed to be sharp enough for fracture toughness measurement without pre-cracks. Kahn et al. [61] reported that different values of fracture toughness were obtained for silicon with pre-cracked ones and oxidizations

might also affect measured values. In this research, the material under study, nickel, is isotropic in comparison with silicon. In addition, oxidized thin film is always present in nickel and therefore should not be a significant factor.

In the test, a controlled displacement was delivered using the translation stage at a speed of 10 μm per second. The specially designed holder, a high strength steel bar of 5 mm in diameter, applied the load to the two flat-faced shoulders as shown in Figure 3-3(A). As the load is applied along the direction of the arrow line shown in Figure 3-3(A) and (B), and reaches the fracture toughness of the electroplated Ni, crack starts to propagate from the sharp opening at the end of the notch. Figure 3-5 shows a combined SEM image of the broken cross-section at the notch of a specimen.

The critical load and the notch displacement are two key parameters for fracture toughness measurement. The load was monitored in real time with an accuracy of 0.056 N. The translation stage used in the experiment has a resolution of 150 nm. Ideally, it would be preferred to directly monitor the notch displacement in real time. However, the limited operation space and required accuracy made this difficult to achieve. Instead, a careful displacement analysis was utilized to determine the notch displacement with reasonable accuracy.

The mechanical holder (a 5 mm diameter steel bar) is much more rigid than the specimen and its deflection is neglected in the total displacement. The displacement L delivered by the translation stage is therefore equal to the sum of the notch displacement L_n and the extension L_s of the specimen under load,

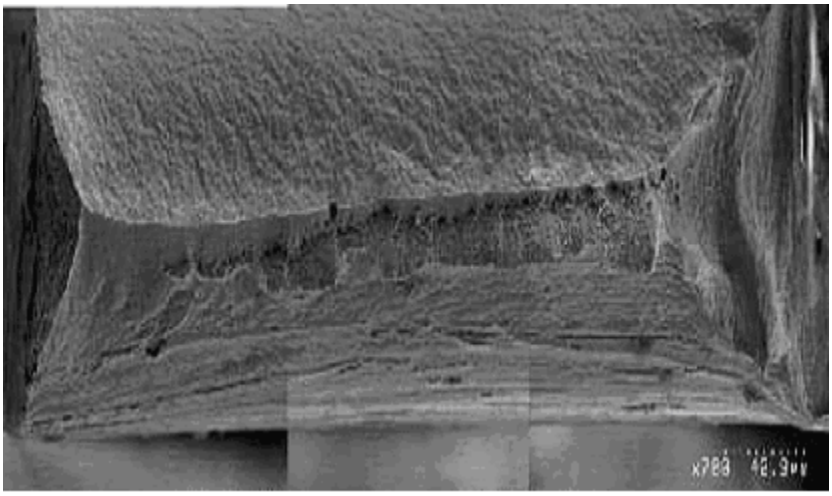

Figure 3-5 The cross-sectional image of a broken test sample. The crack initiated from the right side and propagated to the left side.

$$L=L_n+ L_s \tag{3.1}$$

Using Young's modulus of 153 GPa for electroplated Ni as suggested by Kelly et al. [70], the extension of stem section of a typical sample under load can be estimated as 0.122 μm/N. At load of 75 N, this would result in an elongation of about 9.15 μm, which represents an error of about 1.7% for a total displacement of 550 μm. For any given load P_q, this error can easily be compensated using the following relationship,

$$L_n = L - L_s = L - 0.122P_q \tag{3.2}$$

Figure 3-6 shows the plots of the forces versus notch displacements measured in the experiments. The error caused by the stem section elongation has been compensated.

The following equation as suggested by ASTM Standards for the type of notch used in this study [72] was used to calculate the fracture toughness:

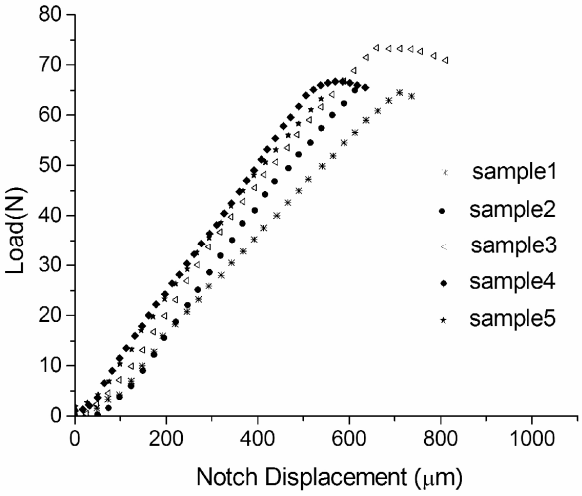

Figure 3-6 Experimental results showing force vs. notch displacement

$$K_Q = \frac{p_Q}{t\sqrt{w}}(0.866 + 4.64\alpha - 13.32\alpha^2 + 14.72\alpha^3 - 5.6\alpha^4)\frac{2+\alpha}{(1-\alpha)^{1.5}}, \qquad (3.3)$$

where $\alpha = \alpha_i / w$, α_i is the initial cracking length, t is the thickness of the specimen, and w is the width of the specimen. Because the pre-cracking was impractical for this micro-scale specimen, the stable crack growth as described in ASTM standard [72] for macroscopic specimen was not observed, as shown in the load-displacement plot as the single sudden drop in load before final fracture preceded by an almost linear curve. The maximum loads were therefore used as the fracture load (p_Q) instead of adapting the 95% compensation for the slope [72].

Utilizing the experimental results as plotted in Figure 3-6 and Eq. (3.3), the fracture toughness of these samples are calculated and listed in Table 3-4. These fracture toughness values are for UV-LIGA fabricated nickel specimens of the particular design, and under the specific electrodeposition conditions as presented in the previous section. The dimensions of

the specimens were also measured using Nikon MM-22U Measuroscope and were listed in the table. The average value of the fracture toughness is 53.39 MPa$\sqrt{m}$, with standard deviation of 2.30 MPa$\sqrt{m}$. More experiments are needed to establish database for other properties of electroplated Ni microstructures [6].

Table 3-4 Sample dimension and fracture toughness

	Notch depth (μm)	Sample width (μm)	α	Sample thickness (μm)	Maximum load (N)	Fracture toughness (MPa$\sqrt{m}$)
Sample1	359	760	0.472	389	64.506	52.65
Sample2	379	790	0.480	396	65.807	52.98
Sample3	383	787	0.487	407	72.155	57.82
Sample4	376	795	0.473	397	66.817	52.40
Sample5	390	800	0.488	404	63.643	51.12
Average	377.4	786.4	0.48	398.6	66.586	53.39
Standard Deviation	10.3	13.9	0.007	6.35	3.0	2.30

CHAPTER 4. MECHANISMS AND STRUCTURE DESIGNS OF COMB DRIVE MICRO-ACTUATOR

4.1 Comb Drive Mechanical Response Modeling

A typical comb-drive actuator with the classical folded-beam suspension is shown in Figure 4-1 [15]. The dark areas represent the anchors that are fixed and the grey areas represent the suspended parts, which include the comb drive structure and the spring system. In this section, we discuss the electro-mechanical principles of comb drive micro-actuators. For simplicity, fringing field effects in comb-drive structures has been neglected. The moving fingers and fixed fingers can be abstracted as two parallel plates forming a capacitor when an external voltage is applied, as shown in Figure 4-2.

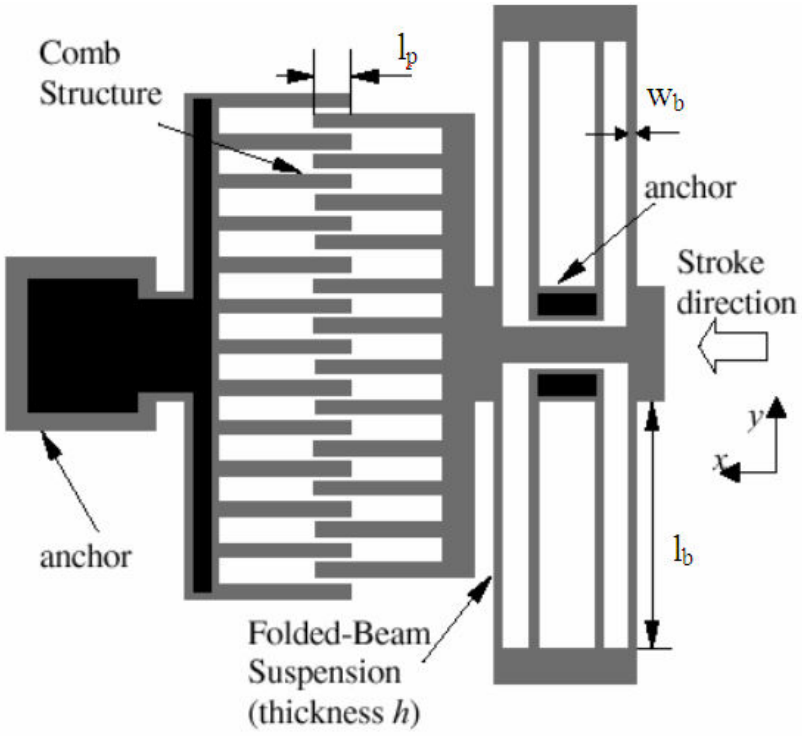

Figure 4-1 A typical comb-drive actuator

The equivalent capacitance for each parallel plate unit can be calculated by

$$C = \frac{\varepsilon_0 A}{g} = \frac{\varepsilon_0 l_p h}{g} \tag{4.1}$$

where C is the capacitance, ε_0 is the permittivity constant of air, A is the overlapping area between the two plates, g is the distance between the two plates, l_p is the overlapping length, and h is the height of the plate, respectively.

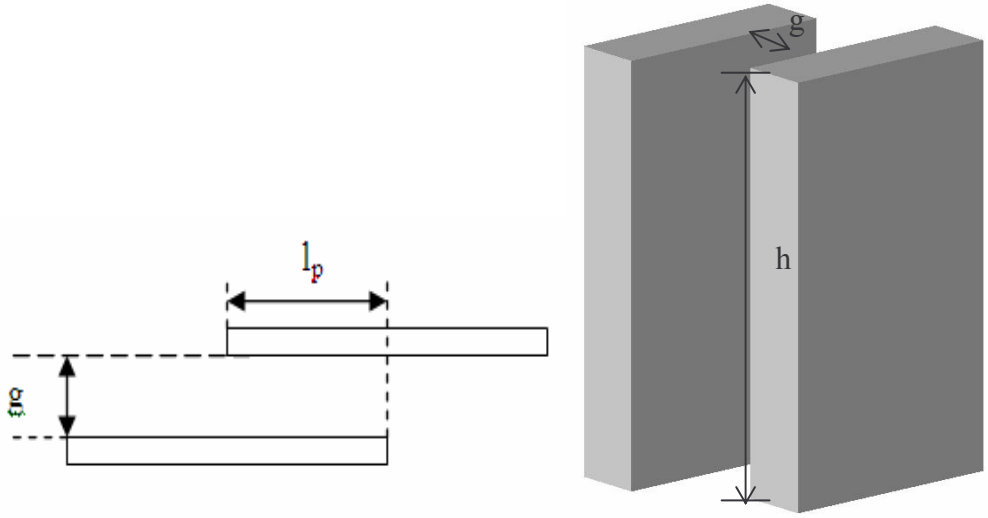

(a) (b)

Figure 4-2 Schematic illustration of the parallel plates

When a voltage is applied, the electrostatic energy contained in the two parallel plates is

$$W = \frac{1}{2} C V^2 = \frac{1}{2g} \varepsilon_0 l_p h V^2 \tag{4.2}$$

where W is the stored energy and V is the driving voltage, respectively.

Assuming g and h are fixed, and the variation of l_p along the x direction is denoted by x, the total energy change is:

$$W = \frac{1}{2g} \varepsilon_0 x h V^2 \tag{4.3}$$

When the voltage is constant, the electrostatic force is given by

$$F_x = \frac{\partial W}{\partial x} = \frac{1}{2g}\varepsilon_0 h V^2 \tag{4.4}$$

where F_x is the electrostatic force along the x-direction.

In a comb drive structure with multiple fingers, each pair of the fingers forms a capacitor. The total capacitance can be calculated as the capacitance of a set of parallel capacitors. Hence, the total electrostatic force is

$$F_x = \frac{N}{2g}\varepsilon_0 h V^2 \tag{4.5}$$

where N is the number of comb drive finger units.

The absence of the displacement variable x in the above equation indicates one of the most attractive features of this lateral comb dive design: constant driving force that is independent of the displacement x, as long as x is less than the overlapping length l_p under the constant bias voltage.

A typical design of comb drive micro-actuator consists of the comb drive structure, the spring system (several designs of which will be discussed later), and the driving mass. The suspended comb fingers connect the spring system to the driving mass. Driven by the electrostatic force generated from the comb drive structure, the suspended comb fingers move the mass, leading to the vibration of the mass as the driving voltage is applied. As the spring system deforms, the elastic reaction force is generated in the opposite direction, pushing the comb fingers towards to original equilibrium position. The kinetics of the micro-actuator is

decided by the balance between the electrostatic force and the elastic reaction force. Therefore, the system can be simplified as a 1-D spring-mass system as shown in Figure 4-3 [73]. The simplicity of the resulted model allows a simple analytical kinetic equations to be formulated as

$$F_x - K_x x = M\frac{d^2x}{dt^2} \tag{4.6}$$

where K_x is the elastic modulus of the springs in the x-direction and M is the equivalent mass of the driving mass. The equation completely describes the dynamics of the micro-actuator. By solving the ordinary differential equation, the comb finger displacement x at any given time instance t and the system's natural frequency can then be calculated by:

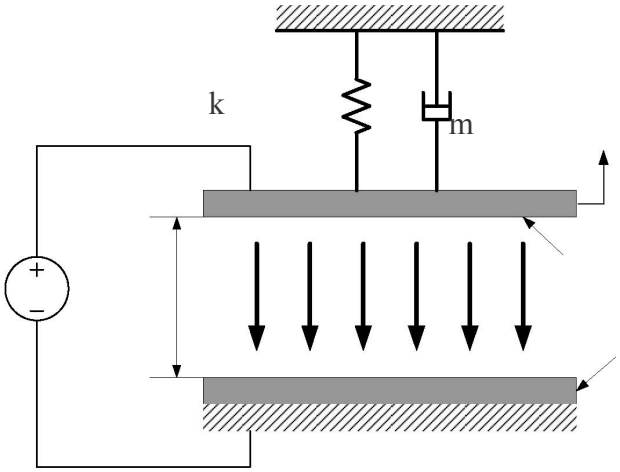

Figure 4-3 Model of the spring-actuator configuration

$$x = \frac{F_x}{K_x}(1-\cos\omega t) = \frac{N}{2gK_x}\varepsilon_0 hV^2(1-\cos\omega t) \tag{4.7}$$

$$\omega = \sqrt{\frac{K_x}{M}} \tag{4.8}$$

$$f_n = \frac{1}{2\pi}\omega = \frac{1}{2\pi}\sqrt{\frac{K_x}{M}} \tag{4.9}$$

If the overshooting is not considered, the ideal maximum displacement is

$$x_{\max} = \frac{\mathrm{F_x}}{K_x} = \frac{N}{2gK_x}\varepsilon_0 hV^2 \tag{4.10}$$

4.2 Designs of the Suspension Springs (K_x)

The foregoing analysis is based on the assumption that the movable finger structure does not move along the y-direction. In reality, there is substantial driving force in the y-direction (gap-closing driving force) between the two fingers if the gap is very small. The gap-closing driving force could be self-balanced if the movable fingers remain precisely at the center between the two neighboring fixed fingers. Obviously, the required level of precision can hardly be met in fabrication. Even if such restrictive condition is satisfied, the forces at the ends of finger array cannot be completely balanced. Consequently, if the driving voltage is too high or the end fingers are too thin, the fingers may be clamped together resulting in short circuit, often called the pull-in problem [25]. Furthermore, any perturbation from the center fingers, such as rotation or offset from center point, can lead to instability. Therefore, special attention should be paid in the design to contain the possible pull-in instability.

Many methods have been proposed in the literature to calculate the severity and to control the instability [18,23,74-76]. In most methods, the stability is achieved by designing the spring constant to satisfy

$$K_y > \frac{2\varepsilon_0 h l_p V^2}{g^3} \tag{4.11}$$

or

$$K_y >> \frac{x^2 K_x}{g^2} \tag{4.12}$$

where K_y is the spring constant in the y-direction. It is therefore highly desirable to have the spring very compliant in one direction (the targeted moving direction) and stiff in the orthogonal direction at the same time.

Different types of spring designs have been used in comb drive micro-actuators. Among them, four spring designs are most often adapted: clamped-clamped beams, crab-leg flexure, basic three folded cantilever beams, and folded-beam flexure. The first two structures are illustrated in Figure 4-4(a) and (b) [77], and the latter two structures are introduced in details in the following sections.

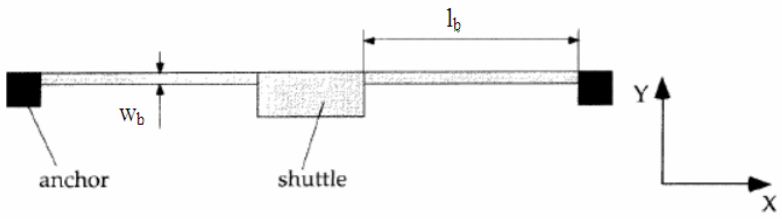

(a) clamped-clamped beams

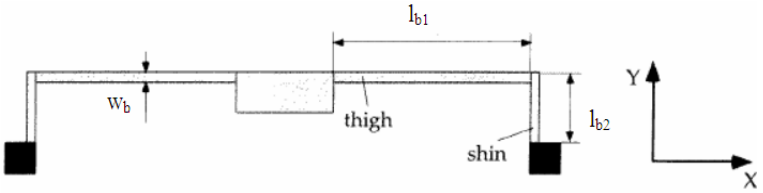

(b) crab-leg flexure

Figure 4-4 Designs of springs (a) clamped-clamped beams and (b) crab-leg flexure

The main drawback for clamped-clamped beams and crab-leg flexure is that they are not suitable for large displacement due to the larger non-linear force vs. displacement relationship and the large reduction in the stiffness ratio. Therefore, they are not investigated in this study.

4.2.1 Basic Three Folded Cantilever Beams

The first approach is based on the basic three folded cantilever beams. The method of determining the spring parameters is discussed in this section. In our design, each segment of the spring has the same width and thickness. The lengths of different segments of the spring are represented by a and b, respectively, as shown in Figure 4-5 [77].

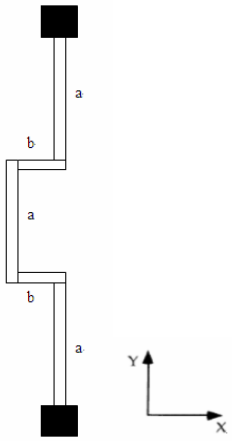

Figure 4-5 Schematics of three folded cantilever beams

With F_x and F_y denoting the lateral and transversal forces resulted from the spring respectively, M denoting the resulted spring end moment, and x denoting the distance from the end of each segment, the moment in each segment can be written as

$$M_1 = F_x \times x + M \qquad x:(0,a) \tag{4.13}$$

$$M_2 = F_x \times a - F_y \times x + M \qquad x:(0,b) \tag{4.14}$$

$$M_3 = F_x \times (a+x) - F_y \times b + M \qquad x:(0,a) \tag{4.15}$$

$$M_4 = F_x \times (2a) - F_y \times x + M \qquad x:(0,b) \tag{4.16}$$

$$M_5 = Fx \times (2a+x) + M \qquad x:(0,a) \tag{4.17}$$

$$W = \int \frac{M^2}{2EI} dx \,,$$

$$= \frac{1}{2EI} \int_0^a M_1{}^2 dx + \int_0^b M_2{}^2 dx + \int_0^a M_3{}^2 dx + \int_0^b M_4{}^2 dx + \int_0^a M_5{}^2 dx \tag{4.18}$$

where M_i is the moment in each segment, E is the material's Yong's modulus, and I is the moment of inertia of the cross section, which can be calculated from

$$I = \frac{1}{12} w_b{}^3 h \,, \tag{4.19}$$

where w_b and h are the width and thickness of the beam, respectively.

Taking the derivative of the elastic energy against the applied forces, the respective displacements are calculated as

$$\frac{\partial W}{\partial \mathrm{F_x}} = x \quad , \quad \frac{\partial W}{\partial \mathrm{F_y}} = y \quad , \quad \frac{\partial W}{\partial \mathrm{M}} = \theta \tag{4.20}$$

where x and y are the displacements along the x and y directions respectively, and θ is the rotation angle at the end of the spring. In order to maintain the stability, y must be equal to or near zero. In addition, the rotation angle at the spring end should be zero since the spring and the mass are one piece. Both of two restraints confirm to the structure symmetry requirement.

Substitute Eqs. (4.13) - (4.19) into Eq. (4.20), we obtain

$$\frac{18a^3\mathrm{F_x} + 10\mathrm{a}^2 b\mathrm{F_x} - 3\mathrm{a}^2 b\mathrm{F_y} - 3\mathrm{ab}^2\mathrm{F_y} + 9a^2 M + 6abM}{2\mathrm{EI}} = x \tag{4.21}$$

$$\frac{-3a^2 b\mathrm{F_x} - 3\mathrm{ab}^2\mathrm{F_x} + 2\mathrm{ab}^2\mathrm{F_y} + \frac{4b^3\mathrm{F_y}}{3} - 2abM - 2b^2 M}{2\mathrm{EI}} = 0 \tag{4.22}$$

$$\frac{9a^2 F_x + 6abF_x - 2abF_y - 2b^2 F_y + 6aM + 4bM}{2\mathrm{EI}} = 0 \tag{4.23}$$

Solving Eqs. (4.21) - (4.23) by eliminating F_y and M, the displacement x is calculated as

$$x = \frac{(4.5a^3 + a^2 b)F_x}{2EI} \tag{4.24}$$

According to the Hooke's law, the spring constant can be derived as

$$K_x = \frac{F_x}{x} = \frac{Ehw_b^{\ 3}}{27a^3 + 6a^2 b} \tag{4.25}$$

Evident from the analysis, once the values of a and b are given, K_x is uniquely determined by the thickness and width of the beam. The relationship between K_x and a, b is shown graphically in the Figure 4-6.

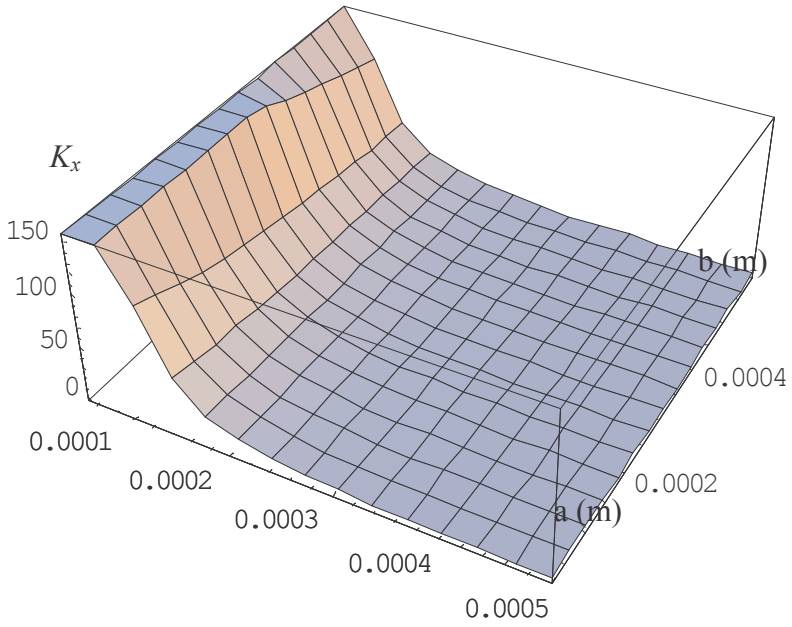

Figure 4-6 The relationship between spring stiffness K_x and values of *a, b*

Figure 4-6 indicates that a has much larger influence on the spring constant than b, also evident from Eq. (4.25). Therefore, long segment length should be chosen to archive the desired large spring constant.

4.2.2 Folded-beam Flexure

The stability margin requires the spring to possess very compliant spring constant in one direction, while be stiff in the orthogonal direction at the same time. This characteristic can be achieved by the folded-beam flexure structure.

A sketch of the folded beam design is shown in Figure 4-7. The beams are anchored near the centre and the trusses allow expansion or contraction of the beams along the *x*-axis. Assuming rigid trusses, the spring constant of the folded flexure design in the axial and lateral directions can be calculated by

$$K_x = 2Ehw_b^{\,3} / l_b^{\,3} \tag{4.26}$$

$$K_y = 2Ew_b h / l_b \tag{4.27}$$

where l_b is the length of the spring.

The stiffness ratio between the two orthogonal directions depends on the relationship between w_b and l_b, which is given by

$$\frac{K_y}{K_x} = (\frac{l_b}{w_b})^2 \tag{4.28}$$

Usually, the stiffness ratio is chosen sufficiently high so that the structure is much more rigid in the y direction than in the x direction. In other words, the displacement in x direction should be much larger than that in y direction. Under this condition, we can assume that there is no displacement in y direction, and thus neglect the y direction stiffness K_y. Based on this assumption and according to the equation (4.26), we can achieve desired K_x by choosing appropriate values for w_b and l_b.

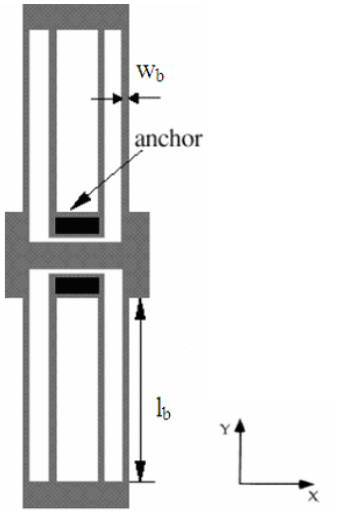

Figure 4-7 Folded-beam flexure

4.3 Structure Design and Analysis

The two spring designs discussed above and related finite element (FEM) simulation results are presented in this section. The material used is SU-8 photoresist. The density is $\rho = 1.164 g/cm^3$ and Young's modulus is estimated as $E = 4.4 Gpa$. The spring constants K are calculated from the method given in previous sections from the given geometries of the springs. The maximum displacements under a constant voltage are calculated and the fundamental frequencies in dynamic situation are estimated.

4.3.1 Basic Three Folded Cantilever Beams

To keep the structure stable in y direction, the symmetric structure is used in our design as shown on Figure 4-8. Table 4-1 lists different sizes and properties of the comb-drive structures for the basic three folded cantilever beams spring under the conditions of V=100 volts. For example, if we choose *a* as 500 μm and *b* as 1000 μm. Considering processing limitations and

operation convenience, the width of the beam and the height of the beam are chosen as 20 μm and 400 μm respectively. According to the equation (4.25), the spring constant K_x is calculated as 2.89 N/m for spring with one folding, as shown in Figure 4-5. In the case that the spring has two folding, as shown in Figure 4-9, the spring constant K_x could be derived similarly as in section 4.2.1, at 0.46 N/m. Table 4-1 shows the results calculated for the two folding spring structure, in which K_x represents the collective stiffness of the four springs. If the rectangle mass is designed as 1600 μm long and 2000 μm wide, the mass comes out at 1.485 mg. When the width and gap of fingers are both 20 μm, with thickness of 400 μm and length of 250 μm, the design realizes a maximum displacement of 38.48 μm for the 80 comb drive units at a voltage of 100 V, as shown as the 4th row in Table 4-1. The same configuration was also simulated with finite element simulation (FEM). The commercial software, ***ANSYS***, was used. The results are shown in Figure 4-9 and 4-10. The simulated relationship between displacement and applied voltage are in good agreement with analytical solution. The analytical solution slightly over predicted the spring stiffness because the spring beam width was simplified as a line in the analytical solution.

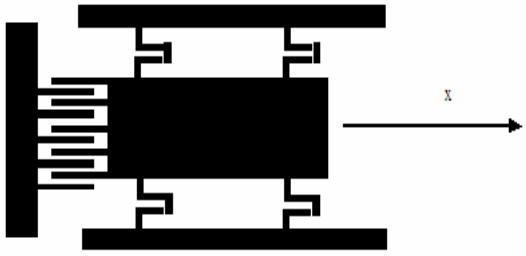

Figure 4-8 Comb drive actuator with basic three folded cantilever beams

Table 4-1 Properties of the basic three folded cantilever beams design

	g (μm)	h (μm)	Mass (mg)	N	K (N/m)	X_{max} (μm)
1	20	400	1.147	20	1.85	9.59
2	30	400	3.542	40	1.84	12.78
3	15	400	1.147	20	1.84	12.78
4	20	400	1.485	80	1.84	38.48

4.3.2 Folded Beam Flexure

The comb drive was designed to have 160 capacitor units with a height of 400 μm, a width of 40 μm, and the air gap at 20 μm. The beam width and length are 40 μm and 1800 μm respectively. For the cured SU-8 polymer with mass density $\rho = 1.164 g/cm^3$ and Young's modulus $E = 4.4 Gpa$, K_x is calculated to be 38.63 N/m using equation (4.26). With a mass of 4.050 mg, the maximum displacement and natural frequency of the micro-actuator can be estimated as 14.663 μm using a driving voltage of 200 volts.

The behavior of the folded beam spring was also numerically simulated by finite element analysis (FEA), and compared with the analytical solution. The commercial software, ***ANSY***S, was used. In Figure 4-11, the simulated displacement of the end of the spring is 14.749 μm which is very close to what was predicted by the analytical method.

The relationships between the driving voltage and displacements of spring designs with two different sizes were simulated using FEM and ploted in the same figure with the ones obtained using analytical solutions in Figure 4-12. The FEM simulations are in excellent agreement with analytical solutions. It also confirms that the spring with higher stiffness ratio generates larger displacement with the same driving voltage.

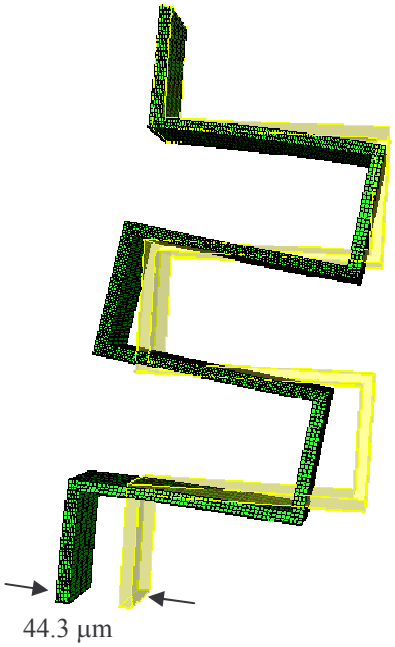

Figure 4-9 FEM numerically simulated spring deflection for basic folded cantilever beam spring structure

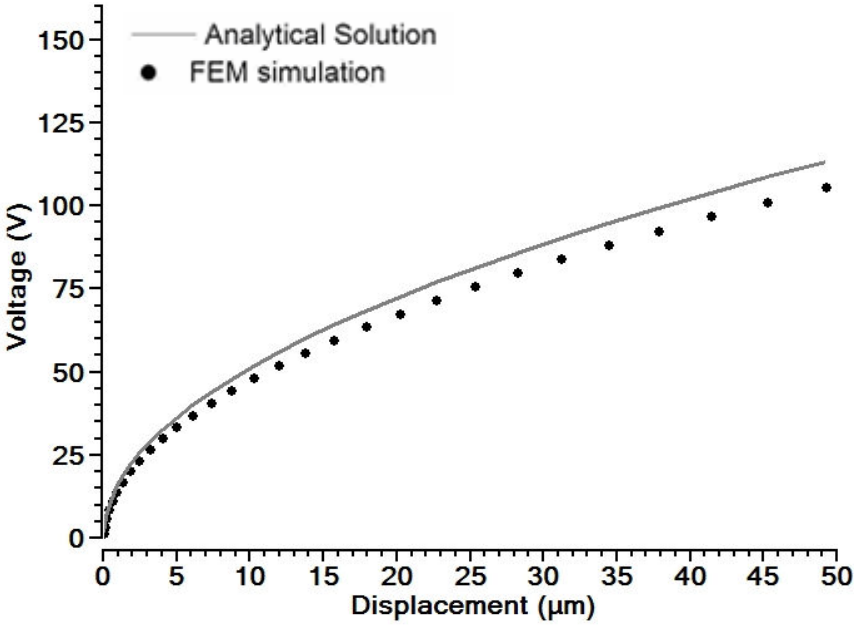

Figure 4-10 The simulated relations between applied voltage and displacements for basic folded cantilever beam spring structure

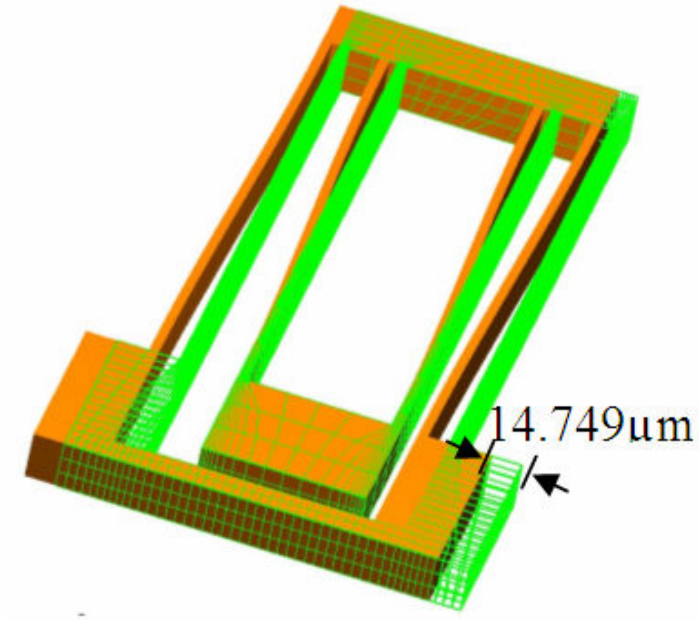

Figure 4-11 FEM numerically simulated spring deflection for folded beam spring structure

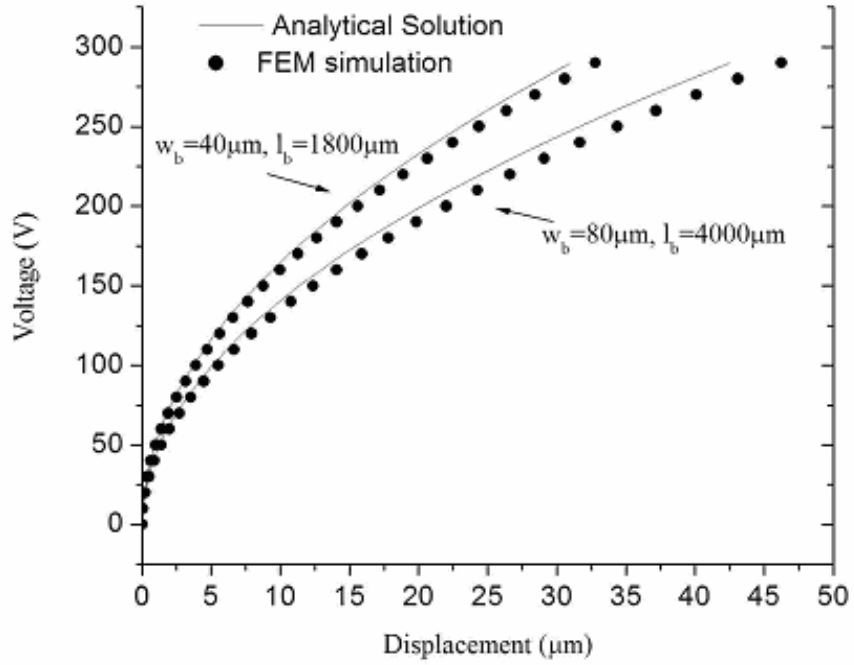

Figure 4-12 The simulated relations between applied voltage and displacements for folded beam spring structure

Some basic properties of micro-actuators with different designs are shown in Table 4-2(a) and (b) with the external voltages at 100 and 200 volts, respectively. It should be noted from the table that the spring constants only depend on the ratio between the beam length and width, regardless of the actual sizes. In addition, while the maximum displacement increases as the applied power is increased, the natural frequency remains unchanged [78].

Table 4-2 Properties of the folded-beam flexure design

No.	g (μm)	w_b (μm)	h (μm)	l_b (μm)	Mass (mg)	N	K_x (N/m)	X_{max} (μm)
1	40	80	400	4000	4.873	216	28.16	3.394
2	20	40	400	1800	4.050	160	38.63	3.667
3	30	40	400	1800	5.290	104	38.63	1.588
4	40	80	400	4000	2.362	216	28.16	3.394

(a) V=100 volts

No.	g (μm)	w_b (μm)	h (μm)	l_b (μm)	Mass (mg)	N	K_x (N/m)	X_{max} (μm)
1	40	80	400	4000	4.873	216	28.16	13.577
2	20	40	400	1800	4.050	160	38.63	14.663
3	30	40	400	1800	5.290	104	38.63	6.354
4	40	80	400	4000	2.362	216	28.16	13.577

(b) V=200 volts

CHAPTER 5. MICRO-FIBRATION OF SU-8 BASED MICROSTRUCTURES

Traditional comb drives are made of silicon, which require complex fabrication process and high driving voltage [23,26]. In this dissertation, we report a lower cost, alternative approach to fabricate comb drive micro-actuator based on selectively metallized SU-8 polymer with high aspect ratio microstructure. The major advantages of this SU-8 based micro-actuator include: simple structure, excellent design flexibility, low fabrication cost, and no assembly requirement.

In this chapter, two different fabrication methods of SU-8 based comb drive microstructure are presented in details, respectively. The first method is to utilize modified SU-8 as the sacrificial layer to support the suspended parts and the second method is to use common Cu as the sacrificial layer. The advantages and the disadvantages of each method are discussed in the following sections.

5.1 Modified SU-8 as the Sacrificial Layer

It has been reported that UV absorption in SU-8 is proportional to the concentration of photoacidgenerator (PAG) [9,79]. The photoresist with higher PAG concentration shows increased sensitivity to radiation as well as higher absorption rate. Ling [79] reported experimental results of modified SU-8 that can realize different expose depths by mixing resin and regular SU-8 50. The key to the successful SU-8 modification is the appropriate ratio between the regular SU-8 and the resins, and the complete mixing of the two materials. In theory, we can use the regular SU-8 as the structural layer and the modified SU-8 as the

insensitive bottom layer to realize the micro-actuator without the sacrificial layer if the appropriate lithography parameters are applied.

To prepare the modified SU-8, a weight ratio of 1:25 between regular SU-8 50 (2.027 g) and SU-8 R 50 resin (49.994 g) was used. In order to produce uniform mixing solution, the mixtures were sealed in a bottle with a magnetic bar, which was immersed in a big beaker with lid containing hot water. The mixed solution was then agitated on a hotplate for at least 48 hours. The detailed lithography fabrication processes are described below and illustrated in flow chart Figure 5-1.

(1) The modified SU-8 photoresist was spin coated on a clean silicon wafer. To reach a uniform thickness of 50 μm, the spinning speed was set at 2000 rpm for 30 seconds. The soft-bake time was about 20 min at 96 ^{0}C.

(2) The supporting part of the micro-actuator was patterned using mask #1 under UV light source. The exposure dosage was increased significantly to 2000 mJ/cm^2 because of the low sensitivity of the modified SU-8. After 30 minutes relaxation time, post-baking process was done to induce cross-linking. Different from regular processes, the step of development was skipped.

(3) A thick regular SU-8 50 was spun on the exposed bottom layer with spinning speed of 400 rpm. As mentioned previously, it was necessary to place the wafer on a levered surface for a long period to create uniform SU-8 layer before soft-bake. After enough relaxation, soft-bake was performed on the wafer for 2 hours at 110 ^{0}C.

(4) The suspension part was patterned with mask #2. Different dosages were applied to different zones in one wafer to avoid overexposing the bottom layer. A 20 minutes post-bake process was also done after the exposure.

(5) Nano SU-8 Developer was applied to develop SU-8 structures for 1.5 hours. The wafer was then put into IPA and DI water for rinse.

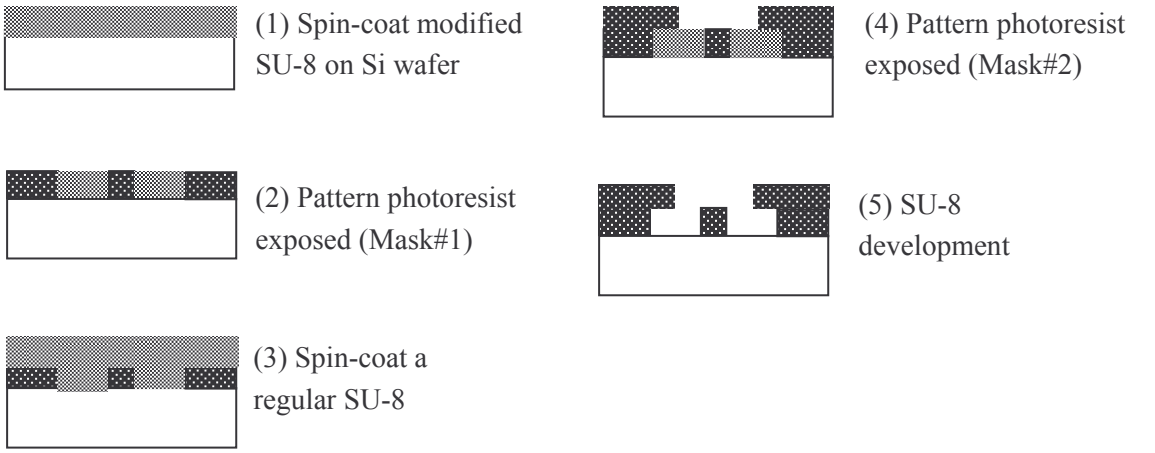

Figure 5-1 Fabrication sequence using regular and modified SU-8

However, in practice, the upper layer of SU-8 would diffuse into the bottom layer, especially during the bake process, which rendered the originally insensitive bottom layer sensitive, and resulted in the exposure of parts that were not designed to be exposed. In fact, after careful examination of the micro-structure (Figure 6(B) in Ref. [83]), a very thin diffusion layer between the upper and bottom layer was found. The aforementioned process provides many advantages such as easy handling, low cost, short operation time. For some applications, such diffusion can be tolerated for its benefits, especially for very thin upper layer structures or for the channel structures, where the upper layer is too thin to produce significant diffusion

between the upper layer and the bottom layer. But in our case (the upper layer is much thicker than the bottom layer), the drawback was significant: the two layers diffused together and the suspension part could not be obtained.

5.2 Cu as the Sacrificial layer

Evident from the previous section, although the modified SU-8 can be applied in many other scenarios, it is not suitable for our design. The other approach that utilizes Cu as the sacrificial layer based on traditional lithography process has to be used. Two optical masks were still used to fabricate the SU-8 based comb structure but the design was optimized. The first mask was used to produce the lower layer of the hinge posts and the plating pattern for Cu sacrificial layer. After the second layer of SU-8 was spin-coated and patterned, the copper sacrificial layer was removed to form the suspended comb drive fingers and to generate the support hinges with over-hang edges. The lithography process, which is schematically shown in Figure 5-2, has similar steps to the previous fabrication method.

(1) 10 nm Cr and 50 nm Au were coated on the surface of clean silicon substrate as the seed layer for electroplating.

(2) A 50 μm SU-8 film was spin-coated onto the wafer. The wafer was then pre-baked for 20 minutes.

(3) The SU-8 was patterned with a near-UV light source using the designed mask #1. The expose dosage and post-baking process are same as these in step 2 of the previous fabrication method. However, developing in Nano SU-8 Developer followed by rinsing in

IPA and DI water was necessary. After being blown dry with nitrogen gas, film residue removal from the substrate was then done with oxygen plasma asher.

(4) The copper sacrificial layer was electrodeposited. The electroplating process took almost 4 hours while applied current was adjusted to 0.13 A. The overplating part was then manually and mechanically leveled to the height of the photoresist, followed by a DI water rinse and N_2 blow-dry.

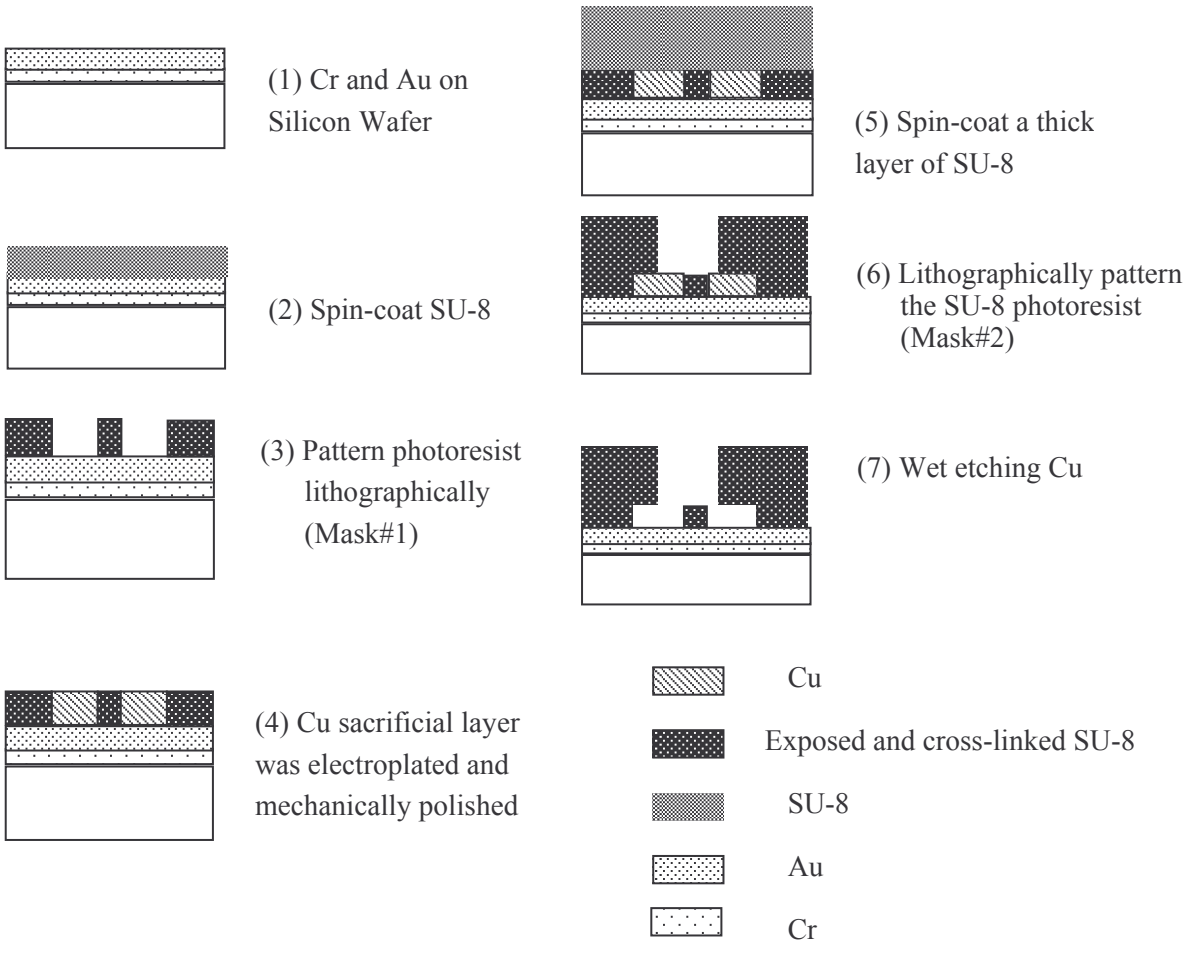

Figure 5-2 Fabrication sequence using regular lithography process

(5) A 400 μm structural layer of SU-8 photoresist was spin-coated onto the sacrificial layer and pre-baked for 2 hours at 110 ^{0}C after enough relaxation time.

(6) The SU-8 resist was lithographically patterned with a near-UV light source utilizing the UV-mask #2. Same as above, the regular post-baking was performed. Special attention was paid to the developing step in Nano SU-8 Developer. Due to the thick layer and narrow structure, developing was performed in the megasonic environment.

(7) Suspension release was achieved by wet etching of the copper sacrificial layer.

CHAPTER 6. SELECTIVE METALLIZATION OF CURED SU-8 MICROSTRUCTURES

6.1 Metallization of SU-8 Polymer

In the last chapter, the prototype of micro-actuator was fabricated using multi-layer and multi-step UV lithography technique. The functionality of the microa-ctuator requires electrical signals be transmitted through the electrically non-conductive SU-8 microstructures. It is therefore essential to develop a technology for selective metallization of cured SU-8 polymer microstructures.

One of commonly utilized methods to achieve electrical conductivity in cured SU-8 is to add metal (i.e. silver) nanoparticles to the SU-8 monomer [80]. Because silver particles are not transparent to the UV light, the lithography resolution of the resist is significantly reduced. Typical resolution is about 35 microns following standard processing steps. With more complex procedures, resolution of 5 microns may be achieved, but only for relatively thin films (less then 10 microns). Another way to make SU-8 electrically conductive is to use conductive polymers, i.e. polyaniline [81].

Instead of creating homogenous conductive SU-8 polymer, polymer metallization can also be realized through E-beam deposition (sputter) and electroless plating. Zhao [25] used sputtering technology to obtain Ti/Au films in fabricating a PMMA-based electrostatic comb drives. Eberhardt [26] proposed a method in which LCP (liquid crystal polymer) micromechanical devices were covered with metal layers such as copper or gold using electroless plating. However, their devices required manual assembling and adjustment under

microscope after the polymer parts were metallized; otherwise the entire polymer and even non-polymer material could also be metallized, resulting in short circuits and other problems. G. A. Shafeev et al. [82] used electroless plating combined with visible continuous-wave and pulsed lasers techniques to produce metal films on insulator surfaces such as SiO_2, glass and polyphenylquinoxaline by electroless growing on a thermally activated palladium acetylacetonate ($Pd(acac)_2$) seeding layer. Hrapovic [83] described a simple electroless procedure for deposition of gold from solution onto glass surfaces precoated with a thin layer of poly (diallyldimethylam-monium chloride), PDDA. Henry [84] reported the use of amine-terminated poly (methyl methacrylate), AT-PMMA, surface as the substrate for the electroless deposition of Au nanoparticle films (Au-EDNPFs). Through the adsorptive deposition of Au colloids, the laterally patterned formation of Au-EDNPFs, and the use of the patterned Au-EDNPFs, he was able to form electrolessly deposited Ag films with micrometer features. In this chapter, improved E-beam deposition method and selective electroless plating method were used to metallize the SU-8 based microstructures to realize the micro-actuators. The detailed procedures are presented in the following sections.

6.2 Tilted E-beam Evaporation

After the comb drive structures were produced, metal film should be coated to form two electrically separated electrodes. With the uniquely designed support hinges with over-hang edges, only a single evaporation process was required to coat metal film on these electrodes and connectors without causing interconnections and short circuits. E-beam deposition, one of the

most convenient methods, was applied to SU-8 based microstructure to ensure the structure conductivity by coating gold. Usually, E-beam particles hit the target perpendicularly. It is difficult for the metal atoms to be attached to the bottom parts of the side wall of the comb drive because of its very high respect ratio. Therefore the e-beam evaporation was performed by rotating by certain angle continuously to metallize the sidewall. To metallize the bottom of the side wall, the maximum inclined angle α must satisfy the following relationship:

$$\alpha \le ac\tan\frac{g}{h} \tag{6.1}$$

In our design, g is 20 μm and h is 400 μm, and α was calculated as $\alpha \le 2.86^0$. Such a small incline angle was proven feasible.

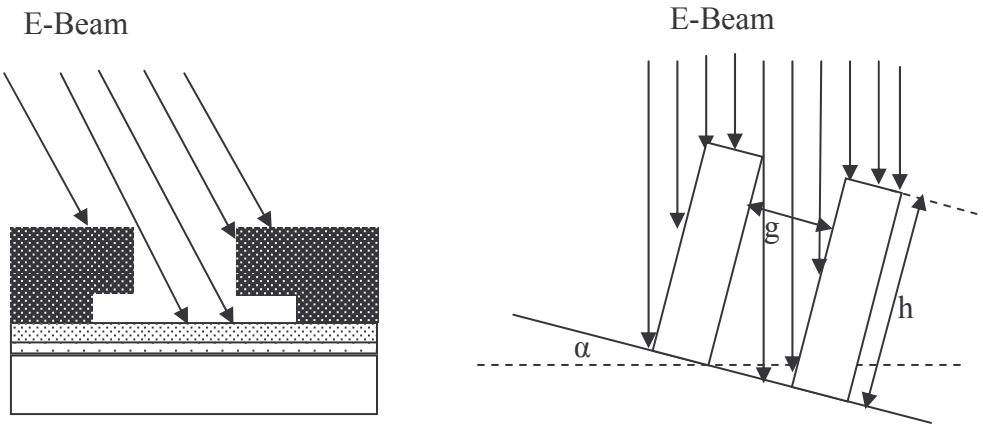

(A) (B)

Figure 6-1 Coating metal film on side walls of the comb drive

Figure 6-1 schematically illustrates the principle of the metal coating process using this evaporation method. Figure 6-1 (A) shows that the over-hang edge in hinge post prevented metal from being deposited on the bottom part of the post, which can cause short circuit. Figure 6-1 (B) shows the relationship between the tiled angle, the height, and the gap between the

fingers of the comb drive during the evaporation process. The tilted E-beam deposition combined with design of over-hang geometry requires that:

(A) The cantilevered structure of the supporting posts to avoid metal deposition on the bottom parts and electrical connection between the stationary and moving parts.

(B) The height and gap of the comb drive should be carefully designed for full metal deposition on sidewalls.

In usual E-beam evaporation, the main difficulty was to obtain the uniform coating of sidewalls of microstructures, because of the very narrow gaps between the micro-features and the unavoidable nature of the line of sight. Although the tilted E-beam deposition is capable of realizing such uniform coating, the over-hang geometry design was necessary to avoid short circuit. The over-hang geometry however presents a significant drawback in that the two layers in the previous fabrication process should both be SU-8 structures, which may result in insufficient adhesion between the two layers. To obtain the one-step SU-8 structure and keep the silicon wafer insulated, other technique is necessary.

6.3 Selective Electroless Plating Method

A new approach to selectively electroless plate metal on high aspect ratio cured SU-8 polymer microstructures is reported in this section. In this approach, UV light source was used to activate the cured SU-8 surface. Selective electroless plating of metals on cured SU-8 was achieved by controlling the UV exposure dosage and radiation direction. This technique offers the possibility of metallizing microstructures selectively with no assembly requirement, which

could be important in realizing the low cost fabrications of integrated polymer based micro-transducer.

6.3.1 Sample Preparation

To quantitatively characterize the selective electroless plating of metals on cured SU-8 polymer, microstructures made of SU-8 resist with honey cell patterns were fabricated as samples using UV lithography. Such structures have the advantage of multiple sidewalls and chambers, which makes it easier to test the metallized surfaces in later stage. For the comparison purpose, efforts were made to maintain the same processing conditions for all of the samples. The detailed procedure for the sample fabrication is presented as follows: SU-8 50 was spin-coated on a clean silicon substrate at the speed of 400 rpm to obtain a film of 400 μm. After four hours relaxation to release residual stress, a softbake was conducted at the temperature of 110 °C for 2 hours. A near-UV lithography was then made using the optical mask with honey cell pattern, followed by post-baking step to induce cross-linking. Finally, the unexposed SU-8 was developed in Nano SU-8 Developer (MicroChem Corp., Newton, MA), rinsed in Isopropanol (IPA) and deionized (DI) water, and blown dry with nitrogen gas. Film residue was removed from the substrate using oxygen plasma asher. The honey cell microstructures had wall height of 400 μm, length of 650 μm, and thickness of 70 μm.

6.3.2 Surface Modification

Henry, et al. [84] demonstrated that the surface of commercially available PMMA can be modified through UV light exposure, whose mechanism can be linked to the amine group. This

amine group can be easily attached to metal nanoparticles that serve as a good base for depositing thick metal films. From the perspective of molecular structure, SU-8 has even more active molecular structure than PMMA. Henceforth, it should be possible to modify SU-8 using UV radiation, and then coat metal films on it using electroless deposition. In this work, the samples (patterned honey cell SU-8 microstructures on silicon wafers) were prepared under the above mentioned conditions. A deep UV lamp (USHIO lamp, UXM-501MA, ABM, Inc) with a wavelength of 254 nm was used to expose the samples under various conditions of exposure durations and exposure directions. The intensity of the UV light source was maintained at the same level of 15 mW/cm^2.

In the first set of experiments, samples were perpendicularly exposed and only exposure dosages were varied. The samples were tested in four different dosages, with exposure duration set at 5, 10, 20, and 40 minutes, which are equivalent to dosages of 4500, 9000, 18000, and 36000 mJ/cm^2, respectively.

In the second set of experiments, six groups of samples were tilt-exposed for 5, 10, 20, 40, 60 (54000 mJ/cm^2), and 120 minutes (108000mJ/cm^2), respectively. All other processing conditions were maintained the same as in the previous experiments. The purpose of tilted exposure was to obtain electroless plating on the sidewalls of the microstructures.

After the UV exposure, the samples were immersed in compound solution of 750 mg *N*-(3-Dimethylaminopropy-*N′*-ethylcarbodiimide Hydrochloride ($C_8H_{17}N_3 \cdot HCl$, simplified as EDC), 75 ml phosphate buffer, and 900 μL ethylenediamine ($C_2H_8N_2$, simplified as EDA). The

solution was covered and continuously stirred for 16 hours to guarantee the uniform mixture of the compound with the samples.

6.3.3 Electroless Plating Au and Cu

Electroless plating of Au was conducted at the room temperature. The samples were first placed in a solution of 29.4 mg hydrogen tetrachloroaurate (III) hydrate ($HAuCl_4$) and 75 ml DI water, covered with alumina foil to avoid ambient light radiation. After three hours stirring in the solution, the samples were taken out and submerged into a solution of 570 mg sodium borohydride ($NaBH_4$) and 75 ml DI water for an hour, which completed electroless plating of Au on cured SU-8. The next step was to electrolessly plate Cu on Au covered SU-8 surface. A conventional electroless copper bath was used. The recipe was: 24.79 ml formaldehyde (HCHO), 2.18 g copper sulphate ($CuSO_4$), 28.223 g sodium potassium tartarate ($KNaC_4H_4O_6 \cdot 4H_2O$), and 1000 ml DI water. Potassium hydroxide (KOH) was also added to the solution to adjust the PH value to 11. The bath was then heated to 45 ^{0}C and the samples were kept in it for 30 minutes to obtain Cu film of 1-2 μm thickness. It was observed that the immersion time and the plating temperature significantly affected the plating speed and the coated metal thickness.

6.3.4 Experimental Analysis and Discussion

Table 6-1 shows the relationship between the exposure time (total dosages) and the selective electroless plating results on the surfaces of both cured SU-8 polymer and silicon substrate. The experimental results demonstrated that selective Cu and Au coating on the surfaces of the cured SU-8 structures and the silicon substrates can be realized, but only with

careful controlled UV exposure dosages. The exposure dosage proved to be the dominant factor in achieving successful electroless coating. As shown in Table 6-1, when the exposure dosage was less than 9000 mJ/cm^2, silicon surface was coated with copper but cured SU-8 microstructures were not. When the radiation dosage exceeded 9000 mJ/cm^2, metal depositions were observed on surfaces of both silicon substrate and SU-8 microstructures. As the exposure dosage increased to more than 18000 mJ/cm^2, metal plating was realized only on the surfaces of cured SU-8 microstructures but not on the silicon substrate. The experimental results were found highly repeatable. Additionally, another interesting phenomenon was also observed: the sidewalls of SU-8 microstructures could not be electrolessly plated even when the dosage was increased to 36000 mJ/cm^2. The possible reason could be that the much lower effective exposure dosages received by the vertical sidewalls due to the perpendicular application of UV light source.

Figure 6-2 shows a SEM image of the prototype honey cell structure with metal successfully deposited on the top surfaces, but no observable metal plating on the sidewalls. The SEM image in Figure 6-3 shows metal deposits on top surfaces of SU-8 microstructures. Evident from the SEM image, the metal particles were quite uniformly distributed and their sizes were estimated to be in submicron range. EDAX EDS analysis (Hitachi S-3600N variable pressure SEM and EDAX EDS system, Hitachi High Technologies America, Inc.) results are shown in Figure 6-4, in which the horizontal axis is electronic energy and the vertical axis is intensity. For the same element, the energy peaks always appear at the same location along the

horizontal axis, although the vertical axis shows different intensity values under different experimental conditions. In Figure 6-4, the matched peaks indicate the presence of copper. Carbon and oxygen also shown in the figure were from cured SU-8 microstructures, while silicon was the consequence of contaminations in wafer cutting during sample preparation.

Table 6-1 The relationship between exposure dosage and material deposited

Exposure dosage (mJ/cm^2)	4500	9000	18000	36000
Silicon	Metal plating	Metal plating	No metal plating	No metal plating
Cured SU-8	No metal plating	Metal plating	Metal plating	Metal plating with lower quality

In order to electrolessly plate metal film on the sidewalls of cured SU-8 microstructures, tilted UV exposures were utilized. In our case, the thickness of honey cell wall was 400 μm and the gap between two walls was around 1000 μm. Therefore, the tilt angle should be below 68^0 (=arctan(2.5)). To ensure the exposure at the bottom of sidewalls, the tilt angle was selected as 45^0. It was observed from experiments that higher dosages were needed in such tilted exposures than in normal exposure. The optimal exposure dosage was selected as 36000 mJ/cm^2, under which the sidewalls of cured SU-8 microstructures were coated while no metal coating was observed on silicon substrate. To visually confirm the metal coating on the sidewalls of the microstructures, the samples were mechanically cut into half, and the sidewalls of cured SU-8 were observed using scanning electronic microscope. Figure 6-5 shows the upside-down view SEM image of a sample, and Figure 6-6 is a zoom-in SEM image showing the magnified surface topography of the sidewall. The EDAX EDS analysis results shown in Figure 6-7

indicate that the coated metal was indeed copper. The results also proved that there was no significant difference between the copper deposited on the top and sidewall surfaces.

The experimental results presented above demonstrated the feasibility of the approach taken in this research, i.e., electroless plating of copper on cured SU-8 polymer can be achieved after appropriate surface modification. To explain the underlying mechanism for such process, one needs to delve into the underlying chemical principles.

As well known, uncured SU-8 resin has eight epoxy functional groups, each of which forms a ring. After UV exposure and post-bake, these rings are opened and SU-8 resin is cross-linked to form polymer structure from monomers. Epoxy resins are normally based on phenol or aromatic groups. They are not stable under ultra violet exposure due to their unsaturated molecular structures. In other words, UV light exposure could re-arrange epoxy structures (e.g. from unsaturated structure to saturated structure). For instance, UV light may break the double bonds to single ones, or change the net-structures of the resin polymers. Some bonds between carbon and oxygen in the cross-linked structure of SU-8 could also break down under large dose of UV illumination. The broken bonds between carbon and oxygen in SU-8 polymer may also allow the opportunity of the carbons linking to amine group under the influence of certain chemicals. EDA was used as a solvent for the Au in our study. It is a powerful curing agent for the epoxy resin and can react with epoxy groups to form OH^- group, which provides excellent adhesion to metals. This leads to Au colloidal film attached to the surface of polymer structure that serves as the seed layer for electroless plating copper film.

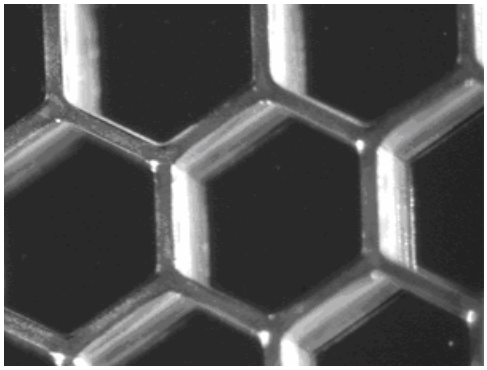

Figure 6-2 Metal deposited on top surface of cured SU-8 microstructures

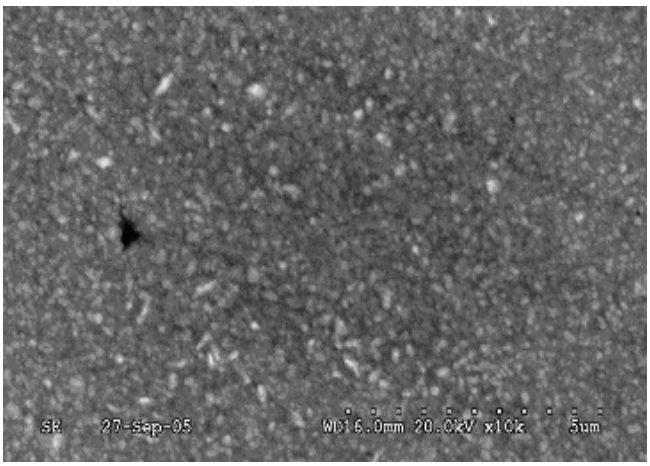

Figure 6-3 A zoom-in SEM image showing metal particles on the surface of cured SU-8 microstructures

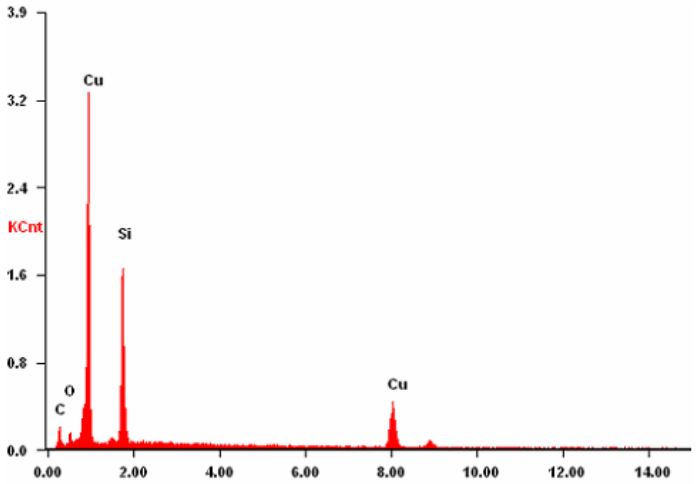

Figure 6-4 EDS spectrum of cured SU-8 surface after electroless plating by copper

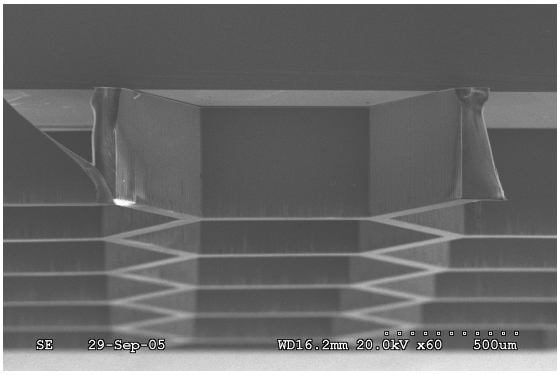

Figure 6-5 Side view SEM image of the cured SU-8 microstructures, inversely oriented

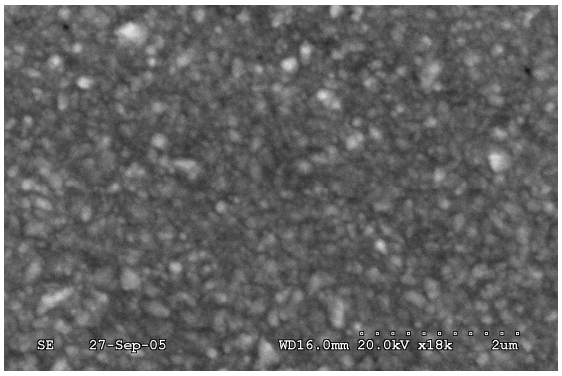

Figure 6-6 SEM image showing metal film on the sidewalls of cured SU-8 microstructures

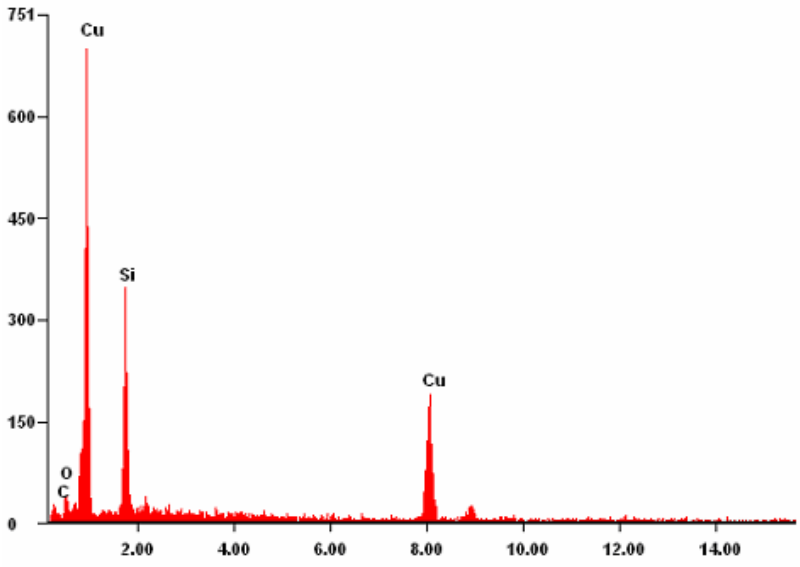

Figure 6-7 EDS spectrum of the sidewall surfaces of cured SU-8 microstructures with electroless plated thin film

Many researches have also pointed out the excellent affinity of amines for certain metal ions or metal colloids [84,85,86]. Particularly, the bonds between amine and Au colloid are very strong [87]. $HAuCl_4$ is often regarded as an oxidant in chemistry that can be reduced to Au colloid by reacting with $NaBH_4$. It is therefore reasonable to deduce that the UV modified SU-8 surface connected with amine group helps to attach Au colloids after being immersed in solution of $HAuCl_4$ and $NaBH_4$. The Au film then forms the plating base for copper plating.

On the other hand, when the exposure exceeds certain level (more than 54000 mJ/cm^2), the electroless plating quality actually dropped significantly. This may also be explained based on the effect of UV exposure on epoxy resins. It is well known that excessive UV exposure may cause performance and properties deterioration of epoxy resins. The longer the exposure to UV, the worse properties the epoxy resin may have. It is therefore important to avoid epoxy resin exposure under UV light in industrial applications. UV stabilizers sometimes are added into the epoxy system before the application process in some industrial uses. Because the stabilizers can absorb UV, damage on epoxy resins caused by UV can be greatly reduced.

When excessive UV exposure dosage is used, surface damage might become severe. This was proved by the observation of some powder-like materials on the surface of the cured SU-8 in our experiments. The powders on the surface have seriously reduced the adhesion of Au colloidal film on the polymer surface and resulted in dramatically lower adhesion between metal film and SU-8 polymer. Several experiments were done to analyze the films plated on the cured SU-8 microstructures. Figure 6-8 shows an SEM image of the modified SU-8 surface

after being immersed in $NaBH_4$ solution. Large amount of particles were distributed on the surface. Some particles are very small while some others are much larger, indicating that these particles either exist in the form of nanoparticles, or accumulate into colloids with larger sizes. EDAX EDS analysis confirmed that these particles are Au element as shown in Figure 6-9. Figure 6-10 shows AFM results for a typical sample. These results confirmed that the typical sizes of Au nanoparticles are in the range of several hundred nanometers, and the heights are less than ten nanometers.

The successfully obtained Au colloidal film serves as an excellent base for electroless plating of copper. The solution composition and plating conditions followed common practices in our case. Potassium sodium tartarate was used as the complexing agent and formaldehyde was used as the reducing agent. According to the mixed-potential theory, the overall reaction can be expressed as a simple reduction -- the cathodic partial reaction:

$$Cu^{2+} + 2e \rightarrow Cu \tag{6.2}$$

and the oxidation reaction -- the anodic partial reaction

$$HCHO + 2OH^- \rightarrow HCOO^- + H_2O + \frac{1}{2}H_2 + e \tag{6.3}$$

It should be noted that the reaction environment must be alkaline. Therefore, an appropriate pH value is vital to the success of electroless copper plating.

There are very few research efforts reported in open literature on electroless plating metals on silicon substrate. Xu et al. [88] reported a work on selective electroless plating of copper on (100)-oriented single crystal silicon surface. They treated silicon with HF solution, which

produced the hydrogen-terminated silicon surfaces. It was then activated with UV-induced reactive coupling of 4-vinylpyridine (4VP). High quality film of copper could then be produced using electroless plating.

This research work targets selective electroless plating of metal films on only the cured SU-8 structures, but not the silicon substrate. However, our experiments revealed that the electroless plating of metals on the silicon surface could not be avoided without proper surface treatment. Fortunately, the experiments also revealed that large dosage of UV light exposure could help preventing electroless plating on silicon surface. A large dosage of UV exposure generated a layer of oxidation film on the surface of silicon substrate. The layer of oxidized silicon is much less electrical conductive and thus prevents electroless plating of metals.

Electroless plating in general produces very good surface uniformity. Because the sidewalls are exposed in a given tilt angle, their surface property should be also uniform as long as the light exposure is uniform on the sidewalls. The surface uniformity should therefore only be affected by the diffusion of Cu ions into the honeycomb cells. The film thickness may decrease when closer to the bottom of very deep and narrow gaps. Some types of agitations and stirring mechanisms are therefore necessary in such cases. However, for the honey cell structures in this work, the surface uniformity (with the thickness of the film around 1 μm) seemed very good. In particular, for the applications of this approach in this thesis to fabricate polymer based micro-transducer, only thin films of metals are required. The uniformity in general should not be a problem [89].

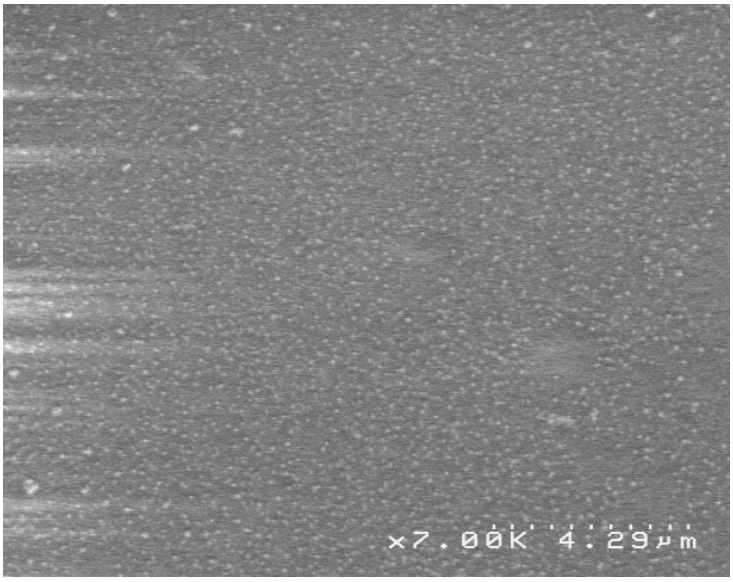

Figure 6-8 SEM image of modified SU-8 surface before electroless copper plating. Gold nanoparticles were observed on the surface

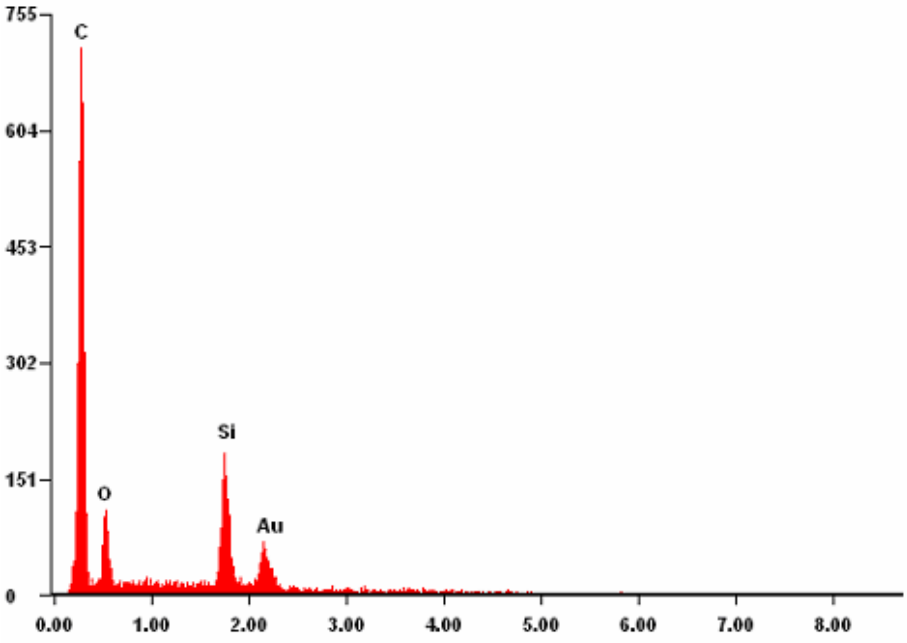

Figure 6-9 EDS spectrum of the modified SU-8 surface before electroless copper plating. The measurement verified the existence of gold

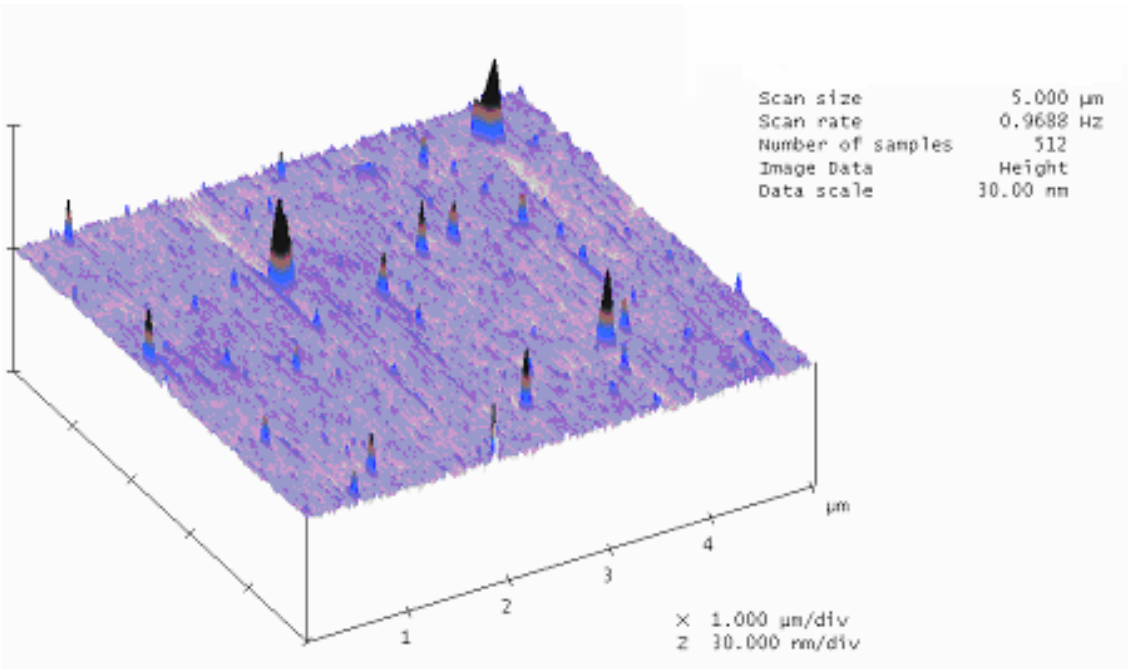

(A)

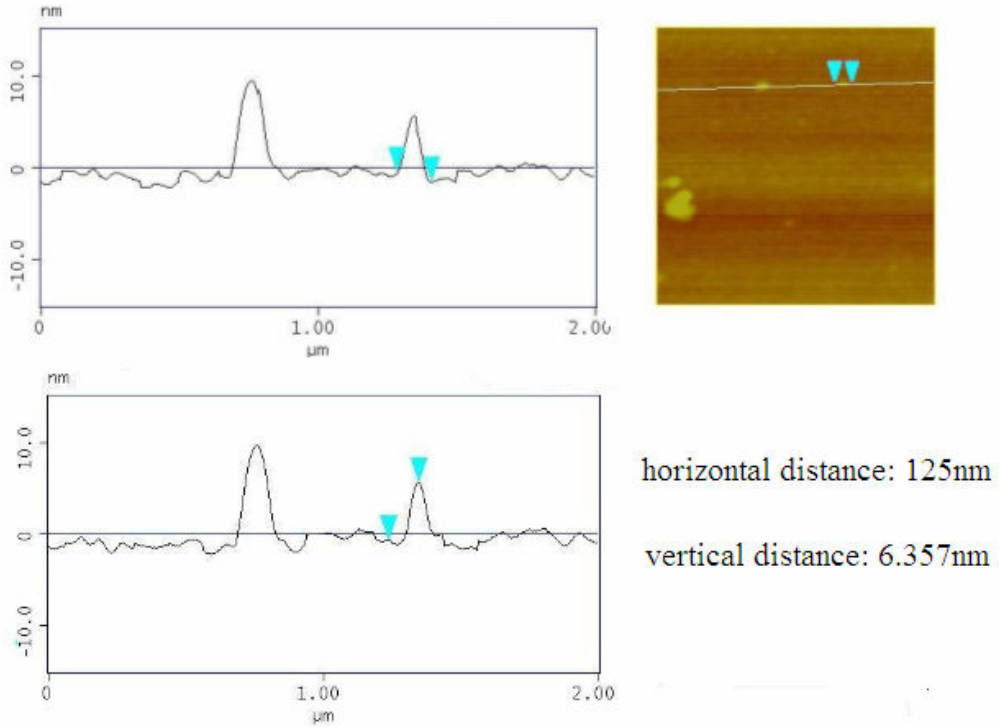

(B)

Figure 6-10 AFM results of Au particle on SU-8 surface (A) The overview (B) The size and height of an Au particle

CHAPTER 7. MICRO-ACTUATOR FABRICATION EXPERIMENTS AND RESULTS DISCUSSION

In previous chapters, the methods and approaches for design and fabrication of micro-actuators based on SU-8 polymer as main structural material were developed. The adhesion properties between metals and SU-8 polymer surfaces were characterized. The established knowledgebase provided the guideline for choosing the optimal metal materials with high adhesion strength to SU-8 as the seed layer or sacrificial layer, which served as the basis for realizing the micro-structure through multi-layer, multi-step UV-lithography technique. To guarantee the sufficient structural integrity, the methodology for measuring micro-fracture toughness of materials used for fabricating micro-structures was established. The method was successfully implemented to measure the fracture toughness of micro electroplating nickel.

With the material properties characterized, the structure of the comb-drive micro-actuator was designed with the help of mechanical structural analysis. The techniques for fabricating the specific micro-structures were developed with two multi-layer, multi-step UV-lithography methods, described in chapter 5.

The most difficult problem of realizing the electrical conduction for the side wall of the comb drive prototype was tackled in chapter 6. Two approaches were studies in details, the titled E-beam deposition technique and the selectively electroless plating technique. The electroless plating technique was shown to be more suitable as it requires no special over-hang geometry design and thus dramatically simplified the fabrication process.

As the nature of any fabrication process research activity, the success can only be the results of many prior failure, from which lessons are learned and fabrication procedures were perfected. In this chapter, the prior unsuccessful results are first shown, and the root causes are explained. The final fine tuned fabrication procedures are then re-iterated, summarizing steps scattering in previous chapters. Some of steps and parameters are improvements over the previously described. Finally, the successfully fabricated functional micro-actuators are shown, and test results are given to demonstrate its deformation/actuation responses under the applied electrical signals.

7.1 Suspended Micro-structures

Two fabrication approaches were evaluated for fabricating the SU-8 micro-structure in Chapter 5: (1) multilayer processing using modified SU-8 with reduced PAG (photoacidgenerator) as sacrificial layer; (2) multilayer processing using normal SU-8 with copper as sacrificial layer. Figure 7-1 shows SEM picture of microstructure using the modified SU-8 method. In this picture, it is clear that the design intended suspension spring has already reached the wafer surface, which means that the suspended parts were not obtained. The main cause was that the thick upper layer diffused into the thin bottom layer, which rendered the bottom layer sensitive to UV source, hence, indicating that this fabrication method was not suitable for our design.

The other fabrication method used copper as sacrificial layer, as presented in the section 5.2. This method is based on the over-hang geometry design and needs to be combined with

tilted E-beam deposition technology to realize the comb drive micro-transducer using SU-8 as the main structural material. The purpose of using tilted angle in E-beam evaporation was to coat metal film on electrodes and connectors while avoiding the undesirable wafer surface part coating and short circuits. Figure 7-2 shows several successful SEM images of a prototype comb drive with gap of 20 μm and height of 400 μm after gold film evaporation using regular lithography process with Cu as the sacrificial layer. Figure 7-2 (A) shows the released comb drive structure, (B) shows the suspended comb drive part connected with spring, and (C) shows the larger suspended spring structure. It is evident that there are slits between microstructure and silicon surface, confirming part of the comb drive and the spring are indeed suspended.

7.2 Fabrication Process Optimization

Once the suspended micro-structures were fabricated, the micro-actuator was ready for characterization. As an initial check, the suspended comb drive part and spring structure were pushed by a very small force with great care. The comb-drive left the original position and started very small vibration. When the force was removed, the structure went back to the original position. The observation proved that the comb drive part and spring were in fact suspended and were able to deform elastically. Then, the response of the micro-actuator was measured while the device was plugged into an external voltage. Thin copper wires were bonded on the bonding pads using conductive epoxy. In the first stage, a DC voltage was applied to the connectors with the bonding copper. However, displacement was not observed under the microscope even when the applied voltage reached 200V.

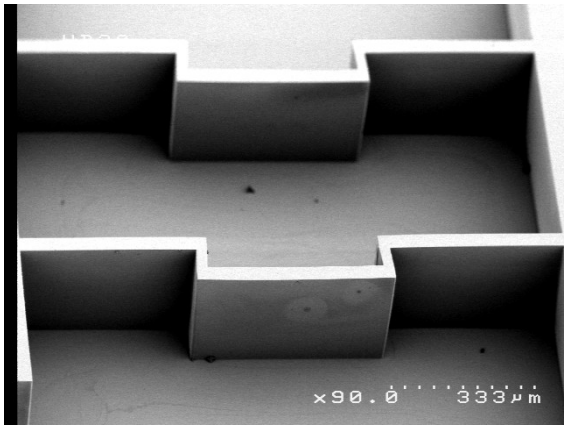

Figure 7-1 Unsuccessful examples using modified SU-8 method

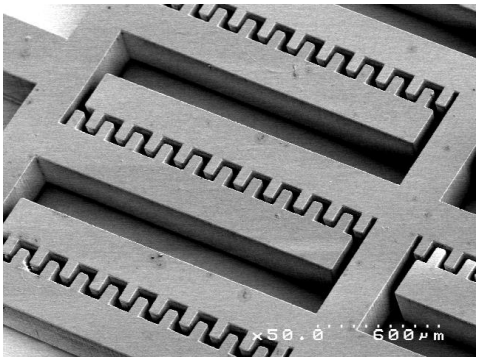

(A)

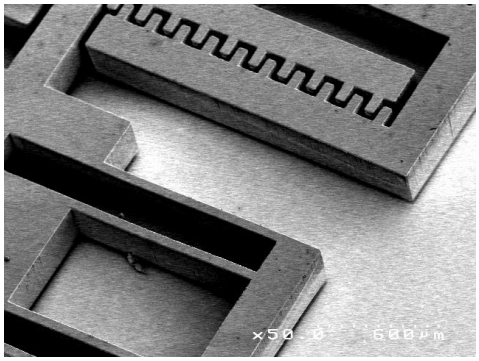

(B)

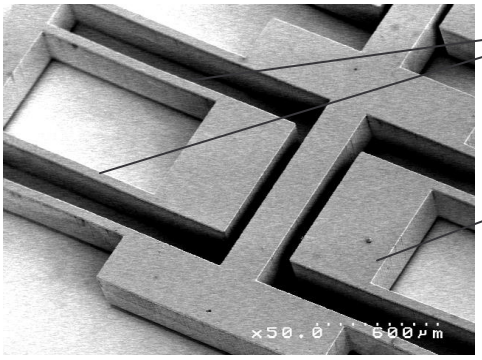

Suspension springs released from substrate

Hinge with over-hang edge (air gap in area)

(C)

Figure 7-2 SEM pictures of successful comb-drive after metallization

The root cause of the stagnation of the micro-structure under electrical signals was investigated. Several hypotheses were postulated as the explanation. A) The comb drive side wall surfaces might not be smooth enough because of incomplete development in some areas. B) The metal coating might not be thick enough. C) The metal film might have not been deposited on the bottom of the side wall, which means the microstructure was insulated. D) The tilt angle in the tilted E-beam evaporation process was hard to control, which might have caused unnecessary part in the silicon wafer becoming conductive, resulting in short circuit.

Several solutions to overcome the problems were adapted according to the above analysis.

Careful control of development procedure. The last development step of UV lithography process in SU-8 based microstructure fabrication was more precisely controlled. The exposed SU-8 microstructure was put in the mega-sonic environment and the developer was refreshed once or twice. At the end, the wafer was placed face down in the developer for an extended period so that the unexposed part in the narrow area dropped off by gravitation force.

It was also observed that too short development time will result in incomplete development, while too long development time will cause the SU-8 microstructure swollen, even unable to separate the comb drive structure. Therefore, the entire development time were carefully chosen by trial-and-error, and precisely imposed.

Deposition of multiple metallic layers on SU-8 structure. In the original design, a thin gold film with the thickness of 50 nm was deposited with tilted angle to SU-8 based microstructures. Due to the tilted deposited process, the bottom corner area had only an

extreme thin gold coating or even was not deposited at all. If this happens, the open circuit is resulted, leading to the stagnation of micro-structure under external DC. To enhance the reliability of the deposition process, multiple Au-depositions were conducted in sequence. In the mean time, thicker Au film coating for each layer was necessary, but at higher cost.

Adaptation of selectively electroless plating method. In order to avoid controlling the tilted angle in the E-beam evaporation process, another metallization technique — selectively electroless plating method was instead used, as described in chapter 6. Some of the results of high quality metal film being selectively coated on the surfaces of cured SU-8 microstructures with electroless plating method were already presented in chapter 6. This method was proven to be an ideal choice to realize our micro-transducer. The major advantage is that it is capable of metallizing the specific part of SU-8 structure, but not the silicon wafer. To achieve the selectiveness, extensive tests were done to determine the proper UV exposure dosage, duration, and other operational procedure parameters. Under optimal process condition, the method has been found to be every reliable and produce very high quality. Also benefiting from adapting the selective electroless plating method, the SU-8 microstructure fabrication process could be simplified since the over-hang geometry design could be replaced by easier and more common designs. The new design also has longer comb drive fingers, which would help increasing the linear response range between displacements and applied voltages.

The underlying mechanism of the electroless metal plating on UV modified SU-8 polymer could be explained from the polymer molecular structures of cured SU-8 and the effects of UV

exposure on the chemical bonds. Because epoxy resins (such as SU-8) are based on phenol, or aromatic groups, they are not stable under ultra violet exposure due to its unsaturated aromatic structures. UV light exposure could re-arrange epoxy structures (e.g. from unsaturated structure to saturated structure) and may break the double bonds to single ones, or change the net-structures of the resin polymers. Some bonds between carbon and oxygen in the cross-linked structure of SU-8 could also break under large dose of UV illumination. Some bonds between carbon and oxygen in the cross-linked structure of SU-8 could also break under large dose of UV illumination. EDA is a powerful curing agent for the epoxy resin and can react with epoxy groups to form OH^- and amine groups that provide the excellent adhesion to metals. This leads to Au colloidal film attached to the surface of polymer structure that serves as the seed layer for electroless plating copper film. Our research also found that excessive exposure dosage could cause significant surface damages on cured SU-8, a well known phenomenon in polymer industry, and therefore reduce the adhesion of metals on SU-8 surface.

7.3 The Optimized Fabrication Procedure

The unsuccessful trials of micro-actuator fabrication revealed necessary changes in the fabrication procedure over the procedure formulated when each individual technique was developed in the previous chapters. The final optimized fabrication procedure and parameters are summarized below in eleven steps. The use of AZ photoresist shortened the time required for the whole process, and one-step SU-8 operation was realized. It should be noted that the new comb drive design was a little different from the old over-hang design.

(1) 10 nm Cr and 50 nm Au were coated on the surface of clean silicon substrate as the seed layer for electroplating.

(2) About 5 ml AZ 4620 was spin-coated onto the wafer at the spinning speed of 2000 rpm for 5 seconds. The target thickness is around 20 μm. After 30 minutes relaxation, the wafer was put in the oven at the temperature of 95 ^{0}C for 10 minutes and then put on the hotplate at the temperature of 115 ^{0}C for one minute. After that, 400 mJ/cm^2 UV exposure was made using mask #1. The mixture of AZ 400K and DI water (1:4) as developer was used to develop the exposed pattern. The development time was about 5 minutes.

(3) Before the copper sacrificial layer was electrodeposited, the wafer was put in the plasma ash machine to improve the adhesion between the copper and gold seed layer. The electroplating process took almost 3 hours while applied current was adjusted to 0.13 A. The overplating part was then manually and mechanically leveled to the height of the photoresist, followed by a DI water rinse and N_2 blow-dry.

(4) A 400 μm structural layer of SU-8 photoresist was spin-coated onto the sacrificial layer. The thickness control is emphasized as follows: Before spin coating SU-8, the net wafer weight was measured by the scale. Then about 9 g SU-8 was put on the center of the wafer and spun at the speed of 400 rpm for 30 s (SU-8 is difficult to spread if it is less than 8 g). After that, we found the net SU-8 was around 5 g. The pre-bake process was put on the leveled hotplate for 2 hours at 110 ^{0}C after enough relaxation time. To reduce the internal stress, the cooling process was realized by ramping to 75 ^{0}C in 40 minutes, ramping to 55

^{0}C in another 40 minutes, then dwelling for 4 hours at 55 ^{0}C, and finally ramping to 25 ^{0}C within 3 hours. The SU-8 resist was then lithographically patterned with a near-UV light source utilizing the UV-mask #2 and followed by the regular post-baking. Special attention was paid to the developing step in Nano SU-8 Developer. Due to the thick layer and narrow structure, developing performed in the megasonic environment is recommended. For about 400 μm high structure, the ideal development time is about 65-90 minutes. Due to careful process control, the profiler measurement showed the thickness of the comb drive microstructure was 402-404 μm.

(6) Suspension release was achieved by wet etching of the copper sacrificial layer. The sample was put into the diluted nitric acid (30% weight) for 30 minutes and then rinsed in DI water.

(7) Seed layer was etched by the gold etchant for 15 seconds till the silicon was exposed. The exposure was checked.

(8) The surface of cured SU-8 polymer needed to be pretreated using UV light exposure with carefully controlled dosage and radiation direction using shadow masks. The wavelength of UV light was 254 nm and the UV intensity was 15 mW/cm^2. The optimal exposure dosages were around 18,000 mJ/cm^2 for perpendicular radiation. For electroless plating on sidewalls of the microstructures, a tilted exposure was utilized. In general, the required exposure dosages should be calculated based on the normal projection on the sidewalls for the specific tilt angle. A dosage of 360,000 mJ/cm^2 was used to modify the sidewall surface with small tilted angles in our cases.

(9) The samples were immersed in a compound solution of 750 mg *N*-3-Dimethylaminopropy-*N′*-ethylcarbodiimide Hydrochloride ($C_8H_{17}N_3$·HCl, simplified as EDC), 75 ml phosphate buffer, and 900 μL ethylenediamine ($C_2H_8N_2$, simplified as EDA) for 12 hours.

(10) Electroless plating of Au was conducted at the room temperature. The samples were firstly placed in the solution of 29.4 mg hydrogen tetrachloroaurate (III) hydrate ($HAuCl_4$) and 75 ml DI water, covered with alumina foil to avoid ambient light radiation. After three hours stirring in the solution, the samples were taken out and submerged into the solution of 570 mg sodium borohydride ($NaBH_4$) and 75 ml DI water for an hour.

(11) Electrolessly plate Cu on Au covered SU-8 surface. The solution was made of 24.79 ml formaldehyde (HCHO), 2.18 g copper sulphate ($CuSO_4$), 28.223 g sodium potassium tartarate ($KNaC_4H_4O_6$ •$4H_2O$), and 1000 ml DI water. Potassium hydroxide (KOH) was also added to the solution to adjust the pH value to 11. The bath was then heated to 45 ^{0}C and the samples were kept in it for 30 minutes to obtain Cu film of 1-2 μm thickness.

After following the procedure stated above, SU-8 based micro-actuators were successfully produced. Figure 7-3 shows the pictures of the comb drive microstructures under the optical microscope after the developing step and before etching the sacrificial layer (after step 6 but before step 7). In the figure, (B) is a zoom-in picture for (A), and (C) is the spring system. From 7-3 (B), it is clear that the combs separate from each other, which confirms that the development was complete. Figure 7-4 shows the pictures after etching the sacrificial layer and

seed layer, where the silicon was exposed under the microstructures. At this stage, if a very small force was applied to push the suspended comb drive part and spring structure, the combs and springs would leave the original place. If the force was removed, the structure would come back to the original position. This could be used as a simple test to prove that the comb drive part and spring are indeed suspended and able to deform elastically. Figure 7-5 illustrates the results after the SU-8 microstructure was surface UV modified and selectively electroless plated with Cu. Figure 7-5 (A) (B) show the combs and spring on the top view, and (C) shows the side walls of the combs. From the Figure 7-5, it is evident that that the top surfaces and the side walls of SU-8 comb drive microstructures were coated by shinning material, bearing the appearance of electroplated copper. Using resistance-meter, the resistance of the top surfaces and side walls was measured within the range of 0.8-3.2 Ω, which means the electrical signal can be conducted through this area. Hence the shinning material must be the metal-copper.

7.4 Micro-actuator Response to Electrical Signal

Since the comb drive microstructures has been proven conductive, electrical signals are necessary to verify the performance of the comb drive. The first step is to observe and measure the displacements of the combs when the external voltage is applied. The detailed procedure is described as follows. First, a conductive epoxy with high strength was selected. The wires and bonding pad were connected with the epoxy tightly. Special attention was paid to avoid disturbance while attaching the wires. The external DC voltage was first applied with a small current, which was then increased gradually. At the same time, using high magnification

microscope with record function, the displacement was observed continuously while the device was connected into the power. Both the basic folded cantilever beam spring structure and the folded beam spring structure were tested. Due to the limitation of the instruments and the size of the micro-actuator, the quantitative displacement measurement was difficult to achieve. The realized displacements were estimated from the pictures by comparing to the known lengths of the comb drive fingers. It should be cautioned that such estimation was not very accurate.

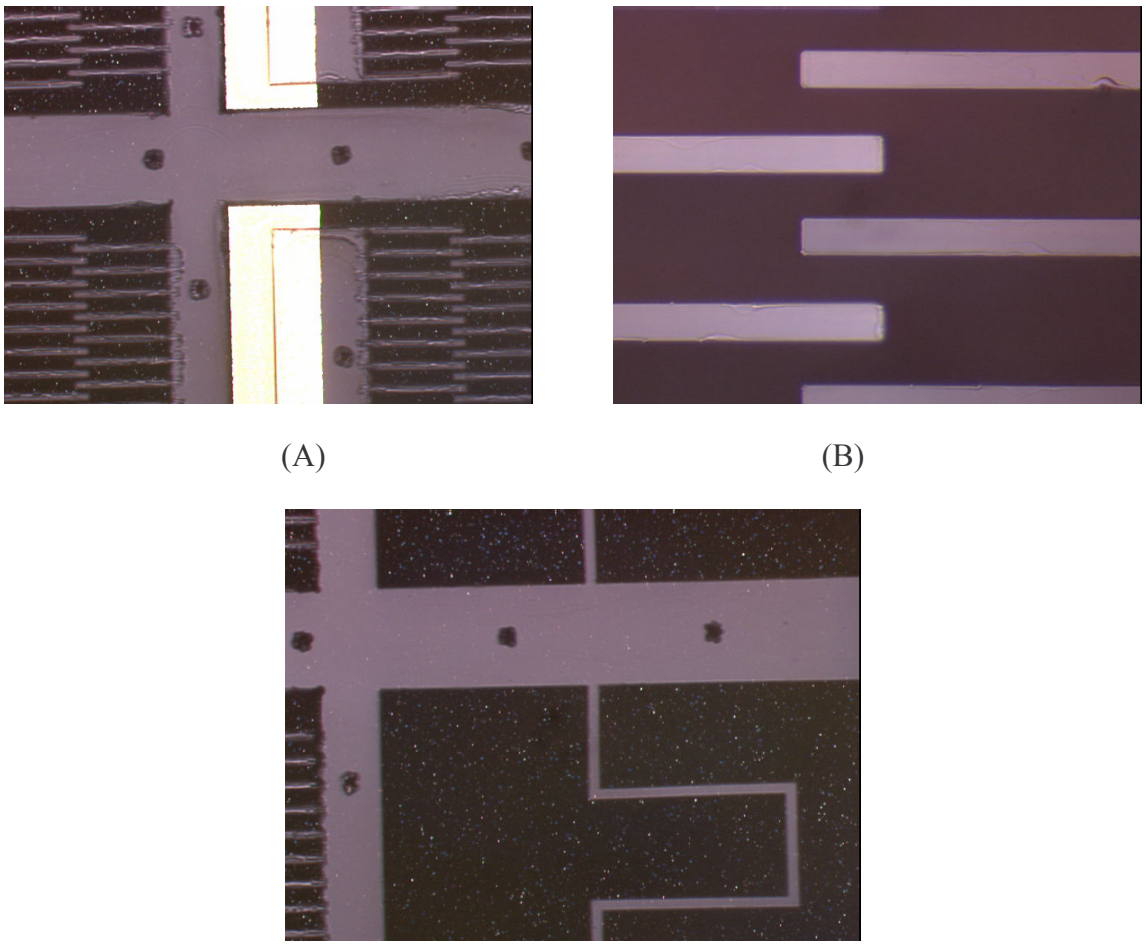

(A) (B)

(C)

Figure 7-3 Optical pictures of comb drive microstructure before etching Cu

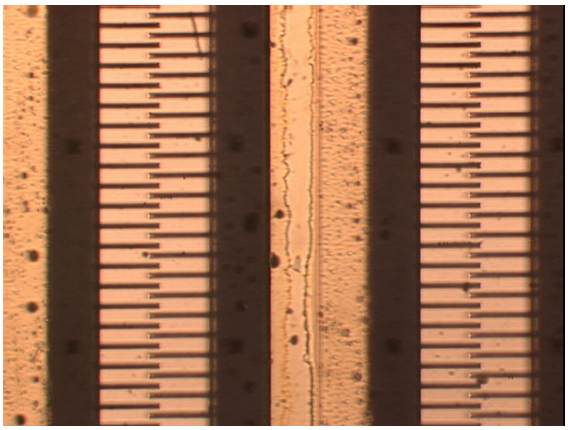

(A)

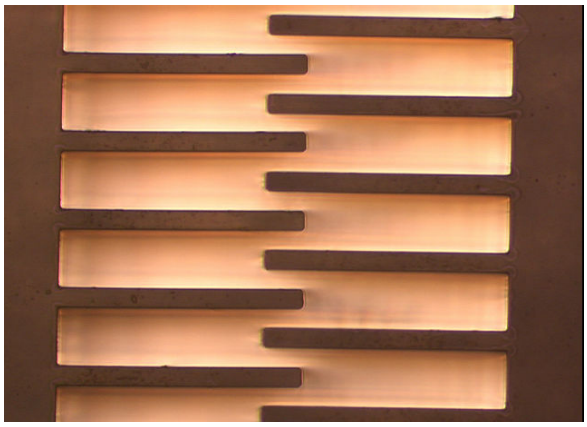

(B)

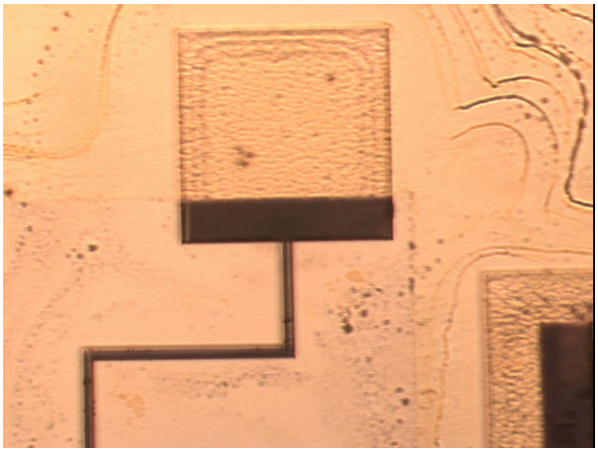

(C)

Figure 7-4 Optical pictures of comb drive microstructure after etching Cu and Au

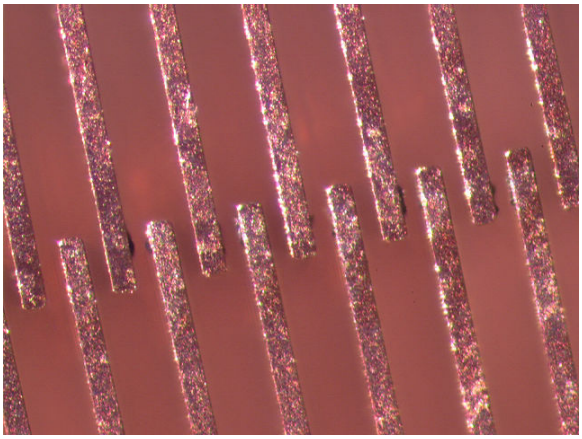

(A)

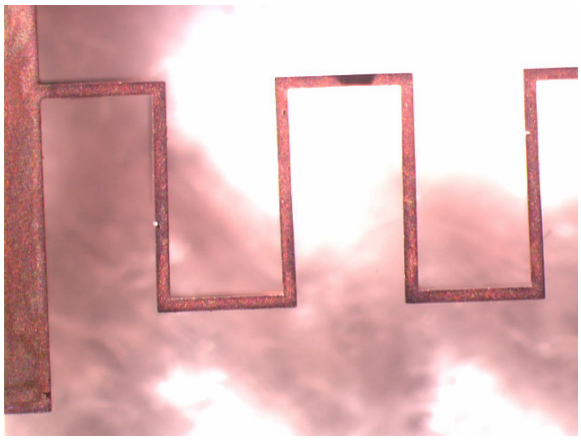

(B)

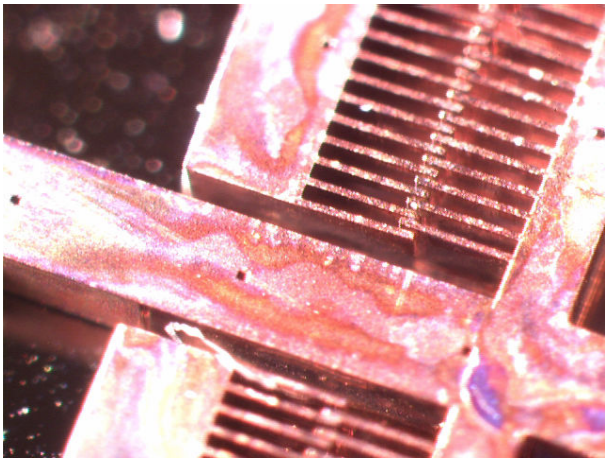

(C)

Figure 7-5 Optical pictures of comb drive microstructures after electroless plating Cu

In the case of folded beam spring structure specimen, the design corresponds to the second row in Table 4-2 and 4-3, and stated in section 4.3.2 as the example in describing the calculation method. Figure 7-6 (A)-(D) show the comb-drive before, after 50V, 100V, and 200V was applied, respectively. The zoom-in pictures of Figure 7-6 are shown in Figure 7-8 (A) and (B) with geometry labeled, for the 100V can 200V cases respectively. When the voltage is at 100 V, the analytically estimated displacement is 3.7 μm. Such small displacement is very difficult to be captured by the estimation of picture. As shown in Figure 7-8 (A), although the picture does suggest a very small displacement in the order of a couple of microns, such estimation is by no means accurate or even indicates a definite movement of the comb drive at all. When the voltage was increased to 200 V, significant displacement was observed, and captured in pictures, as shown in Figure 7-6 (D) and Figure 7-8 (B). Based on the pictures, the displacement estimation is 12 μm. The measured displacement is in good agreement with the calculated values of 14.6 μm in Chapter 4, qualitatively. One can also recall from Chapter 4 that the displacement is proportional to the square of the applied voltage. Hence, the 200 V in principle generates 4 times the displacement of 100 V.

Figure 7-7 (A)-(D) show the pictures of comb drive with basic folded-cantilever beam spring design before, after 50 V, 70 V, and 100 V voltages were applied, respectively. The design corresponds to the last row in Table 4-1, and also as the calculation example in section 4.3.1. The zoom-in pictures with geometry labeled are shown in Figure 7-9. At 50 V, the displacement is estimated at 4 μm. Although the Figure 7-9 (A) does suggest the movement of

comb drive under 50 V, the displacement is still too small for a conclusive measurement, as in the previous case. Qualitatively, the value agrees with the analytical estimation of 9.5 μm. Due to its softer spring structure, at 100 V, 21 μm of displacement can be estimated from Figure 7-9 (B). Although qualitatively, it matches the analysis prediction of 38 μm, the analysis over-predicted the response. Because of the relatively soft spring structure design in the folded cantilever beam structure, when the voltage larger than 100 V was applied to micro-actuator, the displacement increased very rapidly and exceeded the limit of the comb drive (displacement increases with second order of voltage) so that the fingers of the comb-drive would touch each other, resulting in short circuit and burning the comb-drive.

Quantitatively, the observed displacements for both cases were lower than what was calculated by analysis. The causes might be the inaccuracy in displacement measurements, geometry realization, and/or the effect of non-linearity of spring structure starts to surface at relatively large displacement. Further efforts in the future are necessary to correlated quantitatively the analysis prediction and experimental observation.

The response of the micro-actuators clearly indicated that the fabrication methods developed in this work are well capable of realizing the micro-actuators based on SU-8 polymer as the structural materials, and hence achieved the objective of this research work.

7.5 Future Work

While the experimental testing completed in this work clearly demonstrated the validity of the developed fabrication techniques for fabricating polymer based micro-actuator. Due to the

limitation of the time and resources, certain aspects, particularly the quantitative response measurement remained desirable for future improvements.

Structural design improvement. In order to enhance the displacement of the micro-actuator under applied voltage, other spring suspension forms such as tilted folded beam suspension structure should also be evaluated. Side instability and stable travel range can be analyzed both by analytical solution and by finite element simulation, and verified by experimental measurements.

Improve the optical measurements. Due to the limitation of equipments, accurate displacement measurement was not possible at present. Before applying the design to actual micro-actuator applications, the quantitative response clearly should be measured. More extensive effort should be devoted to the selection of the optimal conductive epoxy that can achieve the best bonding between the wire and the micro-structure. Also, operation platform should be designed to reduce disturbance during the wire connection. High magnification microscope with continuous video recording and internal gauge system should be used to quantify the displacement under voltage.

Precise displacement response measurement by capacitance. The relationship between displacement and voltage can also be characterized more precisely by measuring the relationship between the capacitance changes and the applied voltage.

Dynamic displacement response measurement. Instead by a DC voltage, the micro-actuator could also be driven by a sinusoidal wave voltage signal. The micro-actuator

will vibrate continuously, instead of attenuating rapidly as under DC voltage. This would allow the characterization of dynamic responses, such as natural frequencies, of the structure.

7.6 Potential Applications

The material properties characterization methods and the micro-actuator fabrication techniques developed in this research were demonstrated in the design and fabrication of the comb-drive micro-actuator based on SU-8 polymer as the structural material. However, it is clear that the purpose of this research is rather to provide the enabling technology, knowledgebase, general framework and guidelines for developing polymer based micro-transducers. The techniques developed can be directly applied or easily adapted for use in many other applications. Some of the potentials are:

1. Benefit from the research work about measuring properties of metal microstructures, integrating SU-8 with metal microstructures to create metal-polymer mixed microdevices becomes possible.
2. The research work on selectively electroless plating technique shows that after the Au films were formed on SU-8 polymer as a plating base, other conventional electroless plating baths may also be used to obtain thin films of other metals such as Ag, Ni, Cr, and so on. Multi-layer deposition can be also achieved in the same way.
3. Based on the similar design and fabrication process of the micro-actuator, many other types MEMS devices such as micro-sensors, micro-switches, micro-circuits, micro-electrode in microfluidic devices, heaters in micro-PCR chips, and etc. can also be realized.

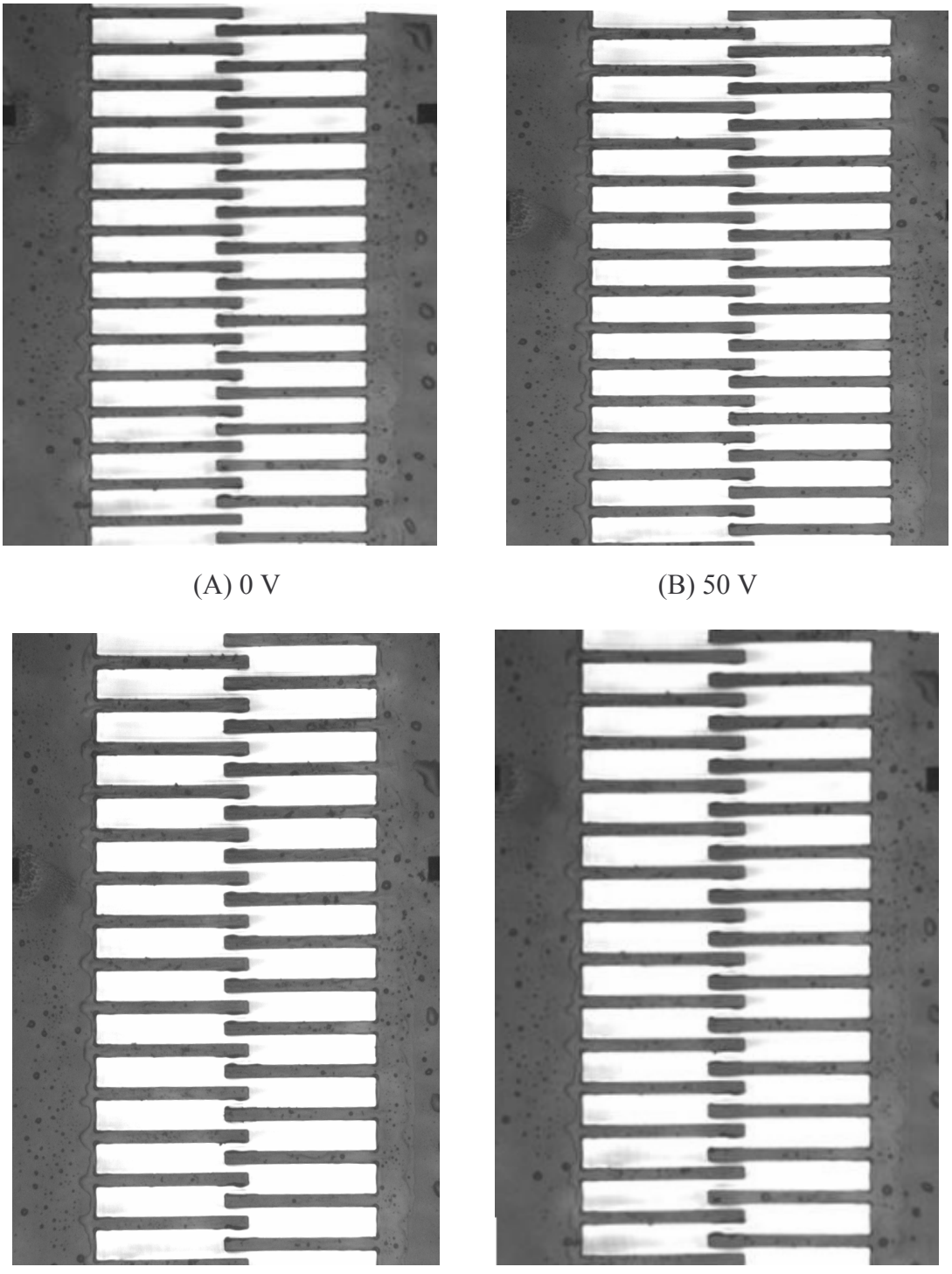

(A) 0 V (B) 50 V

(C) 100 V (D) 200 V

Figure 7-6 The folded beam spring comb drive before and after the voltage was applied

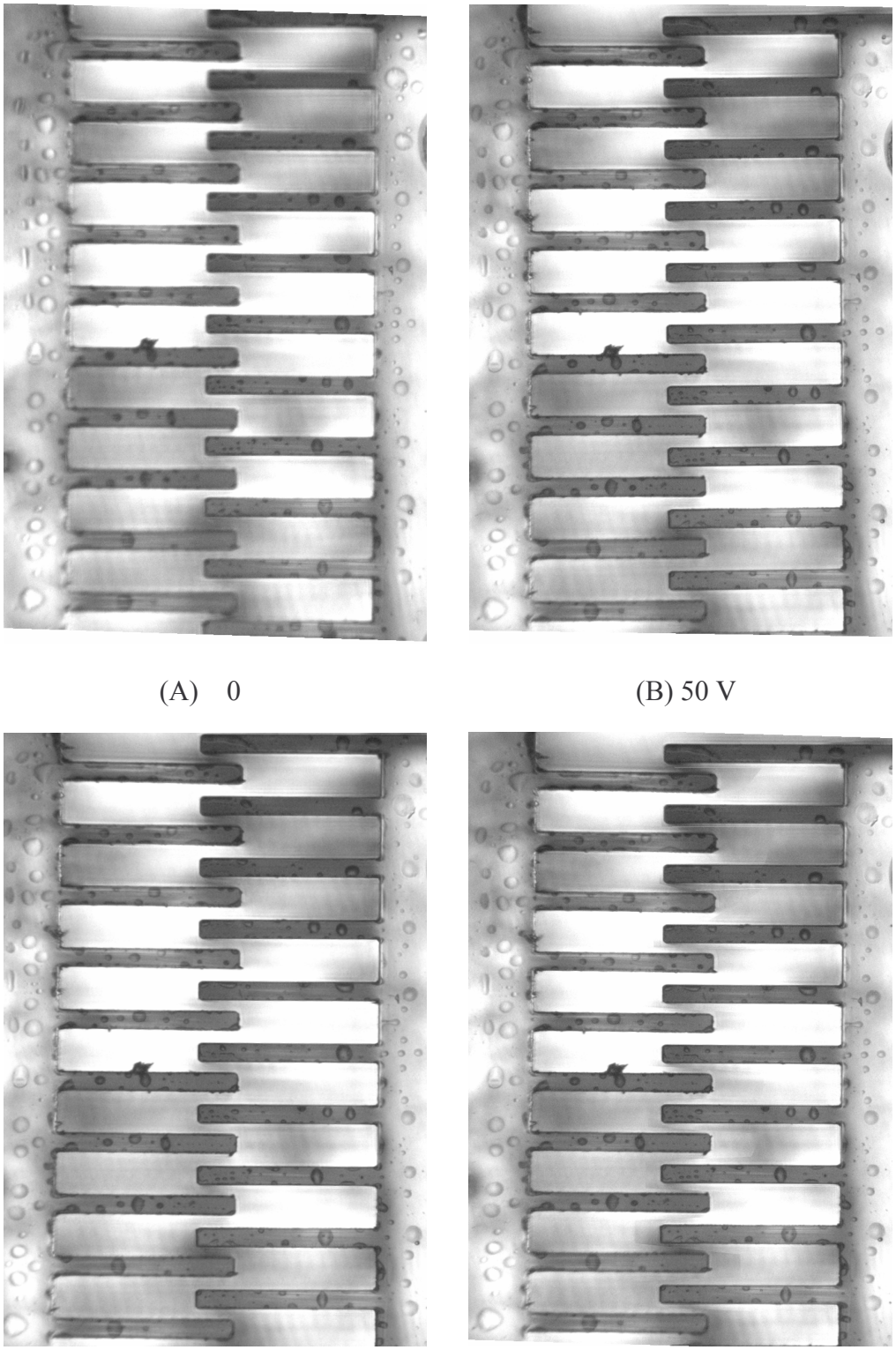

(A) 0 (B) 50 V

(C) 70 V (D) 100 V

Figure 7-7 The folded cantilever beam comb drive before and after the voltage was applied

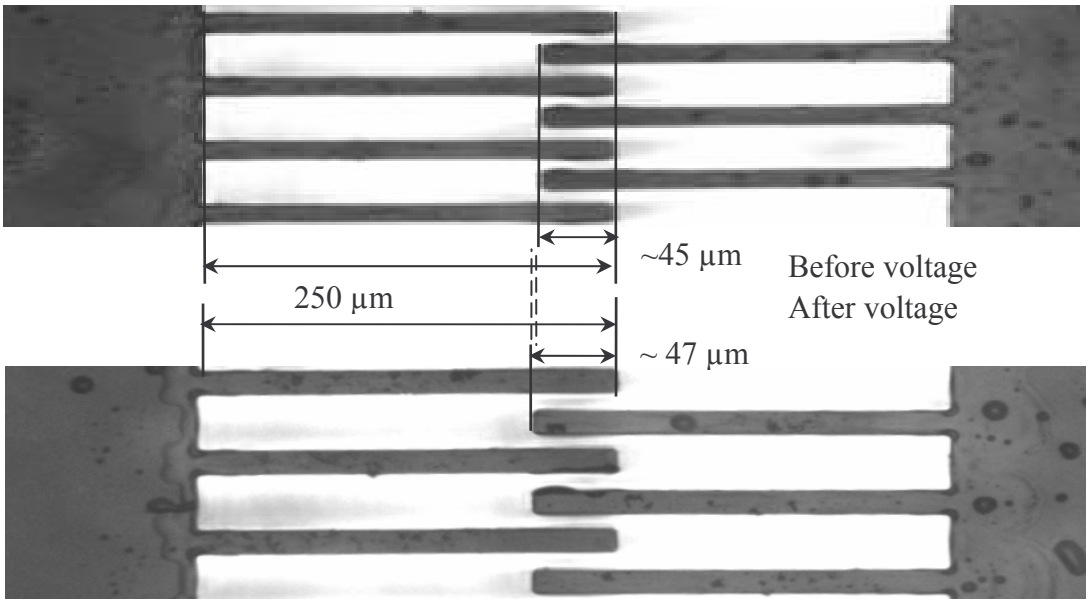

(A) Folded beam flexure (100V)

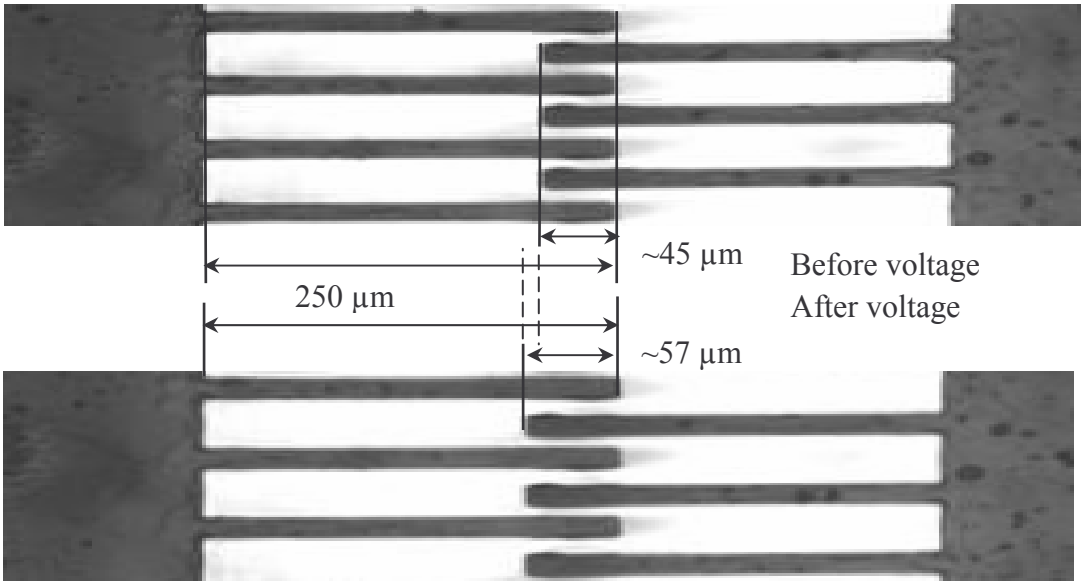

(B) Folded beam flexure (200V)

Figure 7-8 Displacement of the folded beam comb-drive actuators under external voltages

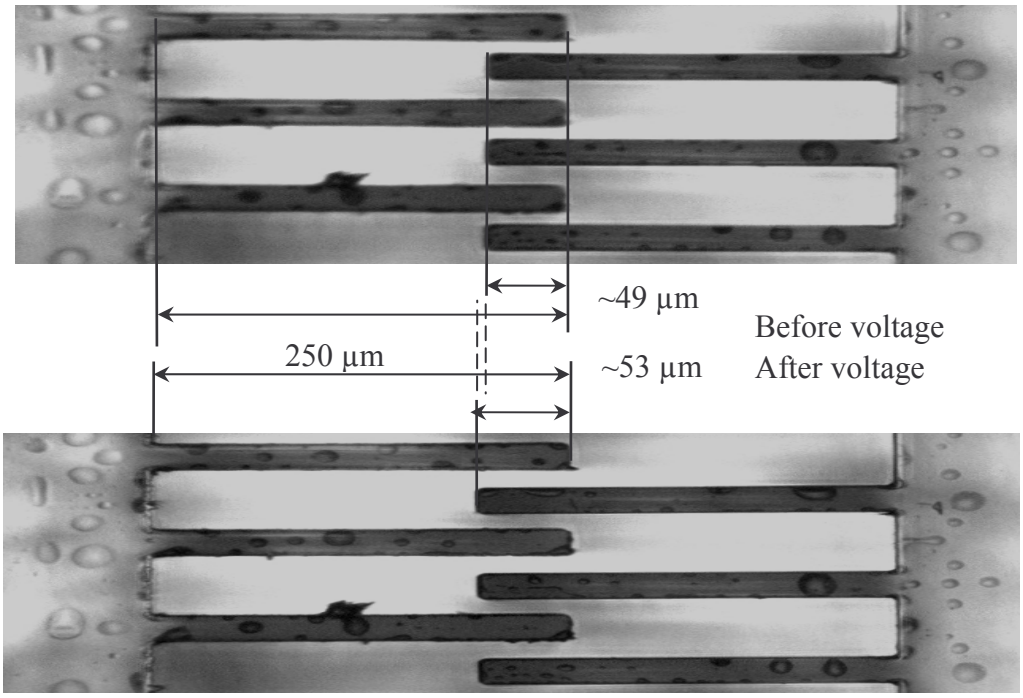

(A) 50 V

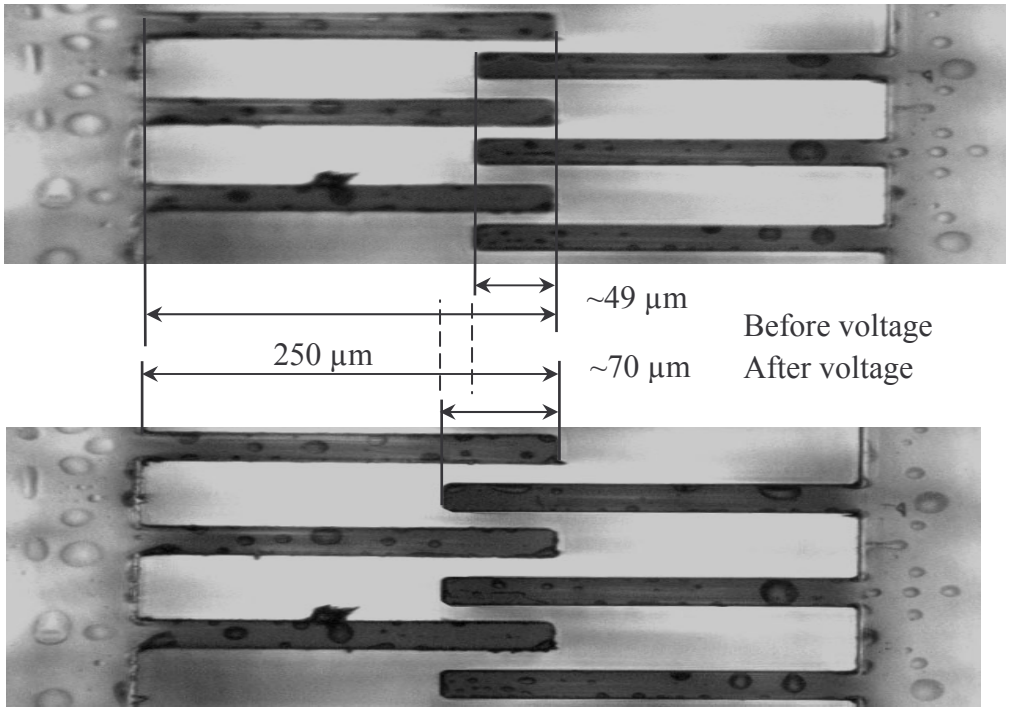

(B) 100 V

Figure 7-9 Displacement of the folded cantilever beam comb-drive actuators under external voltages

CHAPTER 8. SUMMARY

A novel comb drive micro-actuator was designed, analyzed, and successfully fabricated with UV-lithography technology and selectively metallization method. The actuator uses SU-8 polymer material and coated gold film for electric conduction.

The fabrication process began with a gold-deposited silicon wafer surface serving as the seed layer for electroplating copper. The first difficulty encountered was the adhesion problem between the SU-8 material and the metallic surface. In this thesis, we investigated the adhesion properties through standard experiments. The results revealed the relationship between adhesion strengths and metals used, which was then explained from atomic theory perspective for the first time. Among all the tested metals, it was found two groups of adhesion strength. The Ti, Cr, and Au showed stronger adhesion ability with SU-8 polymer than Ni and Cu. Among the group of strong adhesion materials, Au was chosen as a satisfactory base for electroplating not only because of its good adhesion, but also its availability.

The polymer based microdevices investigated in this dissertation have the potential applications of being integrated with metal microstructures to create metal-polymer mixed microdevices. Therefore, the mechanical properties of the metal microstructures are also of interest, which may differ significantly from bulk materials properties due to the difference in material microstructures. Fracture toughness is one of often used properties in mechanical structure design. However, there is no established test procedure for obtaining the fracture toughness for structures at micro-scale. In this thesis, a customized experimental procedure was

designed to measure the fracture toughness of Ni microstructures, which can be easily adapted for other materials measurements.

With the basic material properties established, the mechanisms, principles, and design of the micro-actuator were introduced in detail. Four different spring designs were presented where the basic three folded cantilever beams design and folded-beam flexure design were emphasized. Related analytical results including spring constant calculation and maximum displacement were also given. The micro-actuators were designed to operate with a control voltage of about 100-200 volts corresponding to different structure sizes.

The micro-actuator design was realized with a multi-layer, multi-step micro-fabrication process. Prototypes of comb drive microstructure were fabricated. Two different approaches for fabricating SU-8 based microstructures were used and compared: (1) multilayer processing using modified SU-8 with reduced PAG (photoacidgenerator); (2) multilayer processing using normal SU-8 with copper as sacrificial layer. The second approach was chosen since the first approach resulted in diffusion from sensitive layer to insensitive layer due to the thick upper sensitive layer utilized in our design. For the process of metallizing SU-8 microstructure, there were also two methods -- tilted E-beam evaporation and selectively electroless plating. While using the first method, it should be noticed that the unique support hinges with over-hang edges are necessary, so that the evaporation process with certain tilted angle was required to coat metal film on these electrodes and connectors without causing interconnections and short circuits. The second method can overcome this difficulty. Selectively electroless plating

method offers the possibility of plating the specific SU-8 microstructure but not the silicon wafer, without the requirement of over-hang geometry design. At the same time, it could be seen that the electroless plating of Au colloidal films on modified SU-8 polymer structures served as an intermediate step that allowed the electroless plating of copper on the Au base. The same principle and approach can be easily utilized to obtain thin films of other metals such as Ag, Ni, Cr, and etc., with the Au films formed on the SU-8 surface as the plating base. Furthermore, multi-layer deposition is also possible, which opens up new application possibility. The thickness and uniformity of electroplated metal film are dependent on the plating bath conditions in addition to the optimal UV modification of the cured SU-8 polymer. Tilted UV exposure was proven able to metallize the sidewalls of SU-8 microstructures. The appropriate tilt angle should be chosen according to the ratio between the depth and the gap of microstructures. The combined utilization of tilted and masked exposures could make possible the electroless plating of metal films on any specific surfaces of cured SU-8 microstructures. Such features are essential for the MEMS device structures that require electrical isolation between conductive areas or components.

The optimized procedure was followed to successfully produce the prototype micro-actuators. Tests were conducted on the micro-actuators to prove the validity of the fabrication techniques and design concepts. The resulted micro-actuator clearly demonstrated the displacement response under the applied electrical voltage, although further study is desirable to more accurately characterize the dynamic responses of the prototype system.

REFERENCES

1. Bryzek J., Roundy S., et al., “Marvelous MEMS”, IEEE Circuits & Devices Magazine, Vol. 22, pp. 8-28, 2006

2. Grayson A.C.R., Shawgo, S.R., et al., “A bioMEMS review: MEMS technology for physiologically integrated devices”, in Proceedings of The IEEE, Vol. 92, No. 1, 2004

3. Madou M.J., Fundamentals of Microfabrication: The Science of Miniaturization, 2nd Edition, CRC Press, Boca Raton, FL, 2002

4. Ristic L. and Shah M., “Trends in MEMS technology”, in Proceedings of WESCON, pp. 64-72, Anaheim, CA, USA, Oct. 1996

5. Williams J.D. and Wang W., “Microfabrication of an electromagnetic power relay using SU-8 based UV-LIGA technology”, Microsystem Technologies, Vol. 10, No. 10, pp. 699-705, 2004

6. Dai W., Oropeza, C., Lian K., and Wang W., “Experiment design and UV-LIGA microfabrication technology to study the fracture toughness of Ni microstructures”, Microsystem Technologies, Vol. 12, No. 4, pp. 306-314, 2006

7. Lee D.E., Chen, H.P., Soper S., and Wang W.**, “**An electrochemical micropump and its application in a DNA mixing and analysis system**”,** in Proceedings of Micromachining and Microfabrication, Photonics West, San Jose, CA, pp. 264-271, 2003

8. Yang R., Jeong S.J., and Wang W., "UV-LIGA microfabrication of a power relay based on electrostatic actuation", in Proceedings of Micromachining and Microfabrication, Photonics West, San Jose, California, pp. 122-130, January, 2003

9. Ling Z.G., Lian K., and Jian Z., “Improved patterning quality of SU-8 microstructures by optimizing the exposure parameters”, in Proceedings of SPIE, Vol. 3999, pp. 1019-127, 2000

10. Konaka Y. and Allen, M.G., “Single and multi-layer electroplated microaccelerometers”, in Proceedings of the IEEE Micro Electro Mechanical Systems (MEMS), pp. 168-173, 1996

11. Lorenz H., Despont M., et el., "High aspect ratio ultra thick, negative-tone near-UV photoresist and its applications for MEMS", Sensors and Actuators. A, Vol. A64, pp. 33-39, 1998

12. Jacobsen S.C., “A design overview of an eccentric-motion electrostatic microactuators”, Sensors and Actuators, Vol. 20, pp. 1-16, 1989

13. Sun Y., Piyabongkarn, D., et al., “A high-aspect-ratio two-axis electrostatic microactuator with extended travel range”, Sensors and Actuators A, Vol. 102, No. 1, pp. 49-60, 2002

14. Ye W., “Optimal shape design of an electrostatic comb drive microelectromechanical systems”, Journal of Microelectromechanical Systems, Vol. 7, No. 1, pp. 16-26, 1998

15. Zhou G. and Dowd P., “Tilted folded-beam suspension for extending the stable travel range of comb-drive actuators”, Journal of Micromechanics and Microengineering., Vol. 13, pp. 178-183, 2003

16. Tang W.C., Nguyen T.H., and Howe R.T., “Laterally driven polysilicon resonant microstructures”, in Proceedings of Tech. Dig. IEEE Micro Electro Mech. Syst. Workshop (Salt Lake City, 20–22 Feb. 1989), pp. 53–59, 1989

17. Johnson W.A. and Warn L.K., “Electrophysics of micromechanical comb actuators”, Journal of Microelectromechanical Systems, Vol. 4**,** pp. 49–59, 1995

18. Ye W. and Mukherjee S., “Optimal shape design of three-dimensional MEMS with applications to electrostatic comb drives”, International Journal for Numerical Methods in Engineering, Vol. 45, pp. 175–94, 1999

19. Sniegowsi J.J. and Garcia E.J., “Surface micromachined gear trains driven by an on-chip electrostatic micro-engine”, IEEE Electron Device Letters, Vol. 17, No. 7, pp. 366–368, 1996

20. Steven R.M. and Kota S., “A new class of high force, low-voltage, compliant actuation systems”, in Proceedings of Solid-State Sensor and Actuator Workshop, Hilton Head Island, SC (US), Apr, 2000

21. Andrew Y.J.L., Hui C.Y., and Tien N.C., “Electrostatic model for an asymmetric comb drive”, Journal of Microelectromechanical Systems, Vol. 9, pp. 16–26, 2000

22. Chan E.K. and Dutton R.W., “Electro-static micromechanical actuator with extended range of travel”, Journal of Microelectromechanical Systems, Vol. 9, pp. 321–328, 2000

23. Hirano T., Furuhata T., Gabriel K.J., and Fujita H., “Design, fabrication, and operation of submicron gap comb-drive microactuators”, Journal of Microelectromechanical Systems, Vol. 1, pp. 52–59, 1992

24. Patterson P.R., et al, “A scanning micromirror with angular comb drive actuation”, in Proceedings of 15th IEEE International Conference of MicroElectroMechanical Systems, pp. 544–547, 2002

25. Zhao Y. and Cui T., “Fabrication of high-aspect-ratio polymer-based electrostatic comb drives using the hot embossing technique”, Journal of Micromechanics and Microengineering, Vol. 13, pp. 430-435, 2003

26. Eberhardt W., et al., “Innovative concept for the fabrication of micromechanical sensor and actuator devices using selectively metallized polymers”, Sensors and Actuators A, Vol. 97-98, pp. 473-477, 2002

27. LaBianca N. and Delorme J., "High aspect ratio resist for thick film applications", in Proceedings of SPIE, Vol. 2438, pp. 846-852,1995

28. Lorenz H., Despont M., Vettiger P., and Renaud P., "Fabrication of photoplastic high-aspect Ratio microparts and micromolds using SU-8 UV resist", Microsystem Technologies, Vol. 4, pp. 143-146, 1998

29. Lee K., LaBianca N., Rishton S., and Zohlgharnain S., "Micromachining applications for a high resolution ultra-thick photoresist", Journal of Vacuum Science and Technology, Vol. B13**,** pp. 3012-3016, 1995

30. Lorenz H., Despont M., et al., "EPON SU-8: A Low-cost negative resist for MEMS", Journal of Micromechanics and Microengineering, Vol. **7,** pp. 121-124, 1997

31. Williams J.D. and Wang W., “UV lithography process for ultra high aspect ratio SU-8 microstructures with and without megasonic development,” to appear in Microsystem Technologies, 2006

32. Jeong S.J. and Wang W., “Microaccelerometers using cured SU-8 as structural material”, in Proceedings of SPIE Symposium on Micromachining and Microfabrication, Photonics West, Mems/Moems Components And Their Applications, Proceedings of SPIE Vol. 5344, January 24-29, San Jose, California, 2004

33. Curtis P., Iezekiel S., Miles R.E., and Pescod C.R., “SU-8 as a material for integrated all-optical microwave filters”, Microwave Engineering, Vol. 39, pp. 51-54, 2001

34. Thorpe J., Steenson D., and Miles R., "High frequency transmission line using micromachined polymer dielectric", Electron. Letters, Vol. 34 , pp. 1237-1238, 1998

35. Liu J., Cai B., Zhu J., et al, “Fabrications of high-aspect ratio microstructure on metallic substrate using SU-8 resist”, in Proceedings of SPIE Micromaching and Microfabrication Process Technology and Devices, Vol. 4601, pp. 200-204, 2001

36. Zhu J., Zhao X., and Ni Z., “High aspect ratio microstructure fabrication using SU-8 resist”, in Proceedings of SPIE Micromaching and Microfabrication Process Technology and Devices, Vol. 4174, pp. 86-89, 2000

37. Conradie E.H. and Moore D.F., “SU-8 thick photoresist processing as a functional material for MEMS applications”, Journal of Micromechnics and Microengineering, Vol. 12, pp. 368-374, 2002

38. Khoo H.S., Liu K.K., and Tseng F.G., “Mechanical strength and interfacial failure analysis of cantilevered SU-8 microposts”, Journal of Micromechnics and Microengineering, Vol. 13, pp. 822-831, 2003

39. Williams J.D. and Wang W., “Study on the postbaking process and the effects on ultraviolet lithography of high aspect ratio SU-8 microstructures,” Journal of Microlithography, Microfabrication and Microsystems, Vol. 3, No. 4, pp. 563-568, October 2004

40. Bhushan B., “Adhesion and stiction: Mechanisms, measurement techniques, and methods for reduction”, Journal of Vacuum Science and Technology B, Vol. 21, No. 6, pp. 2262-2296, 2003

41. ASTM, “ASTM C633: Standard test method for adhesion or cohesive strength of flame-sprayed coatings,” American Society for Testing and Materials, Philadelphia, PA, pp. 993, 1982

42. Derjaguin B.V., Krotova N.A., and Smilga V.P., “Adhesion of solids (translated from Russian by R. K. Johnston) (consultants Bureau, New York, 1978), 1978

43. Buch A., Pure Metals Properties- a Scientific Technical Handbook, ASM International and Freund Publishing House, LTD, ISBN 0-87170-637-7, 1999

44. Miessler G.L., Tarr D.A., Inorganic Chemistry, Prentice Hall, Engewood cliffs, New Jersey, 1991

45. Sharpe A.G., Inorganic Chemistry, Longman Publishing Group, 1992

46. Dai W., Lian K., and Wang W., “A quantitative study on the adhesion property of cured SU-8 on various metallic surfaces”, Microsystem Technologies, Vol. 11, pp. 526 -534, 2005

47. Wilson C.J., and Beek P.A., “Fracture testing of bulk silicon microcantilever beams subjected to a slide load”, Journals of MEMS, Vol. 3, pp. 142-150, 1996

48. Mazza E., Dual J., and Schiltges G., “Mechanical properties of microstructures: Experiments and theory”, in The International Society for Optical Engineering, Microlithography and Metrology in Micromachining III Proc., pp. 12-22, September, 1997

49. Sharpe W.N., Yuan B., and Edwards R.L., “A new technique for measuring the mechanical properties of thin films”, Journal of Microelectromechanical Systems, Vol. 6, No. 3, pp. 193-198, 1997

50. Sharpe W.N., Brown S., Johnson G.C., and Knauss W., “Round-Robin tests of modulus and strength of polysilicon”, in Materials Research Society Symposium N: Microelectromechanical Structures for Materials Research Proc., San Francisco, California, pp. 57-65, April 15-16, 1998

51. Tsuchiya T., Tabata O., Sakata J., and Taga Y., “Specimen size effect on tensile strength of surface micromachined polycrystalline silicon thin films”, in IEEE Tenth Annual International Workshop on Micro Electro Mechanical Systems Proc., Nagoya, Japan, pp. 529-534, January 26-30, 1997.

52. Ballarini R., Mullen R.L., and Yin Y., “The fracture toughness of polysilicon microdevices”, in Materials Research Society Symposium N: Microelectromechanical Structures for Materials Research Proc., San Francisco, California, pp. 137-142, April 15-16, 1998

53. Greek S., and Ericson F., “Young's modulus, yield strength and fracture ftrength of microelements determined by tensile testing”, in Materials Research Society Symposium N: Microelectromechanical Structures for Materials Research Proc., San Francisco, California, pp. 51-56, April 15-16, 1998.

54. Johansson S., Schweitz J.A., Tenerz L., and Tiren J., “Fracture testing of silicon microelements in situ in a scanning electron microscope,” Journal of Applied Physics, Vol. 63, No. 10, pp. 4799-4803, 1998

55. Kraft O., Schwaiger R., and Nix W.D., “Measurement of mechanical properties in small dimensions by microbeam deflection,” in Materials Research Society Symposium N:

Microelectromechanical Structures for Materials Research Proc., San Francisco, California, pp. 39-44, April 15-16, 1998

56. Pratt R.I., and Johnson G.C., "Multilayer microelectromechanical structures for material property characterization", in Materials Research Society Symposium N: Microelectromechanical Structures for Materials Research Proc., San Francisco, California, pp. 15-20, April 15-16, 1998

57. Suito W. and Dunn M., "Fracture initiation at sharp notches in single crystal silicon", Journal of Applied Physics., Vol. 83, No. 7, pp. 3574-3582, 1998

58. Van Arsdell W. and Brown S., "Subcritical crack growth in silicon", Journal of Microelectromechanical Systems, Vol. 8, No. 3, pp. 319-327, 1999

59. Fitzgerald A.M., Dauskardt R.H., and Kenny T.W., "Fracture toughness and crack growth phenomena of plasma-etched Single crystal silicon", Sensors and Actuators, Vol. A83, pp. 194-199, 2000

60. Lee S.-H., Kim J.S., et al., "Evaluation of microfracture toughness and microcracking with notch tip radius of Si film structure for microactuator in hard disk drives", Microsystem Technologies, pp. 91-98, 2001

61. Kahn H., Ballarini R., and Heuer A.H., "Dynamic fatigue of silicon", Current Opinion in Solid State and Materials Science, Vol. 8, pp. 71-76, 2004

62. Shi Q., Chang S.-C., Putty M.W., and Hicks D.B. "Characterization of electroformed nickel microstructures", in Proceedings of SPIE, Vol. 2639, pp. 191-199, 1995

63. Mazza E., Abel S., and Dual J., "Experimental determination of mechanical properties of Ni and Ni-Fe microbars", Microsystems Technologies, Vol. 2, pp. 197-202, 1996

64. Ruther P., Bacher W., Feit K., and Maas D., "Prototype of a micro testing system made by the LIGA process to measure the young's modulus in cantilever microbeams", ASME Journal of Dynamic. Systems, Measurement, and Control, Vol. 119, pp. 57-60, 1997

65. Sharpe W.N., LaVan D.A., and McAleavey A., "Mechanical testing of thicker MEMS materials", ASME Journal of MEMS, Vol. 62, pp. 93-97, 1997

66. Sharpe W.N., LaVan D.A., and Edwards R., "Mechanical properties of LIGA-deposited nickel for MEMS transducers", in IEEE International Conference on Solid-State Sensor and Actuators Proc., Chicago, Illinois, pp. 607-610, June 16-19, 1997

67. Sharpe W.N. and McAleavey A., “Tensile properties of LIGA nickel”, in The International Society for Optical Engineering Conference on Materials and Device Characterization in Micromachining Proc., Santa Clara, CA, pp. 130-137, September, 1998

68. Buchheit T.E., Christenson T.R., Schmale D.T., and LaVan D.A., “Understanding and tailoring the mechanical properties of LIGA fabricated materials”, in Materials Research Society Symposium AA: Materials Science of Microelectromechanical Systems (MEMS) Devices Proc., Boston, Massachusetts, pp. 121-126, December 1-2, 1998

69. Christenson T.R., Buchheit T.E., Schmale D.T., and Bourcier R.J., “Mechanical and metallographic characterization of LIGA fabricated nickel and 80% Ni-20% Fe permalloy”, Materials Research Society Symposium N: Microelectromechanical Structures for Materials Research Proc., San Francisco, California, pp. 185-191, April 15-16, 1998

70. Kelly K., Stephens S., Simhadri S., and Meletis E., “Mechanical property evaluation of electroplated high aspect ratio microstructures”, in Materials Research Society Symposium N: Microelectromechanical Structures for Materials Research Proc., San Francisco, California, pp. 173-178, April 15-16, 1998

71. Majjad H., Basrour S., Delobelle P., and Schmidt M., “Dynamic determination of Young's modulus of electroplated nickel Used in LIGA technique”, Sensors and Actuators, Vol. A74, pp. 148-151, 1999

72. American Society for Testing and Materials, “Standard Test Method for Plain-Strain Fracture Toughness of Metallic Materials Design. E399”, Annual Book of ASTM Standards. 03, Philadelphia, pp. 427-534, 1998

73. Jeong S.J., “UV-LIGA micro-fabrication of electrostatically actuated transducers and their applications”, Ph.D. General Proposal, Louisiana State University, Jan., 2004

74. Huang W. and Lu G., “Analysis of lateral instability of in-plane comb drive MEMS actuators based on a two-dimensional model”, Sensors and Actuators A, Vol. 113, pp. 78–85, 2004

75. Chu P.B. and Pister K.S.J., “Analysis of closed-loop control of parallel-plate electrostatic microgrippers”, in Proceedings of the IEEE International Conference Robotics and Automation, San Diego, CA, USA, pp. 820–825, 1994

76. Seeger J.I. and Crary S.B., “Stabilization of electrostatically actuated mechanical devices”, in Proceedings of the Ninth International Conference Solid-State Sensors and Actuators, Chicago, IL, USA, pp. 1133–1136, 1997

77. Legtenberg R., Groeneveld A.W., and Elwenspoek M., "Comb-drive actuators for large displacements", Journal of Micromechnics and Microengineering, Vol. 6, pp. 320–329, 1999

78. Dai W., Wang W., and Lian K., "Design and fabrication of a SU-8 based electrostatic microactuator", to appear in Microsystem Technologies, 2006

79. Ling Z.G., Lian K.. And Jian Z., "Expansion of SU-8 application scope by PAG concentration modification", in Proceedings of SPIE, Vol. 4979, pp. 1019-127, 2003

80. Jiguet S. , Bertsch A. , Hofmann H. , and Renaud P. , "Conductive SU-8 photoresist for microfabrication", Advanced Functional Materials, Vol.15, pp. 1511-1516, 2005

81. Leeuw D., Dagobert M., et al., "Method of producing vertical interconnects between thin film microelectronic devices and products comprising such vertical interconnects", United States Patent 6635406

82. Shafeev G.A., Themlin J.M., et al., *"*Enhanced adherence of area-selective electroless metal plating on insulators*"*, Journal of Vacuum Science and Technology A, Vol.14, pp. 319-326, 1996

83. Hrapovic S., Liu Y., Enright G., Bensebaa F., and Luong J.H.T., "New strategy for preparing thin gold films on modified glass surfaces by electroless deposition*"*, Langmuir, Vol. 19, pp. 3958-3965, 2003

84. Henry A.C. and McCarley R.L., "Selective deposition of metals on plastics used in the construction of microanalytical devices: Photo-directed formation of metal features on PMMA", Journal of Physical Chemistry. B*,* Vol. 105, pp. 8755-8761, 2001

85 . Grabar K.C., Freeman R.G., Hommer M.B., and Natan M., "Preparation and characterization of Au colloid monolayers", Journal of Analytical Chemistry, Vol. 67, pp. 735-743, 1995

86. Musick M.D., Pena D.J., et al., "Electrochemical properties of colloidal Au-based surfaces: Multilayer assemblies and seeded colloid films", Langmuir, Vol. 15, pp. 844-850, 1999

87. Leff D.V., Brandt L., and Heath J.R., "Synthesis and characterization of hydrophobic, organically-soluble gold nanocrystals functionalized with primary amines", Langmuir, Vol. 12, pp. 4723-4730, 1996

88. Xu D., Kang E.T., et al., “Selective electroless plating of copper on (100)-oriented single crystal silicon surface modified by UV-induced coupling of 4-vinylpyridine with the H-terminated silicon”, Journal of Physical Chemistry B, Vol. 106, No. 48, pp. 12508 -12516, 2002

89. Dai W. and Wang W., “Selective metallization of cured SU-8 microstructures using electroless plating method”, to appear in Sensors and actuators, 2006

VITA

Wen Dai is a doctorate candidate in the Program of Engineering Science of Louisiana State University since 2002. She received her bachelor's degree and master's degree from Southeast University of China, both in electrical engineering, in 1998 and 2002 respectively. Ms. Dai worked on optical waveguide research before joining Louisiana State University. Her current research interests focus on the design and fabrication techniques for polymer based MEMS devices, especially the micro-transducers. Ms. Dai has published several papers on the design, material characterization, and fabrication of polymer based MEMS structures. She also had several publications in the area of optical waveguides.